Lattice calculation of the mass difference between the long- and short-lived K mesons for physical quark masses

Bigeng Wang

Submitted in partial fulfillment of the
requirements for the degree of
Doctor of Philosophy
under the Executive Committee
of the Graduate School of Arts and Sciences

COLUMBIA UNIVERSITY

2021

Abstract

Lattice calculation of the mass difference between the long- and short-lived K mesons for physical quark masses

Bigeng Wang

The two neutral kaon states in nature, the K_L (long-lived) and K_S (short-lived) mesons, are the two time-evolution eigenstates of the $K^0 - \overline{K^0}$ mixing system. The prediction of their mass difference Δm_K based on the standard model is an important goal of lattice QCD. Non-perturbative formalism has been developed to calculate Δm_K and the calculation has been extended from the first exploratory calculation with only connected diagrams to full calculations on near-physical[1] and physical ensembles[2].

In this work, we extend the calculation described in Reference [2] from 59 to 152 configurations and present a new analysis method employed to calculate Δm_K with better reduction of statistical error on this larger set of configurations. By using a free-field calculation, we will show that the four-point contractions in our calculation method yields results consistent with the Inami-Lim calculation[3] in the local limit. We also report a series of scaling tests performed on $24^3 \times 64$ and $32^3 \times 64$ lattice ensembles to estimate the size of the finite lattice spacing error in our Δm_K calculation.

We will present the Δm_K calculation on the ensemble of $64^3 \times 128$ gauge configurations with inverse lattice spacing of 2.36 GeV and physical quark masses obtaining results coming from 2.5 times the Monte Carlo statistics used for the result in [2]. With the new analysis method and estimated finite lattice spacing error, we obtain $\Delta m_K = 5.8(0.6)_{\text{stat}}(2.3)_{\text{sys}} \times 10^{-12}$MeV. Here the

first error is statistical and the second is an estimate of largest systematic error due to the finite lattice spacing effects.

The new results also imply the validity of the OZI rule for the case of physical kinematics in contrast to the previous calculation of Δm_K with unphysical kinematics[1], where contributions from diagrams with disconnected parts are almost half the size of the contributions from fully connected diagrams but with the opposite sign.

Table of Contents

Acknowledgments vi

Dedication viii

Chapter 1: Introduction and background 1

1.1 The standard model and flavor physics 1

1.2 Neutral kaon mixing and Δm_K 2

Chapter 2: The physics of Δm_K 4

2.1 The operator product expansion(OPE) and Δm_K 5

2.2 GIM mechanism: short- and long-distance characteristics of Δm_K 7

2.2.1 Calculation of Δm_K from the bag parameter B_K 8

2.2.2 Non-perturbative calculation of Δm_K using a renormalization scale above the charm quark mass 11

2.3 Calculation of the diagrams with two bi-local $\Delta S = 1$ operators on the lattice 12

Chapter 3: Calculation of Δm_K with lattice QCD 14

3.1 Δm_K and integrated correlation functions 14

3.1.1 Three point matrix elements for subtraction of terms with exponential time growth 16

3.1.2 Two-point correlation functions for masses and normalization factors 18

3.2 Operators and Wick contractions 19
3.3 Evaluation of correlation functions on the lattice 24
3.3.1 Chiral symmetry and lattice actions 25
3.3.2 Propagators 27
3.3.3 Sample all-mode averaging(AMA) method 33
3.4 Non-perturbative renormalization 34
3.4.1 Four-quark operators and irreducible representations of $SU(4) \times SU(4)$ . . 35
3.4.2 Non-perturbative renormalization: the RI-SMOM renormalization scheme . 39
3.4.3 Perturbation theory: conversion from RI-SMOM to $\overline{MS}$ scheme 44
3.4.4 Perturbation theory: calculation of the Wilson coefficients in the $\overline{MS}$ scheme. 44

Chapter 4: Data analysis of Δm_K calculation 46
4.1 Fitting of correlation functions 46
4.1.1 Fitting two-point correlation functions 46
4.1.2 Fitting three-point correlation functions 47
4.1.3 Fitting three-point correlation functions with multiple source-sink separations 48
4.1.4 Fitting four-point correlation functions with single-integration method . . . 50
4.2 Data analysis of type-4 diagrams 54
4.2.1 Fitting type-4 diagrams with multiple source-sink separations 57
4.2.2 Removal of random source correlations in type-4 diagrams 58
4.3 Calculating Δm_K from four-point correlation function data 59
4.4 Fitting Δm_K with statistical errors 61
4.4.1 Fitting with the jackknife method 61

4.4.2 Application to Δm_K data analysis . . . 63

4.4.3 Sample all-mode averaging(AMA) corrections and the super-jackknife method 64

Chapter 5: Systematic errors and normalization factors . . . 66

5.1 Finite volume effects . . . 66

5.2 The around-the-world effects . . . 69

5.3 Free-field verification of the four-point contractions in the local limit . . . 71

5.3.1 Calculation with four-point correlation functions . . . 73

5.3.2 Connection between the four-point and three-point diagrams . . . 73

5.3.3 Calculation with three-point correlation functions . . . 75

5.3.4 Comparison between BG/Q supercomupter and analytic calculation . . . 76

5.3.5 Results . . . 78

5.4 Consistency of NPR factors used for Δm_K with other published NPR values . . . 81

5.5 Finite lattice spacing effects . . . 82

5.5.1 Elimination of $O(a)$ finite lattice spacing errors . . . 82

5.5.2 Sources of $O(a^2)$ finite lattice spacing errors . . . 83

5.6 Scaling test on lattices with different lattice spacings . . . 83

5.6.1 Results from two-point functions . . . 84

5.6.2 Scaling of three-point matrix elements . . . 85

5.6.3 Scaling of four-point single-integrated correlation functions . . . 89

Chapter 6: Δm_K calculation with physical quark masses . . . 96

6.1 Details of calculation . . . 96

6.2 Results . . . 97

6.2.1 Two-point results . . . 97
6.2.2 Three-point light-state matrix elements: overview . . . 99
6.2.3 Three-point light-state matrix elements: K to π matrix elements . . . 99
6.2.4 Three-point subtraction coefficients: $c_{\mathrm{s}i}$ and $c_{\mathrm{p}i}$ . . . 103
6.2.5 Three-point light-state matrix elements: K to $\pi\pi$ matrix elements . . . 105
6.3 Contributions to Δm_K . . . 107
6.3.1 AMA correction . . . 111
6.4 Systematic errors . . . 111
6.5 Conclusion . . . 112

Chapter 7: Conclusion and outlook . . . 113

References . . . 116

Appendix A: Normalization conventions and dimensions of the matrix elements . . . 117
A.1 Normalization convention of meson states . . . 117
A.2 Dimension of three-point matrix elements . . . 118
A.2.1 Dimension of three-point matrix elements with four-quark operators . . . 118
A.2.2 Dimension of three-point matrix elements with two-quark operators . . . 120
A.3 Dimension of four-point correlation functions . . . 121

Appendix B: Input parameters used in Δm_K calculation . . . 122

Appendix C: Diagrams . . . 123
C.1 Four-point diagrams . . . 123

C.2 Three-point diagrams . . . 128
C.3 Three-point diagrams: kaon to two-pion diagrams . . . 132
C.4 Two-point diagrams . . . 135

Appendix D: Contractions . . . 137
D.1 Two-point contractions . . . 137
D.2 Three-point contractions . . . 138
D.3 Four-point contractions . . . 140

Appendix E: Analytic free-field calculation with free domain wall fermion propagators . . 142
E.1 Analytic free DWF propagators in coordinate space . . . 142
E.1.1 Wall source propagators . . . 144
E.1.2 Point-source-point-sink propagators . . . 145
E.2 Contractions . . . 146
E.2.1 Two-point contractions . . . 146
E.2.2 Three-point contractions . . . 147
E.2.3 Four-point contractions . . . 149
E.3 Time dependence of the free-field correlation functions with around-the-world effects 150
E.3.1 Pseudo-scalar meson: two-point correlation functions . . . 151
E.3.2 Pseudo-scalar meson: three-point correlation functions . . . 152

Acknowledgements

First of all, I would like to give my utmost praises and thanks to my Lord, my Savior and my Shepherd, Jesus Christ, who restores my soul and leads me in paths of righteousness for his name's sake.

I want to express my deepest gratitude to my advisor Professor Norman H. Christ for his guidance, advice, encouragements, and help during my research at Columbia University. I could not have gone so far without his constant support and encouragements. I'm deeply impressed and encouraged by his passion for physics and his great support for his students. I'm grateful to Professor Robert Mawhinney for all the insightful discussions during the group meetings and kindly providing carpool for the traveling to BNL for our collaboration meetings.

I would like to thank Professor Chris Sachrajda, Dr. Armajit Soni, Dr. Taku Izubuchi, Professor Xu Feng, Professor Luchang Jin, Dr. Chris Kelly, Dr. Masaaki Tomii, and Dr. Joseph Karpie for very illuminating discussions and generous help on all kinds of problems.

I would like to thank Dr. Chulwoo Jung for his help on the compilation, the machines and all kinds of tests on BG/Q and Summit supercomputers. I greatly appreciate Ziyuan Bai's help on getting me more familiar with the calculation.

I would like to thank my dear roommate, friend and colleague Tianle Wang. We have spent most of our PhD life together and survived the stressful lockdown time during the COVID-19 pandemic. I am also indebted to my fellow graduate students, including Jiqun Tu, Duo Guo, Yidi Zhao and Tuan Nguyen.

I would like to thank Professor Wei-Yann Tsai and his family, Professor Ada Mui and her family and Professor Huiming Yin and his family for their Agape in Christ towards me since the beginning of my life here in NYC. I am fortunate to have many brothers and sisters from the Columbia Chinese Bible Study Group, especially our group advisors: Duncan Szeto, Jonathan&Olive Chiu, Vida Huimin Herling and Hon Eng, whose intercession and support has always brightened up my life.

Lastly, and most importantly, I would like to thank my parents, for many years of love and

support as I study physics abroad and far away from them. I wish I had spent more time with them in the past years. I feel very blessed and loved by my Lord to have my girlfriend Xin Chen with me during all these challenging times. The meals she cooked with love, the time when she listened with great patience to my lengthy sharing and the wonderful moments when we worshiped together have always made me feel deeply loved.

Dedication

To the Logos, my Lord, my Savior and my Shepherd, Jesus Christ.

Chapter 1: Introduction and background

1.1 The standard model and flavor physics

The standard model, developed in 1960s, works well in the energy scale up to several hundreds of GeV. It unifies the three basic interactions, electromagnetic, strong and weak interactions and has successfully explained most of the experimental data we currently have. As the top quark (1995), the tau neutrino (2000), and the Higgs boson (2012) were detected, the validity of the standard model was further confirmed.

The electromagnetic sector of the model, is described by quantum electrodynamics(QED) which is the earliest part of the standard model to be proposed and which works very well with excellent agreement to very high precision between the experimental and theoretical results.

The strong sector is described by quantum chromodynamics(QCD). Because of asymptotic freedom, QCD perturbation theory works fairly well in the high-energy region. However, for energy close to the scale of Λ_{QCD} where the strong coupling α_s has a magnitude of order $\sim O(1)$, QCD perturbation theory does not converge and has uncontrolled contributions from high orders. The perturbation calculation in the low-energy region is limited by the computational challenges imposed by high-order perturbative terms. While in the low-energy region, experimental results are copiously generated and effective theories are quite successful in making predictions taking advantage of the approximate chiral symmetry of QCD, theoretical predictions from first-principle calculations based on the standard model are still limited.

The weak sector, which is the least understood part of the standard model, shows many intriguing properties like left-left only interactions, CP violation and quark mixing. In spite of the success of the standard model, there are some observations related to the weak sectors which need to be compared to the predictions by the standard model. These quantities may indicate new physics

beyond the standard model and the weak sector is expected to be the place where new physics may be discovered.

1.2 Neutral kaon mixing and Δm_K

Interesting quantities like the unitarity of the Cabibbo-Kobayashi-Maskawa(CKM) matrix and the CP violation parameters are being carefully measured in many weak-decay processes. Among them, flavor changing neutral current(FCNC) transitions are rare in the standard model and are sensitive to new physics.

The mass difference between the long- and short-lived K mesons, Δm_K, is generated by K meson mixing through $\Delta S = 2$ weak interaction which is a process second-order in the Fermi constant G_F and is closely related to the indirect CP violation parameter ϵ_K. This tiny quantity has been precisely measured experimentally to be $3.484(6) \times 10^{-12}$ MeV [4] and the comparison between the prediction for this quantity by the standard model and its experimental value will serve as a detector of new physics beyond the standard model.

However, like other weak decay quantities, for Δm_K one of the main difficulties in making a prediction based on the standard model is that the weak interactions are entangled with hadronic processes where the strong forces play a important role and one must handle the strong interactions non-perturbatively. In the previous calculations[3] [5], the division of short and long distance in the operator product expansion is made at an energy scale below the charm quark mass. The charm quark is treated perturbatively and the effective Hamiltonian is a local $\Delta S = 2$ operator. However, the result[5] from the calculation of the QCD correction factors using perturbation theory shows the next-to-next-to-leading-order(NNLO) terms are about 36 % of the leading order(LO) terms indicating a slow convergence of the perturbative series.

Due to the Glashow–Iliopoulos–Maiani(GIM) mechanism, the dominant contribution to Δm_K comes from the charm quark scale and below and the calculation can be better performed by making the division of long and short distances at an energy scale larger than the charm mass and treating the charm quark non-perturbatively by using two $\Delta S = 1$ operators in a lattice calculation.

With the improvement of lattice computational power in the past decades, this has recently become feasible. Since the first exploratory calculation[6] performed by the RBC-UKQCD collaboration on a 2+1 flavor, domain wall fermion (DWF), $16^3 \times 32 \times 16$ lattice ensemble with a 421 MeV pion, more developments in the calculation toward the complete prediction with physical quark masses have been achieved[1][7].

Our lattice calculation is based on first principles with well-controlled systematic errors. The finite lattice spacing errors can be estimated from a series of scaling tests with different lattice spacings. Ultimately one can perform calculations for several lattice spacings and extrapolate the results to the continuum limit. Corrections to the Δm_K due to the finite volume effects coming from the two-pion state scattering have been studied theoretically and we can use the formulas in Reference [8] to evaluate them for our calculation.

In this work, we will present the first lattice calculation of Δm_K based on the standard model with physical quark masses. In Chapter 2, we will have a brief review of the physics of the neutral kaon mixing in the standard model and explain our non-perturbative calculation of Δm_K using a renormalization scale above the charm quark mass. In Chapter 3, we will show the formalism and methods we have used to calculate Δm_K with lattice QCD. Chapter 4 further explains the data analysis methods we used to obtain physical quantities with well-estimated statistical errors. In Chapter 5, we will study several important sources of systematic errors, and show consistencies between the non-perturbative renormalization factors used in our Δm_K calculation and previous published results. We will also present a free-field calculation demonstrating the four-point contractions in our calculation method yield results consistent with the Inami-Lim calculation in the local limit[3]. In Chapter 6, we will present the results from our calculation of Δm_K on a $64^3 \times 128 \times 12$ lattice ensemble with physical quark masses. In Chapter 7, we will summarize our physical results and discuss the outlook for future comparisons between the prediction for Δm_K based on the standard model and its experimental value.

Chapter 2: The physics of Δm_K

In Nature, we find two types of neutral K meson with different masses and lifetimes. Δm_K, refers to the mass difference between the long- and short-lived K mesons. This mass difference is generated by the fact that the states with definite strangeness, i.e. K^0 and $\overline{K^0}$, are not the eigenstates of the weak Hamiltonian and they mix through second order weak interactions.

We can express the dynamics of the mixing using Wigner-Weisskopf theory:

$$i\frac{d}{dt}\begin{pmatrix} K^0(t) \\ \overline{K}^0(t) \end{pmatrix} = (M - \frac{i}{2}\Gamma)\begin{pmatrix} K^0(t) \\ \overline{K}^0(t) \end{pmatrix}, \tag{2.1}$$

where the matrices M and Γ are given by:

$$M_{ij} = m_K^{(0)}\delta_{ij} + \mathcal{P}\sum_n \frac{\langle K_i^0|H_W|n\rangle\langle n|H_W|K_j^0\rangle}{m_K - E_n}, \tag{2.2}$$

$$\Gamma_{ij} = 2\pi\sum_n \langle K_i^0|H_W|n\rangle\langle n|H_W|K_j^0\rangle\delta(m_K - E_n), \tag{2.3}$$

where the indices $i, j = 1, 2$ denote the K^0 and $\overline{K^0}$ states and H_W is the $\Delta S = 1$ effective weak Hamiltonian and the $\mathcal{P}$ denotes that a principal value will be taken when the integrand's denominator is vanishing.

The states K^0 and $\overline{K^0}$ are related by the CP transformation:

$$CP|\overline{K^0}\rangle = -|K^0\rangle, \tag{2.4}$$

and if we assume the CP invariance of the effective weak Hamiltonian, then the mass matrix are symmetrical and the matrix elements are real. If the small effects of CP violation are neglected then

the long-lived (K_L) and short-lived (K_S) are approximately the two CP odd and even eigenstates:

$$K_S \approx \frac{K^0 - \overline{K^0}}{\sqrt{2}}, \quad K_L \approx \frac{K^0 + \overline{K^0}}{\sqrt{2}}. \tag{2.5}$$

Therefore we obtain the key formula for the Δm_K calculation:

$$\Delta m_K \equiv m_{K_L} - m_{K_S} = 2ReM_{12} = 2\mathcal{P} \sum_n \frac{\langle \overline{K^0}|H_W|n\rangle\langle n|H_W|K^0\rangle}{m_K - E_n}. \tag{2.6}$$

Based on the standard model, the contribution to the Δm_K comes from box diagrams, double-penguin diagrams and disconnected diagrams. These diagrams are shown in Figure 2.1, 2.2 and 2.3. In order to perform the calculation, with a combination of perturbative and non-perturbative lattice calculations, long- and short-distance characteristics of each diagram have to be examined. Here we use the operator product expansion(OPE) method and the corresponding effective Hamiltonian to help us achieve this goal.

2.1 The operator product expansion(OPE) and Δm_K

The operator product expansion is commonly used in calculations of weak and hadronic processes and its general idea is to express the physics at a low energy scale in terms of an effective Hamiltonian, which is derived from the full theory by integrating out contributions from heavy particles above the low energy scale:

$$H_W = \sum_j C_j(\mu) O_j(\mu), \tag{2.7}$$

where the Wilson coefficients C_j contain the information from the high energy part which is integrated out from the original theory and the low energy part is preserved in the operators O_j. The renormalization scale μ labels the energy scale where the above division between high and low energies is made.

In a QCD-related problem, because of asymptotic freedom, i.e. that the QCD interaction be-

comes weak at a high energy scale μ and the strong coupling constant $\alpha_s(\mu) \ll 1$, the factor can be calculated perturbatively with high accuracy. The low energy part associated with the remaining operators should be treated non-perturbatively by performing lattice QCD simulations.

This is very useful since one can separate the calculation into two parts: the calculation of high-energy factors perturbatively and the calculation of the remaining low-energy matrix elements non-perturbatively with well-controlled systematic errors in each part. The choice of energy scale μ is somewhat arbitrary but in order to reduce the systematic errors from perturbative and non-perturbative calculations, one usually make the scale μ to obey:

$$\frac{1}{a} \gg \mu \gg \Lambda_{QCD}, \tag{2.8}$$

where a is the lattice spacing and Λ_{QCD} is the typical energy scale where $\alpha_s(\Lambda_{QCD}) \sim 1$. Therefore, the low energy part is then called to be "long-distance" and the high energy part is called to be "short-distance", based on the reciprocal relationship between the typical energy and distance scale of the interactions.

The above condition shown in Equation 2.8 is a rather generic one. To choose a proper μ suitable for a specific problem, one has to take into consideration the limit of the available lattice ensembles, computational costs and the corresponding systematic errors introduced by perturbative and non-perturbative calculations. These restrictions themselves are evolving as the developments of lattice QCD are still going on, especially when the lattices with smaller lattice spacings are being generated, and supercomputers with stronger computational power are becoming accessible. At the same time, as the perturbative calculation extends to larger number of orders, the lower bound of the energy scale μ can be taken smaller. Therefore, the division of short- and long-distance calculation, may vary among different methods and different times in history.

Here using the OPE, we will firstly summarize an earlier method to calculate Δm_K[3][9] [5]. By examining the short- and long-distance characteristics of Δm_K calculation and taking the current available computational resources into consideration, we will present our choice of the short- and long-distance division for our full calculation of Δm_K on a lattice with physical quark masses.

2.2 GIM mechanism: short- and long-distance characteristics of Δm_K

The GIM mechanims plays an important role in the kaon-mixing problem. The internal quark lines with different flavors, i.e. up, charm, top, will appear in the diagrams. We start from the $\Delta S = 1$ effective Hamiltonian:

$$H_W = \frac{G_F}{\sqrt{2}} \sum_{q,q'=u,c,t} V_{qd} V^*_{q's} (C_1 Q_1^{qq'} + C_2 Q_2^{qq'}). \tag{2.9}$$

Here $Q_i^{qq'}{}_{i=1,2}$ are current-current operators, defined as:

$$Q_1^{qq'} = (\bar{s}_i \gamma^\mu (1-\gamma_5) d_i)(\bar{q}_j \gamma^\mu (1-\gamma_5) q'_j), \quad Q_2^{qq'} = (\bar{s}_i \gamma^\mu (1-\gamma_5) d_j)(\bar{q}_j \gamma^\mu (1-\gamma_5) q'_i), \tag{2.10}$$

where i and j denote the color indices of the quark fields. As a $\Delta S = 2$ process, the kaon mixing has two $\Delta S = 1$ weak operators involved and if we perform the Wick contractions, for a specific diagram labeled as $\textcircled{\text{X}}$, we will find:

$$\textcircled{\text{X}}_{GIM} = \lambda_u^2 \textcircled{\text{X}}^{uu} + \lambda_c^2 \textcircled{\text{X}}^{cc} + \lambda_t^2 \textcircled{\text{X}}^{tt} + \lambda_u\lambda_c(\textcircled{\text{X}}^{uc} + \textcircled{\text{X}}^{cu}) + \lambda_u\lambda_t(\textcircled{\text{X}}^{ut} + \textcircled{\text{X}}^{tu}) + \lambda_t\lambda_c(\textcircled{\text{X}}^{tc} + \textcircled{\text{X}}^{ct}), \tag{2.11}$$

where the upper index shows the flavors of the two internal contracted quark lines. Based on the unitarity of the CKM matrix, we have:

$$\lambda_u + \lambda_c + \lambda_t = 0, \tag{2.12}$$

where $\lambda_q = V_{q,d} V^*_{q,s}$, $q = u, c, t$, and we can rewrite the Equation 2.11 for example by eliminating $\lambda_c = -\lambda_u - \lambda_t$ and simplify it to be:

$$\textcircled{\text{X}}_{GIM} = \lambda_u^2 \textcircled{\text{X}}^{(u-c)(u-c)} + \lambda_t^2 \textcircled{\text{X}}^{(t-c)(t-c)} + 2\lambda_u\lambda_t \textcircled{\text{X}}^{(u-c)(t-c)}, \tag{2.13}$$

where the $(q-c)$, with $q = u, t$, denotes that the internal quark line with flavor q are subtracted by a quark line with flavor charm. We can see that all the diagrams will vanish if up, charm and top quarks have degenerate masses, which is just what the GIM mechanism predicts.

Therefore, including the effect of the GIM mechanism on the diagrams can be effectively considered as subtracting one of the quark flavors from each quark lines in the diagrams which are built with the other two flavors. Given such formalism to include the GIM mechanism, we can further examine the long- and short-distance characteristics of each sub-diagram, in the context of the OPE.

2.2.1 Calculation of Δm_K from the bag parameter B_K

In the earlier calculation of Δm_K[5], one uses $\lambda_u = -\lambda_c - \lambda_t$ to eliminate λ_u and obtains the expression:

$$\text{(X)}_{GIM} = \lambda_c^2 \text{(X)}^{(c-u)(c-u)} + \lambda_t^2 \text{(X)}^{(t-u)(t-u)} + 2\lambda_c\lambda_t \text{(X)}^{(c-u)(t-u)}. \tag{2.14}$$

In Reference [5], the division of short and long distance is made at an energy scale below the charm quark mass. As a result, the contributions from box diagrams related to charm quarks belongs to the short-distance region and the remaining mixing channels like $K^0 \leftrightarrow (\pi^0, \eta) \leftrightarrow \overline{K^0}$ and $K^0 \leftrightarrow \pi\pi \leftrightarrow \overline{K^0}$ are assigned to be long-distance and remain unresolved. The double-penguin diagrams, have both short-distance and long-distance contributions under this division. It's difficult to separate the two, and only the short-distance contribution has been studied[10].

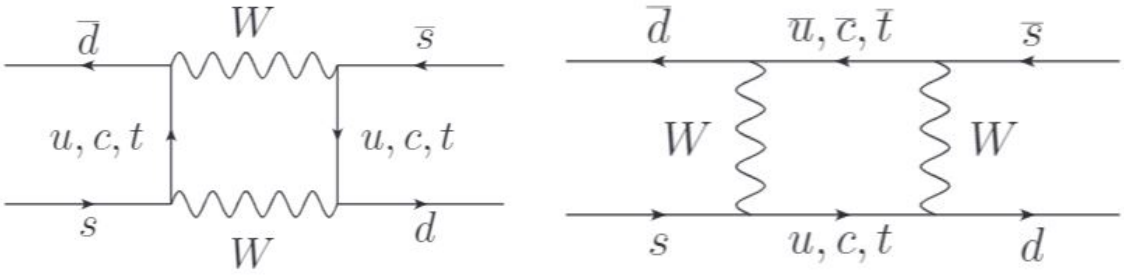

Figure 2.1: Contribution to Δm_K from box diagrams.

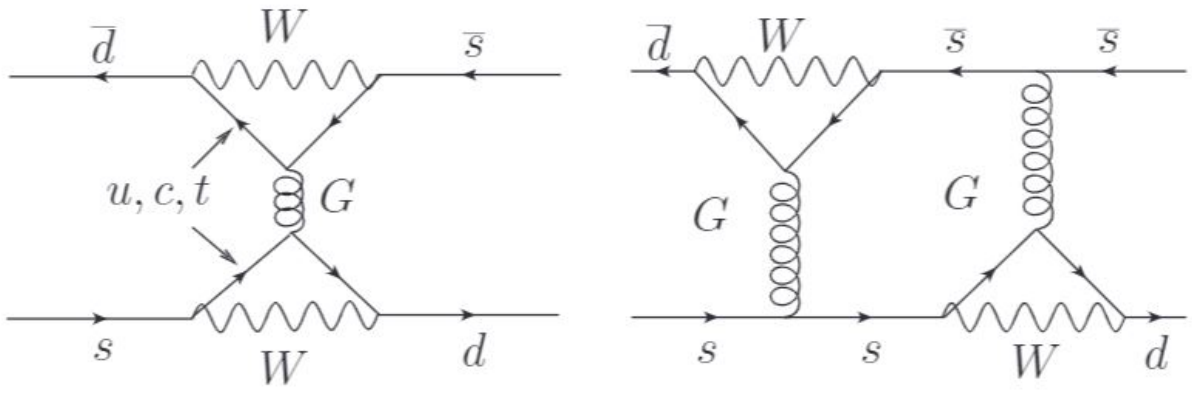

Figure 2.2: Contribution to Δm_K from double-penguin diagrams.

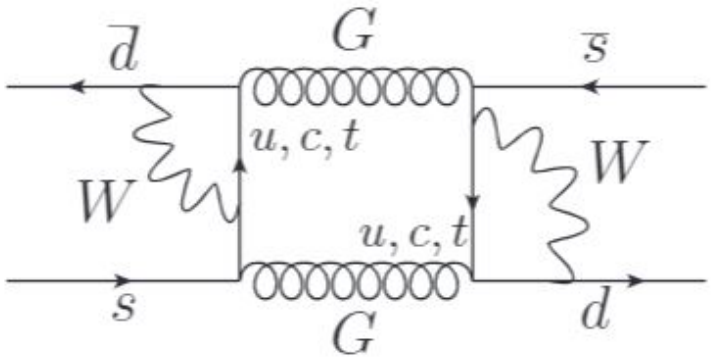

Figure 2.3: Contribution to Δm_K from disconnected diagrams.

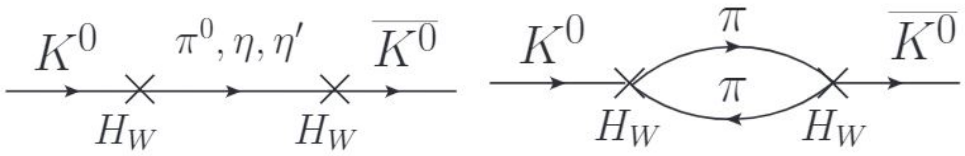

Figure 2.4: Contribution to Δm_K from long-distance diagrams according to the division when $\mu < m_c$.

For the short-distance part, the charm quark contribution is integrated out and calculated perturbatively. The effective Hamiltonian from box diagrams can be expressed in terms of a $\Delta S = 2$ local operator multiplied by a Wilson coefficient from weak and short-distance QCD effects:

$$\mathcal{H}_{eff}^{\Delta S=2} = \frac{G_F^2}{16\pi^2} M_W^2 [\lambda_c^2 \eta_1 S_0(x_c) + \lambda_t^2 \eta_1 S_0(x_t) + 2\lambda_c \lambda_t \eta_3 S_0(x_c, x_t)] \times [\alpha_s(\mu)]^{-\frac{2}{9}} [1 + \frac{\alpha_s(\mu)}{4\pi} J_3] O_{LL} + h.c., \tag{2.15}$$

where $x_i = \frac{m_i^2}{M_W^2}$, $x_i = u, c, t$ and x_u is set to be 0. The local operator is given by:

$$O_{LL} = (\bar{s}d)_{V-A} (\bar{s}d)_{V-A}, \tag{2.16}$$

where $(V - A)$ denotes the left-handed spin structure of the form $\gamma_\mu(1 - \gamma_5)$. The non-perturbative calculation focuses on the evaluation of the matrix element $\langle K^0 | O_{LL} | \overline{K^0} \rangle$. Note that here our normalization convention is $\langle K^0(\vec{p}_1) | K^0(\vec{p}_2) \rangle = 2E(2\pi)^3 \delta^3(\vec{p}_1 - \vec{p}_2)$ and different from the convention used in our finite-volume lattice calculation which can be found in Appendix A. Practically, we calculate the scale- and scheme-invariant bag parameter:

$$\hat{B}_K = \frac{3}{8} \frac{\langle \overline{K^0} | b(\mu) O_{LL}(\mu) | K^0 \rangle}{F_K^2 m_K^2}, \tag{2.17}$$

where F_K is the kaon decay constant and $b(\mu)$ is the renormalized Wilson factor at energy scale μ. The S_0 functions, are the Inami-Lim functions which comes from the electroweak box diagram without QCD correction:

$$S_0(x_c) \approx x_c, \quad x_c \ll 1, \tag{2.18}$$

$$S_0(x_t) = \frac{4x_t - 11x_t^2 + x_t^3}{4(1 - x_t)^2} - \frac{3x_t^3 \ln x_t}{2(1 - x_t)^3}, \tag{2.19}$$

$$S_0(x_c, x_t) = x_c [\ln \frac{x_t}{x_c} - \frac{3x_t}{4(1 - x_t)} - \frac{3x_t^2 \ln x_t}{4(1 - x_t)^2}]. \tag{2.20}$$

The short-distance QCD correction based on perturbation theory are expressed by the combi-

nations of the factors η_1, η_2, η_3 which are α_s-dependent terms. Finally, Δm_K can be calculated using the formula:

$$\Delta m_K = \frac{G_F^2}{6\pi^2} M_W^2 F_K^2 \hat{B}_K m_K [\lambda_c^2 \eta_1 S_0(x_c) + \lambda_t^2 \eta_1 S_0(x_t) + 2\lambda_c \lambda_t \eta_3 S_0(x_c, x_t)]. \tag{2.21}$$

By calculating B_K non-perturbatively, we can obtain a value of the short-distance contribution to Δm_K, by leaving out the contributions from long distance, based on the specific division $\mu < m_c$ where charm quark is integrated out. However, the result[5] shows only 36% accuracy in the next-to-next-to-leading-order(NNLO) calculation of the QCD correction factors using perturbation theory and indicates a slow convergence of the perturbative series. Therefore, treating charm quark non-perturbatively on the lattice provides an alternative way with well-controlled systematic errors and enables us to calculate the full contribution from all types of diagrams.

2.2.2 Non-perturbative calculation of Δm_K using a renormalization scale above the charm quark mass

With the improvement of lattice computational power, treating the charm quark non-perturbatively becomes feasible and we can perform the division of long and short distances at an energy scale larger than the charm mass. Therefore, under this division, the contributions from up and charm quarks are now all long-distance and we will see later in this chapter that the GIM mechanism also ensures that the Δm_K computed in this way on the lattice has a physical continuum limit.

We will start from the $\Delta S = 1$ effective Hamiltonian and eliminate λ_c in Equation 2.11. Using $\lambda_c = -\lambda_u - \lambda_t$, we obtain the contracted diagram $\textcircled{\text{X}}_{GIM}$ for any topology X with the GIM mechanism included:

$$\textcircled{\text{X}}_{GIM} = \lambda_u^2 \textcircled{\text{X}}^{(u-c)(u-c)} + \lambda_t^2 \textcircled{\text{X}}^{(t-c)(t-c)} + 2\lambda_u \lambda_t \textcircled{\text{X}}^{(u-c)(t-c)}, \tag{2.22}$$

where the $(q-c)$, with $q = u, t$, denotes that the internal quark lines with flavor q have a charm quark line subtracted.

Because only the real part of matrix element M_{12} contributes to Δm_K, we can examine the numerical values of the coefficients λ_u^2, λ_t^2 and $\lambda_u\lambda_t$ and estimate the overall contributions to the real part of matrix element M_{12} from each sub-diagram $\textcircled{X}^{(q-c)(q'-c)}$. At the same time, we should also examine the long- and short-distance characteristics of each sub-diagram $\textcircled{X}^{(q-c)(q'-c)}$ and decide whether the quark flavors q and q' should be treated non-perturbatively.

Detailed discussion about these two important aspects can be found in [11]. Following that discussion, we will focus on the diagrams with the (u-c)(u-c) flavor structure and include contributions from all possible diagrams, i.e. the box diagrams, double-penguin diagrams and disconnected diagrams.

2.3 Calculation of the diagrams with two bi-local $\Delta S = 1$ operators on the lattice

On the lattice, due to the discretization, we don't naturally have a continuous space-time integral, and the contribution from the distance at the lattice scale is dominated by lattice artifacts. For a calculation of physical quantities on the lattice, such effects should be considered as a well-controlled source of systematic errors and in the limit where lattice spacing a goes to 0, physical continuum results should be obtained. Therefore, before we move on and implement the calculation of the diagrams on the lattice, we have to confirm that our Δm_K computed on the lattice corresponds to a physical quantity with well-defined continuum limit.

The inner loops in the box diagrams or self-loops in the penguin and disconnected diagrams may lead to ultra-violet divergences and the lattice calculation as a result may have no well-defined continuum limit. However, as we can see below, the GIM mechanism and the left-left spin structure of the two current-current weak operators remove the divergence and the quantities we calculate on the lattice for Δm_K are well defined once the four quark operators themselves have been properly renormalized.

Here we start our discussion with Δm_K calculated from diagrams from two $\Delta S = 1$ weak operators evaluated in momentum space. If we simply perform the calculation where charm quark is integrated out, the loop integrals are divergent. This can be understood by writing down the

QCD-free loop integral appearing in the diagrams, regulated by the lattice cutoff a^{-1}:

$$\int_{m_u}^{a^{-1}} d^4p \Big[\gamma^\mu(1-\gamma_5)\frac{\not{p}-m_u}{\not{p}^2+m_u^2}\gamma^\nu(1-\gamma_5)\frac{\not{p}-m_u}{\not{p}^2+m_u^2}\Big]\Big[...\Big]_{\nu,\mu}, \tag{2.23}$$

or equivalently using the gamma matrix properties, we can write the integral as:

$$\int_{m_u}^{a^{-1}} d^4p \Big[\gamma^\mu(1-\gamma_5)\frac{\not{p}}{\not{p}^2+m_u^2}\gamma^\nu(1-\gamma_5)\frac{\not{p}}{\not{p}^2+m_u^2}\Big]\Big[...\Big]_{\nu,\mu}, \tag{2.24}$$

where the $\Big[...\Big]_{\nu,\mu}$ denotes a similar spinor product as in the brackets on its left. By naive power counting, we can see the integral diverges in a quadratic manner as $a \to 0$.

However, under our division of the short- and long-distance contribution where the charm quark is treated non-perturbatively, the GIM mechanism leads to the $(u-c)$ flavor structure in the inner loops of the diagrams. With the charm quark and GIM cancellation, we have the expression below for an inner loop integral with the $(u-c)$ flavor structure:

$$\int_{m_c}^{a^{-1}} d^4p \Big[\gamma^\mu(1-\gamma_5)\Big(\frac{\not{p}-m_u}{\not{p}^2+m_u^2}-\frac{\not{p}-m_c}{\not{p}^2+m_c^2}\Big)\gamma^\nu(1-\gamma_5)\Big]\Big[(... - ...)\Big]_{\nu,\mu}, \tag{2.25}$$

where a^{-1} suggest the lattice cutoff of the momentum integral. Because of the left-left spin structure of the current-current operator, the term leading to logarithmic divergence vanishes and we obtain:

$$\int_{m_c}^{a^{-1}} d^4p \Big[\gamma^\mu(1-\gamma_5)\Big(\frac{\not{p}(m_c^2-m_u^2)}{(\not{p}^2+m_u^2)(\not{p}^2+m_c^2)}\Big)\gamma^\nu(1-\gamma_5)\Big]\Big[(... - ...)\Big]_{\nu,\mu}. \tag{2.26}$$

As the result, we will have a convergent integral with the dominate contribution coming from the distance $\sim 1/m_c$, rather than a divergent integral as $a \to 0$. Therefore, our Δm_K lattice calculation is well-defined in the continuum limit and we can reduce the systematic errors from the finite lattice spacing by using a lattice with a smaller lattice spacing.

In our calculation on the $64^3 \times 128$ lattice ensemble with physical quark masses, we have $a^{-1} = 2.36$GeV and $m_c a = 0.31$ and our discussion of the finite lattice spacing effects coming from direct scaling tests is included in Chapter 5.

Chapter 3: Calculation of Δm_K with lattice QCD

The previous chapter demonstrates that Δm_K is a long-distance quantity which can be calculated on the lattice with a well-defined physical continuum limit. In this chapter we will show the details about how we calculate Δm_K using lattice QCD. We will first explain the quantities from which we extract the value of Δm_K and then the implementation of the calculations of these quantities. Lastly, the non-perturbative renormalization which connects the lattice value of Δm_K to the physical value will be demonstrated.

3.1 Δm_K and integrated correlation functions

The kaon mixing process can be studied using lattice QCD by calculating four-point correlation functions. As shown below in Figure 3.1, we can evaluate such a correlation function by putting a K^0 creation operator at time t_i and a $\overline{K^0}$ annihilation operator at time t_f and inserting two effective weak Hamiltonian operators at time t_1 and t_2.

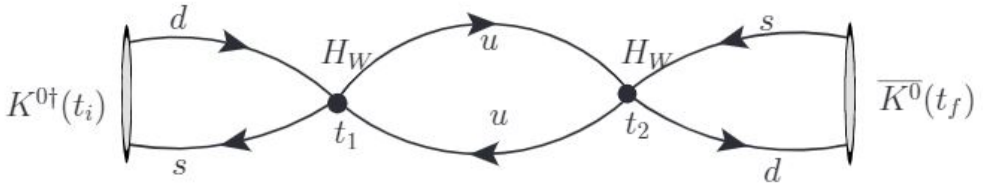

Figure 3.1: A four-point correlator on the lattice.

The correlation function is given by:

$$G(t_1, t_2, t_i, t_f) \equiv \langle 0|\mathrm{T}\{\overline{K^0}(t_f)H_W(t_2)H_W(t_1)K^0(t_i)\}|0\rangle, \tag{3.1}$$

where T{...} means the time ordering of the operators is imposed. If we insert a complete set of

intermediate states, it can be expressed as:

$$G(\delta) = N_K^2 e^{-m_K(t_f - t_i)} \sum_n \langle \overline{K^0} | H_W | n \rangle \langle n | H_W | K^0 \rangle e^{(m_K - E_n)\delta}, \tag{3.2}$$

where $\delta = t_2 - t_1$ is the time difference between the two weak operators and N_K is the normalization factor for the kaon interpolating operators $\overline{K^0}(t_f)$ and $K^0(t_i)$.

To calculate Δm_K we can integrate the four-point correlation functions over the time locations of one of the weak operators with the other one being fixed as shown in Figure 3.2 and obtain the single-integrated correlator:

$$\mathcal{A}^S(T) = \frac{1}{2!} \sum_{t_2 = t_1 - T}^{t_1 + T} \langle 0 | T\{\overline{K^0}(t_f) H_W(t_2) H_W(t_1) K^0(t_i)\} | 0 \rangle. \tag{3.3}$$

which is connected to the correlation function G by:

$$\begin{aligned} \mathcal{A}^S(T) &= \frac{1}{2!} \sum_{t_2 = t_1 - T}^{t_1 + T} \langle 0 | T\{\overline{K^0}(t_f = t_i + \Delta) H_W(t_2) H_W(t_1) K^0(t_i)\} | 0 \rangle \\ &= \sum_{\delta=1}^{T} G(t_1, t_2 = t_1 + \delta, t_i, t_f = t_i + \Delta) + \frac{1}{2} G(t_1, t_2 = t_1, t_i, t_f = t_i + \Delta). \end{aligned} \tag{3.4}$$

If we insert a complete set of intermediate states between the weak operators H_W in Equation 3.3 and drop terms of order a^2 in the sums, we find:

$$\mathcal{A}^S(T) = N_K^2 e^{-m_K(t_f - t_i)} \sum_n \frac{\langle \overline{K^0} | H_W | n \rangle \langle n | H_W | K^0 \rangle}{m_K - E_n} \{-1 + e^{-(E_n - m_K)T}\}. \tag{3.5}$$

We obtain Δm_K from the constant term in Equation 3.5, after we remove the term with exponential dependence on T.

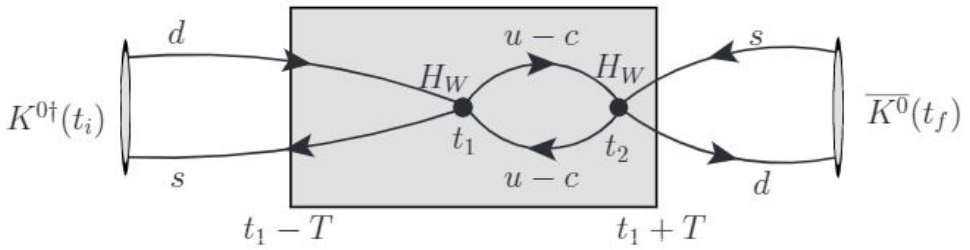

Figure 3.2: The single integration method on the lattice. The shadowed box refers to the region of integration.

3.1.1 Three point matrix elements for subtraction of terms with exponential time growth

The term $\mathcal{E}$ with exponential dependence on T which we need to be removed from $\mathcal{A}^S$ is:

$$\mathcal{E} = N_K^2 e^{-m_K(t_f - t_i)} \sum_n \frac{\langle \overline{K^0}|H_W|n\rangle\langle n|H_W|K^0\rangle}{m_K - E_n} e^{-(E_n - m_K)T}. \tag{3.6}$$

The contributions from the states $|n\rangle$ with $E_n > m_K$, are negligible at large T values. However, the contributions coming from states $|n\rangle$ with $E_n < m_K$ increase exponentially as T becomes larger and we need to calculate their contribution:

$$\mathcal{E}_n = \frac{\langle \overline{K^0}|H_W|n\rangle\langle n|H_W|K^0\rangle}{m_K - E_n} e^{-(E_n - m_K)T}, \tag{3.7}$$

and subtract them from the $\mathcal{A}^S$. Therefore we need to calculate the matrix elements: $\langle \overline{K^0}|H_W|n\rangle$, $\langle n|H_W|K^0\rangle$ and the energies E_n of the low-energy states.

In our case of physical quark masses, the vacuum state $|0\rangle$, single-pion state $|\pi\rangle$, two-pion state $|\pi\pi\rangle$ each have energy smaller than m_K and their contributions need to be subtracted. The single-eta state $|\eta\rangle$ has an energy slightly larger than m_K and its contribution proportional to $e^{-(m_\eta - m_K)T}$, may not be negligible. Therefore we will also subtract the contribution from single-eta state.

Because operators $\bar{s}d$ and $\bar{s}\gamma_5 d$ can be written as a total divergence, we have the freedom to add these two operators with coefficients c_s and c_p to our effective Hamiltonian without changing the final results. With properly chosen coefficients c_s and c_p, we are able to remove two of these contributions.

The kaon to η matrix element is expected to be very noisy since it includes disconnected diagrams. Here we choose $c_{\rm s}$ and $c_{\rm p}$ to satisfy Equation 3.8 so that contributions from the $|0\rangle$ and $|\eta\rangle$ will vanish:

$$\langle 0|H_W - c_{\rm p}\bar{s}\gamma_5 d|K^0\rangle = 0, \quad \langle \eta|H_W - c_{\rm s}\bar{s}d|K^0\rangle = 0. \tag{3.8}$$

As a result, the current-current operators Q_i in the original $\Delta S = 1$ effective weak Hamiltonian should be modified to be :

$$Q_i' = Q_i - c_{{\rm p}i}\bar{s}\gamma_5 d - c_{{\rm s}i}\bar{s}d \tag{3.9}$$

with $c_{{\rm p}i}$ and $c_{{\rm s}i}$ being calculated on the lattice from the ratios of the matrix elements:

$$c_{{\rm s}i} = \frac{\langle \eta|Q_i|K^0\rangle}{\langle \eta|\bar{s}d|K^0\rangle}, \quad c_{{\rm p}i} = \frac{\langle 0|Q_i|K^0\rangle}{\langle 0|\bar{s}\gamma_5 d|K^0\rangle}. \tag{3.10}$$

With the choice shown in Equation 4.10, we can reduce the size of statistical error from the noisy states by taking advantage of the correlation between the denominators and the numerators in Equation 4.10 and we only need to subtract less noisy contributions from the other two states explicitly.

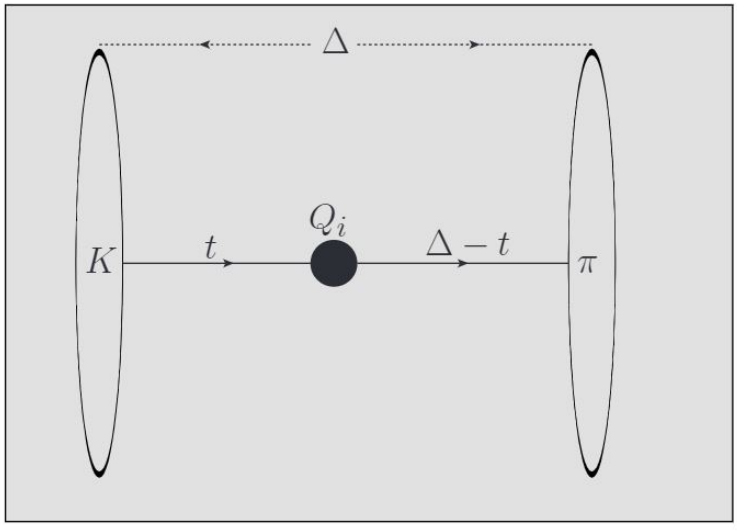

Figure 3.3: The three-point correlation function with a kaon source and a pion sink.

We can extract the matrix elements from the three-point correlation functions. For example, a

three-point correlation function with a kaon source and a pion sink is shown in Figure 3.3. The three-point correlation function is given by:

$$C^{Q_i}(\Delta, t) = \langle 0|O^{\dagger}_{\pi^0}(\Delta)Q_i(t)O_{K^0}(0)|0\rangle \tag{3.11}$$

$$= \sum_n \sum_m \langle 0|e^{H\Delta}O^{\dagger}_{\pi^0}(0)e^{-H\Delta}|n\rangle\langle n|e^{Ht}Q_i(0)e^{-Ht}|m\rangle\langle m|O_{K^0}|0\rangle \tag{3.12}$$

$$= \sum_n \sum_m \langle 0|O^{\dagger}_{\pi^0}(0)|n\rangle\langle n|Q_i(0)|m\rangle\langle m|O_{K^0}|0\rangle e^{-E_n(\Delta-t)}e^{-E_m t} \tag{3.13}$$

where Δ is the time distance between the kaon creation operator and the pion annihilation operator and t is the time distance from the kaon operator to the weak operator. $O_{K^0}(0)$ denotes a kaon creation operator at time 0 and $O^{\dagger}_{\pi^0}$ denotes a pion annihilation operator at time Δ.

Since the sum over m is dominated by kaon ground state for large enough t and the sum over n is dominated by pion ground state for large enough $(\Delta - t)$, we can further simplify above expression to:

$$\begin{aligned} C^{Q_i}(\Delta, t) &\approx \langle 0|O^{\dagger}_{\pi^0}(0)|\pi^0\rangle\langle\pi^0|Q_i|K^0\rangle\langle K^0|O_{K^0}|0\rangle e^{-m_\pi(\Delta-t)}e^{-m_K t} \\ &= N_\pi N_K \langle\pi^0|Q_i|K^0\rangle e^{-m_\pi(\Delta-t)}e^{-m_K t} \end{aligned} \tag{3.14}$$

We can extract the term $\langle\pi^0|Q_i(0)|K^0\rangle$ from $C^{Q_i}(\Delta, t)$ if we obtain factors like $\langle 0|O^{\dagger}_{\pi^0}(0)|\pi^0\rangle$, $\langle K^0|O_{K^0}|0\rangle$ and the meson masses from two-point correlation functions.

3.1.2 Two-point correlation functions for masses and normalization factors

The masses and normalization factors of meson states can be obtained from two-point correlation functions. Using the case of the kaon source and kaon sink as an example, the two-point correlation function, is of the form:

$$C^{2\text{pt}}_{K^0}(t) = \langle 0|O^{\dagger}_{K^0}(t)O_{K^0}(0)|0\rangle = \sum_n |\langle n|O^{\dagger}_{K^0}|0\rangle|^2 e^{-E_n t}. \tag{3.15}$$

The term which dominates the sum is the one with non-zero $|\langle n|O^{\dagger}_{K^0}|0\rangle|$ and relatively large $e^{-E_n t}$. There are kaon excited states which can have non-zero $|\langle n|O^{\dagger}_{K^0}|0\rangle|$ value. However for large t, the lowest non-zero state, i.e. the kaon ground state dominates; so we have an approximate expression:

$$C^{2\text{pt}}_{K^0}(t) \approx |\langle K^0|O^{\dagger}_{K^0}|0\rangle|^2 e^{-m_K t} \tag{3.16}$$

Thus we can obtain $|\langle K^0|O^{\dagger}_{K^0}|0\rangle|^2$ and m_K from fitting this expression and can then remove the time-dependence and normalization factors from the related three-point correlation functions.

3.2 Operators and Wick contractions

The $K_L - K_S$ mass difference can be calculated from the four-point correlators as shown in Equation 3.3. Based on our OPE division, after neglecting the contribution from the top quark, the $\Delta S = 1$ effective Hamiltonian H_W can be expressed as:

$$H_W = \frac{G_F}{\sqrt{2}} \sum_{q,q'=u,c} V_{qd} V^*_{q's} (C_1 Q_1^{qq'} + C_2 Q_2^{qq'}), \tag{3.17}$$

and $Q_i^{qq'}{}_{i=1,2}$ are current-current operators which contribute to Δm_K, and are defined as:

$$Q_1^{qq'} = (\bar{s}_i \gamma^\mu (1-\gamma_5) d_i)(\bar{q}_j \gamma^\mu (1-\gamma_5) q'_j), \quad Q_2^{qq'} = (\bar{s}_i \gamma^\mu (1-\gamma_5) d_j)(\bar{q}_j \gamma^\mu (1-\gamma_5) q'_i). \tag{3.18}$$

By taking advantage of the Fierz identity, we can write the operator Q_2 in a color-diagonal form:

$$Q_2^{qq'} = (\bar{s}_i \gamma^\mu (1-\gamma_5) q'_i)(\bar{q}_j \gamma^\mu (1-\gamma_5) d_j). \tag{3.19}$$

The effective weak Hamiltonian, using $Q_i^{qq'}$ as defined in Equation 3.18, can be explicitly written as:

$$H_W = \frac{G_F}{\sqrt{2}} \Big[\cos\theta_c \sin\theta_c C_i (Q_i^{uu} - Q_i^{cc}) + \cos^2\theta_c (C_i Q_i^{uc}) - \sin^2\theta_c (C_i Q_i^{cu}) \Big], \tag{3.20}$$

where θ_c is the Cabibbo angle since we have top contribution omitted based on the discussion in Chapter 2.

In addition to these weak operators, we must include meson source and sink operators as well. The contractions among these meson operators and the effective weak operators yield the correlation functions from which we would like to extract matrix elements. To have a better overlap with the meson ground state, we use Coulomb gauge-fixed wall source and sink operators to create the K^0 and destroy the $\overline{K}^0$. The meson operators are of the form, using kaon operator as an example:

$$O_{K^0}(t) \equiv K^0(t) = \sum_{\vec{x},\vec{y}} i\bar{d}(\vec{x},t)V(\vec{x},t)\gamma_5 V^\dagger(\vec{y},t)s(\vec{y},t), \tag{3.21}$$

where the sum over $\vec{x}$ and $\vec{y}$ in the spacial hyperplane at time t leads to wall source propagators and the V transforms the gauge links in the spatial hyperplane into Coulomb gauge.

The η meson operator seems to be more complicated because the η and η' mesons are mixtures of the octet state η_8 and the singlet state η_1 under the SU(3) symmetry. The mixing of these two states can be expressed in terms of the mixing angle θ as:

$$\begin{pmatrix} |\eta\rangle \\ |\eta'\rangle \end{pmatrix} = \begin{pmatrix} cos\theta & -sin\theta \\ sin\theta & cos\theta \end{pmatrix} \begin{pmatrix} |\eta_8\rangle \\ |\eta_1\rangle \end{pmatrix}, \tag{3.22}$$

where $|\eta_8\rangle$ and $|\eta_1\rangle$ are obtained by applying the operators:

$$|\eta_8\rangle = \frac{1}{\sqrt{6}}(\overline{u}\gamma_5 u + \overline{d}\gamma_5 d - 2\overline{s}\gamma_5 s)|0\rangle \tag{3.23}$$

$$|\eta_1\rangle = \frac{1}{\sqrt{6}}(\overline{u}\gamma_5 u + \overline{d}\gamma_5 d + \overline{s}\gamma_5 s)|0\rangle \tag{3.24}$$

In our calculation, because θ is small and the systematic error from omitting $|\eta_1\rangle$ is negligible, we take the $|\eta_8\rangle$ as the η state appearing in the three-point matrix elements .

Four-point contractions

We must evaluate the four-point correlation functions $\langle 0|\mathrm{T}\{\overline{K^0}(t_f)H_W(t_2)H_W(t_1)K^0(t_i)\}|0\rangle$ by performing Wick contractions between the operators. There are four types of topology for the contractions between the current-current operators and meson operators as shown in Figure 3.4. In addition to these diagrams, there are also diagrams which contain contractions between the lower dimensional operators $\bar{s}d$, $\bar{s}\gamma_5 d$ and the current-current operators Q_i, as shown in Figure 3.5. Because these diagrams have similar topologies to those of the type-3 and type-4 diagrams, we assign them to the category of type-3 and type-4 diagrams when we separate and evaluate the contributions from the different types of diagrams to Δm_K.

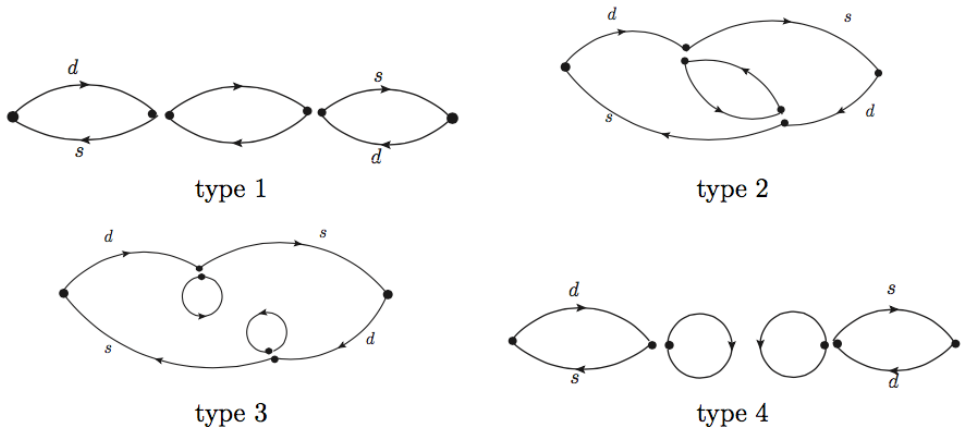

Figure 3.4: Four types of contractions in the 4-point correlators with Q_1 and Q_2. All the internal loops have the (u-c)(u-c) flavor structure because of the GIM mechanism.The single dots correspond to the K^0 and $\overline{K}^0$ operators while the paired dots correspond to the weak four-quark operator.

For the inner propagators, because of GIM mechanism, we will have the (u-c)(u-c) flavor structure, which can be deduced from the operators in Equation 3.20. Because of the GIM mechanism, we can combine groups of four-point diagrams $\boxed{\mathrm{X}}$, to realize a (u-c)(u-c) flavor structure for all internal quark lines with a common factor $\cos\theta_c\sin\theta_c$:

$$\boxed{\mathrm{X}}_{GIM} = \cos\theta_c\sin\theta_c\boxed{\mathrm{X}}^{(u-c)(u-c)}. \tag{3.25}$$

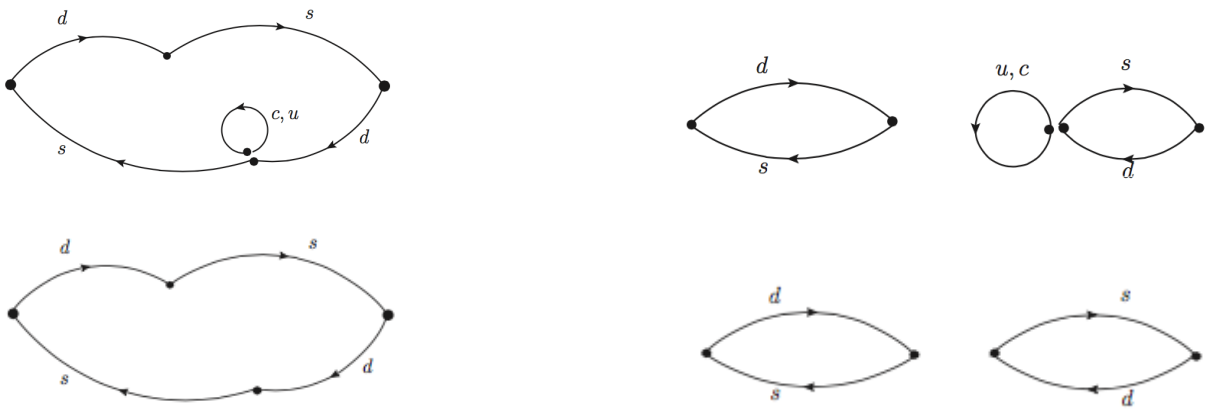

Figure 3.5: The "mixed" contractions in the 4-point correlators. The top two are products of the $c_{si}\bar{s}d$ and $c_{pi}\bar{s}\gamma_5 d$ contracted with the Q_i and the bottom two are products of the $c_{si}\bar{s}d$ and $c_{pi}\bar{s}\gamma_5 d$ operators. The diagrams on the left and the type-3 diagrams have a similar topology. The diagrams on the right and the type-4 diagrams also have a similar topology.

After the Wick contractions are specified, each group of diagrams can be calculated in terms of specific products of propagators. For example, a typical four-point diagram labeled with index 2 shown in Figure C.1 can be explicitly calculated as:

$$\textcircled{2}_{GIM} = Tr\Big[\Gamma^{\mu} S_d^W(x,t_i)\gamma_5 [S_s^W(x,t_i)]^{-1}\Gamma_{\mu}[S^P_{(u-c)}(y,x)]^{-1}\Gamma^{\nu} S_d^W(y,t_f)\gamma_5[S_s^W(y,t_f)]^{-1}\Gamma_{\nu}S^P_{(u-c)}(y,x)\Big], \tag{3.26}$$

where $\Gamma^{\mu} = \gamma^{\mu}(1-\gamma_5)$, $[...]^{-1}$ denotes a propagator with the opposite direction and $Tr[...]$ means taking trace over spin and color indices. The propagator notations are defined here as followings: $S_q^W(x,t)$ means a propagator with a wall source on time slice t and a point sink on space-time site x and $S_q^P(y,x)$ means a propagator with a point source on site x and a point sink on site y and the subscript q denotes the quark flavor. The flavor structure is labeled by $q = s, d$. The $S^P_{(u-c)}(x,y)$ represents a point-source-point-sink propagator with flavor up subtracted by the same type of propagator with flavor charm.

Three-point contractions

We have to calculate three-point correlation functions between the kaon state and light states to extract the matrix elements of the form $\langle n|Q_i|K^0\rangle$, $\langle n|\bar{s}d|K^0\rangle$ and $\langle n|\bar{s}\gamma_5 d|K^0\rangle$. The three-point

contractions can be roughly categorized into two types of diagrams, figure-eight and eye diagrams with self-loop propagators, as shown in Figure 3.6. All the three-point diagrams are listed in the Appendix C.

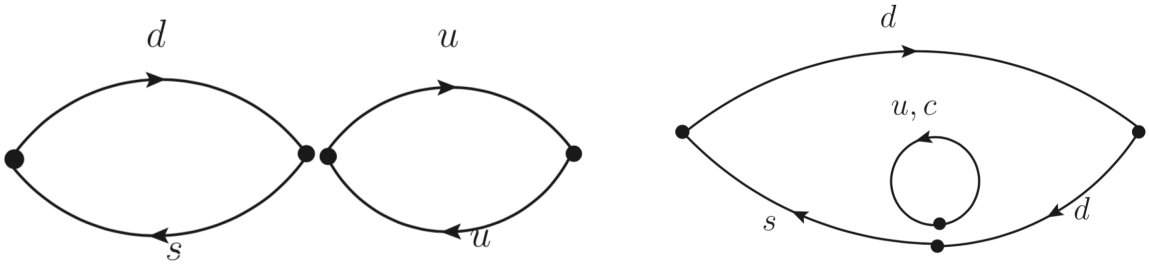

Figure 3.6: Examples of figure-8 diagram(left) and eye diagram(right) that appears in the three-point contractions.

The GIM mechanism enters three-point contractions only through the diagrams with self-loop propagators, like the eye diagrams. We can understand this from the fact that the initial and final states in our three-point calculation have no charm flavor and there is only one weak Hamiltonian operator inserted. Only the combination $\lambda_u C_i(Q_i^{uu} - Q_i^{cc})$ in the effective weak Hamiltonian operator shown in Equation 3.20, can be contracted to produce a self-loop propagator and will yield a self-loop propagator with an up quark subtracted by a self-loop propagator with a charm quark. We denote such a flavor structure as $(uu - cc)$. For example, the eye diagram shown in Figure 3.6 can be explicitly calculated as:

$$\text{(eye)}_{GIM} = \sum_x Tr\Big[\Gamma^\mu S_d^W(x,t_f)\gamma_5 S_d^W(t_f,t_i)\gamma_5[S_s^W(x,t_i)]^{-1}\Big] Tr\Big[\Gamma_\mu S^P_{(uu-cc)}(x,x)\Big], \tag{3.27}$$

where $\Gamma^\mu = \gamma^\mu(1-\gamma_5)$, the space-time site x are all on a time slice t and $Tr[...]$ indicates a trace over spin and color indices.

Two-point contractions

The contractions appearing in the two-point correlation functions are shown in the Appendix D. For example, the kaon two-point contraction is given by:

$$C_K^{\text{2pt}}(t_f, t_i) = Tr\Big[S_d^{WW}(t_f, t_i)\gamma_5[S_s^{WW}(t_f, t_i)]^{-1}\Big]. \tag{3.28}$$

The source and sink of the two-point correlation function are both wall operators. Please note the contraction where the wall source and wall sink are on the same time slice are different from the self-loop propagators appearing in the three-point correlation functions which are generated by the weak operator with a point source.

3.3 Evaluation of correlation functions on the lattice

Under the path integral formalism of quantum field theory, the expectation value of an observable O, like a correlation function required in our calculation, can be expressed in terms of path integral as:

$$\langle O\rangle = \frac{\int \mathcal{D}\Phi O e^{-iS}}{\int \mathcal{D}\Phi e^{-iS}}. \tag{3.29}$$

On a lattice with Euclidean space and time, the expectation value is given by:

$$\langle O\rangle = \frac{\int \mathcal{D}\Phi O e^{-S}}{\int \mathcal{D}\Phi e^{-S}}, \tag{3.30}$$

where $Z = \int \mathcal{D}\Phi e^{-S(\Phi)}$ is the partition function if interpreted from a statistical mechanics perspective. Therefore, we obtain the expectation values of the observables by performing averages over ensembles which follow the distribution properties encoded in the partition function.

By using the Hybrid Monte Carlo(HMC) method, ensembles of gauge configurations satisfying the distribution determined by the lattice action S are generated. The correlation functions required in our calculation are evaluated on these lattice configurations statistically. Specifically, we obtain the expectation values of the diagrams by calculating each diagram on each configura-

tion and then performing an ensemble average. As basic elements of the diagrams, all the required propagators have to be calculated numerically on each configuration. In this section, we will show the lattice action used to generate lattice configurations and the propagators necessary for our Δm_K calculation.

3.3.1 Chiral symmetry and lattice actions

Chiral symmetry of the standard model in the massless quark limit, and the spontaneous breaking of symmetry, lead to the spectrum of light mesons like pion, kaon etc. The interactions at low energy between these hadronic states are restricted by the conditions imposed by chiral symmetry. Therefore, for lattice calculations related to light mesons, reproducing the chiral symmetry and also anomalies in a lattice calculation is crucial.

On the other hand, in our non-perturbative renormalization(NPR) calculation, chiral symmetry prevent operators with different chiralities from mixing and we can limit the dimension of the operator basis needed for NPR.

Based these two arguments, we expect a lattice calculation with a sufficient level of chiral symmetry in the continuum limit not only to preserve the physical spectrum at the low energy scale but also at higher energy scales to reduce the complexity of our NPR calculations.

There are several fermion actions that achieve either approximate or exact chiral symmetry consistent with the restrictions on the Dirac operator D as described by the Nielson-Ninomiya theorem. The clover-improved Wilson fermion action has terms which break chiral symmetry. Although the overlap fermion action on the lattice has exact chiral symmetry, calculations using it are computationally expensive. Compared to these two types of fermion actions, our choice of fermion action, the domain wall fermion action, has well-controlled, approximate chiral symmetry.

The domain wall fermion formalism is based on the fact that, in a continuum 5-dimensional field theory, if we include a varying mass $m(s)$ as a function of the fifth dimension s in the 5-dimensional Dirac operator:

$$D_5 = \not{\partial}_4 + \gamma_5 \partial_s - m, s \geq 0, \tag{3.31}$$

where the mass $m(s)$ is given by:

$$m(s) = m\epsilon(s) = \begin{cases} +m & s > 0 \\ \\ -m & s < 0 \end{cases}, \qquad m > 0, \tag{3.32}$$

one finds boundary states localized at $s = 0$ in the fifth dimension are four-dimensional fermions with definite chirality, given the infinite dimension in the s direction. On the lattice, with a compact fifth dimension and periodic boundary conditions where $\psi(x_\mu, s+2L_s) = \psi(x_\mu, s)$ and mass $m(s) = m\frac{s}{|s|}$, the right-handed and left-handed chiral fermions on the boundaries couple to each other and their coupling is proportional to the residual mass for the massive fermions even without extra interactions:

$$m_{\text{res}} \sim 2me^{-2mL_s}. \tag{3.33}$$

Here m_{res} is a measure of the chiral symmetry violation and any matrix element of an operator with chiral symmetry violation should be of a similar size or smaller. We have to balance the level of chiral symmetry we would like to obtain and the computational cost during the inversion, which is proportional to the size of the fifth dimension L_s.

To implement it on the lattice, Shamir's domain wall fermion action is used and it is given by:

$$\sum_{b=1}^{5}\sum_{x}\sum_{s=1}^{L_s}[\frac{1}{2}\overline{\psi}\gamma_b(\partial_b^* + \partial_b)\psi - m\overline{\psi}\psi - \frac{r}{2}\overline{\psi}\partial_b^*\partial_b\psi], \tag{3.34}$$

where the lattice sites on the five-dimentional lattice is $\mathbf{n} = \{x, s\}$. x is the four-dimensional space-time coordinate and s is the coordinate in the fifth dimention.

To further reduce the computational cost, we use Mobius domain wall fermions where L_s is reduced while the approximate chiral symmetry is still preserved. Results for several quantities indicating that the chiral properties of 64^3 lattice with physical quark masses should be appropriate to be used for the Δm_K calculation [12].

For the gauge action, we used an improved gauge action, the Iwasaki gauge action, which can

be written explicitly as:

$$S_G(U) = \beta \sum_{x,\mu<\nu} (1 - \frac{c_0}{3}) ReTrU_P(x,\mu,\nu) + \beta \sum_{x,\mu\neq\nu} (1 - \frac{c_1}{3}) ReTrU_R(x,\mu,\nu), \tag{3.35}$$

where the first term is derived from the Wilson action and the second term is the additional 1×2 plaquette term with:

$$U_R(x,\mu,\nu) = U_\mu(n) U_\mu(n+\hat{\mu}) U_\nu(n+2\hat{\mu}) U_\mu^\dagger(n+\hat{\mu}+\hat{\nu}) U_\mu^\dagger(n+\hat{\nu}) U_\nu^\dagger(n). \tag{3.36}$$

The coefficients c_0 and c_1 are given by:

$$c_1 = -0.331, c_0 = 1 - 8c_1. \tag{3.37}$$

In Table 3.1, we list the key parameters of several lattices which we use in our calculation of Δm_K and estimation of systematic errors.

Lattice name	Action (F+G)	a^{-1} (GeV)	Lattice Volume	β	b+c	L_s	m_l	m_h	m_{res}
24I	DWF+I	1.785(5)	$24^3 \times 64 \times 16$	2.13	1.0	16	0.0050	0.0400	0.00308
32I	DWF+I	2.383(9)	$32^3 \times 64 \times 16$	2.25	1.0	16	0.0040	0.0300	0.000664
64I	MDWF+I	2.359(7)	$64^3 \times 128 \times 12$	2.25	2.0	12	0.000678	0.02661	0.000314
32IF	DWF+I	3.15(2)	$32^3 \times 64 \times 12$	2.37	1.0	12	0.0047	0.0186	0.000631

Table 3.1: Dynamical 2+1 flavor domain wall fermion lattices used in our Δm_K calculation [12]. The fermion and gauge (F+G) action abbreviations are: DWF = domain wall fermions, MDWF = Mobius domain wall fermions, I = Iwasaki gauge action. $m_{l/h}$ are the sea quark masses in lattice units.

3.3.2 Propagators

Propagators on the lattice can generally be written as:

$$S = D^{-1}, \tag{3.38}$$

where D is the lattice Dirac operator. If suppressing the spin and color indices, the S and D have the dimension $N \times N$ where N is the total number of lattice sites in five dimensions. If S is viewed as an $N \times N$ matrix then each matrix element itself is a 12×12 Wilson matrix.

A propagator with source on site x and sink on site y is just $S(x, y) = D^{-1}(x, y)$. Given the large size of N, inverting the whole matrix D is very computationally expensive. Based on the diagrams we need to evaluate, we don't need propagators from all the lattice site sources, therefore inverting the matrix D is unnecessary.

Instead, we write down a propagator $S^X(x)$ with sink on site x and with a source of type X represented by a vector $\eta^X(y)$, as a linear combination of point source propagators as below:

$$S^X(x) = \sum_y S(x, y)\eta^X(y). \tag{3.39}$$

If written in a matrix form, this becomes:

$$S^X(x) = (S\eta)(x) = (D^{-1}\eta^X)(x) \tag{3.40}$$

or

$$D(a, x)S^X(x) = D(a, x)(D^{-1}\eta^X)(x) = \eta^X(a) \tag{3.41}$$

or

$$DS^X = \eta^X. \tag{3.42}$$

Therefore we can obtain the propagator $S^X(x)$ for all the x on the lattice by solving the linear equation shown in Equation 3.42. Here the S^X is no longer a matrix but a vector with each element being a Wilson matrix, propagating from the certain source X to a sink site on the lattice. Note, each source η^X is actually a set of 12 sources with 12 spins and colors. The 12 sources provide the column index for the 12×12 Wilson matrix identified in the previous sentence. Therefore, in the following discussion, we use an upper index to label the type of the source, and a lower index to label the key parameter of the source and a variable x in the bracket, to represent the element with

index x in the vector of propagators.

Given the large size of the lattice, we decompose the original lattice into parts and distribute the inversion tasks among the massive cores on supercomputers.

Wall-source-point-sink propagators

The source η^W for a wall-source propagator with source on time slice t_{src} with spin α and color a is:

$$[\eta^W_{t_{src},a\alpha}(t,\vec{x})]_{b\beta} = \begin{cases} V_{ab}\delta_{\alpha\beta}, & t = t_{src} \\ 0, & t \neq t_{src}, \end{cases} \tag{3.43}$$

where V is the gauge fixing matrix with color indices written in Latin letters a and b and spin indices are labeled by Greek letters α and β. And we solve the linear equation:

$$DS^W_{t_{src}} = \eta^W_{t_{src}} \tag{3.44}$$

to obtain the propagators $S^W_{t_{src}}$.

Wall-source-wall-sink propagators

To build a two-point correlation function of a meson, we need wall-source-wall-sink propagators. The wall-source-wall-sink propagators are created by summing all the wall propagators with the source at t_{src} and the sink on the specified sink time slice t_{snk}:

$$S^{WW}(t_{src},t_{snk}) = \sum_{\vec{y}} V(t_{snk},\vec{y}) S^W_{t_{src}}(t_{snk},\vec{y}). \tag{3.45}$$

Point-source-point-sink propagators

The source distribution η^P for a point-source propagator with source on site x_{src} with spin α and color a is:

$$[\eta^P_{x_{src},a\alpha}(x)]_{b\beta} = V_{ab}\delta_{\alpha\beta}\delta_{x x_{src}}, \tag{3.46}$$

where $a\alpha$ labels a 12-component vector with spin index α and color index a. And we solve the linear equation:

$$DS^P_{x_{src}} = \eta^P_{x_{src}} \tag{3.47}$$

and a propagator with the sink on site x_{snk} is just $S^P_{x_{src}}(x_{snk})$.

Random-source and All-to-All(A2A) propagators

Self-loop propagators $S^P_x(x)$ which have both source and sink on the same lattice site have to be calculated.

To increase the statistics for these self-loop propagators, on each time slice, we would like to average self-loop propagators multiplied by the rest of the diagram from all spacial sites. One natural way is to calculate the point-source propagators as in Equation 3.47.

This is very computationally expensive due to the large number of lattice sites. Instead of calculating $S^P_x(x)$ for all x, we use random-source propagators under the formalism of A2A propagators.

The basic idea of the A2A propagator is that a propagator with a specific source can be statistically approximated using a A2A propagators with random sources. Here we illustrate how this method is applied to our self-loop propagator calculations.

Firstly we introduce a random point source η_i where i the index of random hits, which satisfies:

$$\langle \eta(t_x, \vec{x}) \eta(t_y, \vec{y})^\dagger \rangle = \lim_{N\to\infty} \frac{1}{N} \sum_{i=1}^{N} \eta_i^\dagger(t_x, \vec{x}) \eta_i(t_y, \vec{y}) = \delta(t_x - t_y)\delta^3(\vec{x} - \vec{y}). \tag{3.48}$$

In our calculation of self-loop propagators, we used Z_2 random numbers where the random number on the sites can either be 1 or -1 and one can easily check that Equation 3.48 is satisfied.

Secondly, if we obtain a vector of all propagators S^R_i with random source η_i with hit index i satisfying:

$$DS^R_i = \eta_i, \tag{3.49}$$

where $\eta_i(y) = \eta_i(t_y, \vec{y})$, we can express it as:

$$S_i^R = D^{-1}\eta_i. \tag{3.50}$$

We can obtain $S_x^R(x)$ where the source and sink are both at a lattice site x by averaging the product of random propagators $S_i^R(x)$ and the random source $\eta_i(x)$:

$$S_x^R(x) \approx \frac{1}{N}\sum_{i=1}^{N} S_i^R(x)\eta_i^\dagger(x) = \sum_z D^{-1}(x,z)\langle\eta_i(z)\eta_i^\dagger(x)\rangle = D^{-1}(x,z)\delta_{z,x} = D^{-1}(x,x) \tag{3.51}$$

where $\langle ...\rangle$ indicates an average over N hits. The approximation in Equation 3.51 becomes exact in the limit of large statistics, and we can pick out $S_x^R(x)$ for all possible values of x and then sum over x to obtain the complete contribution of all self-loop propagators.

Low-mode deflation and Lanczos eigenvectors

Calculation of the above propagators is equivalent to solving linear equations of the form in Equation 3.42. A common method to obtain such solutions is the Conjugate Gradient(CG) method and we use it to calculate the required propagators in our Δm_K calculation.

One of the requirement of CG method is the matrix A in linear equation:

$$Ax = b, \tag{3.52}$$

should be Hermitian. In our case ,the Dirac matrix itself is not Hermitian so we multiply both sides of the Equation 3.42 with $D^\dagger$ and obtain:

$$(D^\dagger D)S^X = MS^X = \eta'^X = D^\dagger\eta^X. \tag{3.53}$$

Now the matrix $M \equiv D^\dagger D$ satisfies the Hermitian condition $M = M^\dagger$ while the solution S^X remains the same.

Another observation of our calculation is that for different propagators with different sources, while the right-hand side of the linear equation is specific to each source type, the left-hand side, especially the matrix $M \equiv D^\dagger D$ is generic. An improvement using low-mode deflation can be used to accelerate the calculation and the low-mode eigenvectors can be reused to accelerate the CG solving process for various sources.

The number of CG iterations in solving Equation 3.53 is proportional to the condition number, which is the ratio between the largest and the smallest eigenvalue of the matrix M given by:

$$\kappa = \frac{\lambda_{max}}{\lambda_{min}}. \tag{3.54}$$

Low-mode deflation aims to remove the low-mode component of M, denoted as M_l, so that κ_h, the condition number of the remaining high-mode matrix M_h is reduced and the number of CG iterations is reduced. In our calculation, only light quark propagators are solved with low-mode deflation. Given the much larger charm quark mass, the condition number for solving charm propagators is already small enough and performing the low-mode deflation is not very efficient.

Using a projector formed by n eigenvectors $|\lambda_i\rangle$ of the matrix M with lowest eigenvalues λ_i:

$$\mathcal{P} = \sum_{i=1}^{n} |\lambda_i\rangle\langle\lambda_i|, \tag{3.55}$$

we can decompose Equation 3.53 into two parts:

$$M_l S_l^X = \eta'_l, \quad S_l^X = \mathcal{P} S^X, \eta'^X_l = \mathcal{P}\eta'^X \tag{3.56}$$

where $M_l = \mathcal{P}M\mathcal{P}$, and

$$M_h S_h^X = \eta'_h, \quad S_h^X = (1-\mathcal{P})S^X, \eta'^X_h = (1-\mathcal{P})\eta'^X \tag{3.57}$$

where $M_h = (1-\mathcal{P})M(1-\mathcal{P})$.

If we express the vector of projected propagator S_l^X as a linear combination of low-mode eigenvectors $|\lambda_i\rangle$ with coefficients $S_{l,i}^X$:

$$S_l^X = \sum_{i=1}^{n} S_{l,i}^X |\lambda_i\rangle \tag{3.58}$$

and plug it into Equation 3.56, we obtain S_l^X explicitly:

$$S_l^X = \sum_{i=1}^{n} S_{l,i}^X |\lambda_i\rangle = \sum_{i=1}^{n} \frac{\langle \lambda_i | \eta_l^{'} \rangle}{\lambda_i} |\lambda_i\rangle. \tag{3.59}$$

The remaining matrix related to the high modes, can be solved using the CG method. Because the low-mode part has been removed, the smallest eigenvalue of the remaining matrix M_h is increased. Therefore, the number of CG iterations in solving M_h can be significantly reduced.

Low-mode deflation is also applicable to our calculation of self-loop propagators using random source A2A propagators. The random source are only introduced when solving the high mode parts and the corresponding self-loop propagators $S_x^R(x)$ is given by:

$$S_x^R(x) = S_{x,l}^R(x) + \langle S_{x,h}^R(x) \rangle = \sum_{i=1}^{n} \frac{\langle \lambda_i | x \rangle}{\lambda_i} |\lambda_i\rangle(x) + \sum_{i=1}^{N_h} S_{i,h}^R(x) \eta_i^{\dagger}(x) \tag{3.60}$$

where $|\lambda_i\rangle(x)$ is the xth element of eigenvector $|\lambda_i\rangle$ and $\langle S_{x,h}^R(x) \rangle$ is the statistically averaged A2A self-loop propagator over N_h hits calculated for the high modes.

Deflation requires a certain number of eigenvectors of the matrix M with the lowest eigenvalues. The implicit restarted Lanczos(IRL) algorithm is used to generate 2000 eigenvectors for our calculation on the $64^3 \times 128$ lattice.

3.3.3 Sample all-mode averaging(AMA) method

The stopping condition for solving $Ax = b$ numerically with CG method is defined as:

$$r_{k+1} < \epsilon, \tag{3.61}$$

where ϵ is the tolerance of the CG solver and r_{k+1} is the residual of the $(k+1)$th iteration calculated in an iterative way:

$$r_{k+1} = r_k - \alpha_k A p_k, \tag{3.62}$$

where $\alpha_k = \frac{|r_k|^2}{\langle p_k|A|p_k\rangle}$ and $p_{k+1} = r_{k+1} + \frac{|r_{k+1}^2|}{|r_k^2|} p_k$. The smaller the ϵ, the more CG iterations are needed.

We use the sample AMA method to reduce the computational cost. AMA method aims to calculate physical quantities with unbiased improved estimators which have significantly reduced statistical errors at modest computational cost[13].

The standard AMA correction is applied on each configuration, among different time slices: on most time slices, quantities are calculated with a CG tolerance ϵ_{slp}("sloppy") and on the other time slices, quantities are calculated with a smaller CG tolerance ϵ_{ext}("exact") in addition to the case with CG tolerance ϵ_{slp} and make the difference between the results from the two cases as corrections. In contrast, the sample AMA correction is applied among configurations: on most configurations, quantities are calculated with a CG tolerance ϵ_{slp} of 10^{-4}. On the other configurations the same quantities are calculated with two CG tolerances $\epsilon_{slp} = 10^{-4}$and $\epsilon_{ext} = 10^{-8}$. The differences between "sloppy" and "exact" calculations are used as corrections to the "sloppy"-only configurations.

In our case, we have data for type-3 and type-4 diagrams, three-point and two-point functions from both "sloppy" calculations and corrections.

3.4 Non-perturbative renormalization

In the process of obtaining the effective weak Hamiltonian, we need to include the ultraviolet behavior of the full theory obtained by integrating out the heavy particles. The resulting Wilson coefficient functions and the matrix elements of operators Q_i have a μ-dependence, where μ is the renormalization scale where the operators are defined.

The typical way to calculate the renormalized Wilson coefficients is based on dimensional

regularization and specifying a specific renormalization scheme like $\overline{MS}$. However, for a lattice operator, we can not simply perform dimensional regularization with a lattice of dimension $4 + 2\epsilon$. Instead, the lattice operators $Q_i^{lat}(a)$ regulated by the inverse lattice spacing, a^{-1}, can be renormalized using lattice perturbation theory if both a^{-1} and renormalization scale μ are large enough. However, this is usually complicated and has challenges for convergence.

Alternatively, we use non-perturbative renormalization for the lattice operators and obtain the Wilson coefficients C_i^{lat} from those in the $\overline{MS}$ scheme in three steps [14] [9]:

- Non-perturbative renormalization: Renormalize the lattice in a regularization-independent(RI) scheme.
- Perturbation theory: Convert from the RI to the $\overline{MS}$ renormalization scheme.
- Perturbation theory: Calculate the Wilson coefficients in the $\overline{MS}$ scheme.

Generally, mixing between the operators happens during the renormalization and the relation between the operators defined in the $\overline{MS}$ scheme and the lattice operators given by these three steps can be expressed as:

$$C_i^{\overline{MS}} Q_i^{\overline{MS}} = C_a^{\overline{MS}} (1 + \Delta r)_{ab}^{RI \to \overline{MS}} Z_{bi}^{lat \to RI} Q_i^{lat} = C_i^{lat} Q_i^{lat}. \tag{3.63}$$

So the Wilson coefficients for the lattice operators C_i^{lat} can be expressed as:

$$C_i^{lat} = C_a^{\overline{MS}} (1 + \Delta r)_{ab}^{RI \to \overline{MS}} Z_{bi}^{lat \to RI} \tag{3.64}$$

3.4.1 Four-quark operators and irreducible representations of $SU(4) \times SU(4)$

Before we perform NPR on lattice, we have to confirm how many operators are involved and include all the operators which can mix with the current-current operators in our calculation of Δm_K.

The operators are products of quark operators with different flavors and transform under global

$SU(4) \times SU(4)$ rotations, where $N_f = 4$ is the number of flavors. The NPR calculation is designed to remove the short-distance ultraviolet singularities of the operators. Thus we can perform the NPR calculation in the limit where the u, d, s and c quark masses are set to be degenerate. In addition, because chiral symmetry is approximately preserved by the domain wall fermion action, operators belonging to different irreducible representations of the $SU(4)$ group will not mix with each other during the renormalization group evolution and operators which are members of the same irreducible representation that is which transform into each other under the $SU(4) \times SU(4)$ symmetry will have the same renormalization factor. Therefore, identifying the irreducible representations to which the operators belong will minimize the number of lattice operators needed for the NPR calculations.

One usually starts from the general problem where the four-quark operator is transforming as a fourth-rank tensor and use the tensor method to find the operator combinations belonging to irreducible representations. Our calculation involves only a left-left spin structure so we will focus on left-left operators. The four-quark left-left operators can be written as :

$$Q_{LL} = (T_{LL})^{ij}_{kl}(\overline{q}_{L,i} \otimes q_{L,k})(\overline{q}_{L,j} \otimes q_{L,l}), \tag{3.65}$$

where we identify q^1_L with an up quark, q^2_L with a down quark, q^3_L with a strange quark and q^4_L with a charm quark. The quark fields transform in the fundamental representation of $SU(4)_L$. If we denote the representation under left-handed and right-handed chiral transformation as (L,R), then $\overline{q}_{L,i}$, $\overline{q}_{L,j}$ transform as $(\overline{4}, 1)$ and $q_{L,k}$, $q_{L,l}$ transform as $(4, 1)$. The transformation of Q_{LL} indicates that it is a member of a 256-dimensional representation $(\overline{4}\otimes 4)\otimes(\overline{4}\otimes 4)$ of $SU(4)_L$ which is reducible. We can use the permutation symmetry of the tensor indices of the coefficient matrix $(T_{LL})^{ij}_{kl}$ to decompose the tensor:

$$(T_{LL})^{ij}_{kl} = (T_{LL})^{\{i,j\}}_{\{k,l\}} + (T_{LL})^{\{i,j\}}_{[k,l]} + (T_{LL})^{[i,j]}_{\{k,l\}} + (T_{LL})^{[i,j]}_{[k,l]}, \tag{3.66}$$

where $\{i, j\}$ denotes indices that are symmetric and $[i, j]$ indices that are anti-symmetric under

permutation. We can identify the correspondingly sub-spaces which are invariant under $SU(4)_L$ transformation with each of the four types of tensors. We can further find the irreducible representations of $SU(4)_L$ by considering the trace of a pair of upper and lower indices [15]. In addition, because the operators in our calculation are symmetric under simultaneous exchange of indices $(i,k) \leftrightarrow (j,l)$, only the completely symmetric case $(T_{LL})^{\{i,j\}}_{\{k,l\}}$ and the completely anti-symmetric case $(T_{LL})^{[i,j]}_{[k,l]}$ are relevant. The dimension of the two sets of irreducible representations are obtained based on the trace properties and are shown in Table 3.2.

Symmetry of T_{LL}	$(T_{LL})^{\{i,j\}}_{\{k,l\}}$	$(T_{LL})^{[i,j]}_{[k,l]}$
Dimension	$10 \times 10^* = 100$	$6 \times 6^* = 36$
Irrep. dimension	84,15,1	20,15,1

Table 3.2: The dimension of the irreducible representations of $SU(4)_L$ relevant to our calculation.

Then we can examine the operators relevant to our calculation and identify which of the irreducible representations these operators enter. Based on Equation 3.20, the operators are:

$$\widetilde{Q}_1 = Q_1^{uu} - Q_1^{cc} = (\bar{s}_i d_i)_L (\bar{u}_j u_j)_L - (\bar{s}_i d_i)_L (\bar{c}_j c_j)_L, \tag{3.67}$$

$$\widetilde{Q}_2 = Q_2^{uu} - Q_2^{cc} = (\bar{s}_i d_j)_L (\bar{u}_j u_i)_L - (\bar{s}_i d_j)_L (\bar{c}_j c_i)_L, \tag{3.68}$$

$$Q_1^{uc} = (\bar{s}_i d_i)_L (\bar{u}_j c_j)_L, \tag{3.69}$$

$$Q_2^{uc} = (\bar{s}_i d_j)_L (\bar{u}_j c_i)_L, \tag{3.70}$$

$$Q_1^{cu} = (\bar{s}_i d_i)_L (\bar{c}_j u_j)_L, \tag{3.71}$$

$$Q_2^{cu} = (\bar{s}_i d_j)_L (\bar{c}_j u_i)_L. \tag{3.72}$$

For each case, we apply the Fierz identity and rewrite the operators in the color unmixed form:

$$\widetilde{Q}_1 = Q_1^{uu} - Q_1^{cc} = (\bar{s}d)_L (\bar{u}u)_L - (\bar{s}d)_L (\bar{c}c)_L, \tag{3.73}$$

$$\widetilde{Q}_2 = Q_2^{uu} - Q_2^{cc} = (\bar{s}u)_L (\bar{u}d)_L - (\bar{s}c)_L (\bar{c}d)_L, \tag{3.74}$$

$$Q_1^{uc} = (\bar{s}d)_L(\bar{u}c)_L, \tag{3.75}$$

$$Q_2^{uc} = (\bar{s}c)_L(\bar{u}d)_L, \tag{3.76}$$

$$Q_1^{cu} = (\bar{s}d)_L(\bar{c}u)_L, \tag{3.77}$$

$$Q_2^{cu} = (\bar{s}u)_L(\bar{c}d)_L, \tag{3.78}$$

where there is no coloring mixing and the color indices are suppressed.

We define a new set of operators which contains linear combinations of the above operators:

$$Q_+^X = Q_1^X + Q_2^X, \tag{3.79}$$

$$Q_-^X = Q_1^X - Q_2^X, \tag{3.80}$$

where the label X denotes the possible flavor structures which can be "$\sim$", "uc" and "cu". Using $X = \sim$ as an example:

$$\widetilde{Q}_+ = (\bar{s}d)_L(\bar{u}u)_L - (\bar{s}d)_L(\bar{c}c)_L + (\bar{s}u)_L(\bar{u}d)_L - (\bar{s}c)_L(\bar{c}d)_L, \tag{3.81}$$

$$\widetilde{Q}_- = (\bar{s}d)_L(\bar{u}u)_L - (\bar{s}d)_L(\bar{c}c)_L - (\bar{s}u)_L(\bar{u}d)_L + (\bar{s}c)_L(\bar{c}d)_L, \tag{3.82}$$

we can find that Q_+^X corresponds to a tensor of coefficients $(T_{LL})^{ij}_{kl}$ which is traceless and symmetric under permutations and therefore belongs to the (84,1) irreducible representation while for Q_-^X, T_{LL} is traceless and anti-symmetric under permutations and therefore belongs to the (20,1) irreducible representation. We can also directly use the renormalization factors calculated from any operator belonging to (84,1) or (20,1) representations for our $Q_\pm^X$ operators. Thus, we only need to perform NPR for Q_+^X and Q_-^X for a single choice of X, since the renormalization factors for the other X choices are identical. However, since the $Q_\pm^X$ are linear combinations of the Q_i^X operators, and the Q_i^X enter both (84,1) and (20,1) representations, we can also perform the NPR using the basis of Q_i^X with a 2×2 operator renormalization mixing matrix and the relationship of the renormalization

factors between the two basis is given by:

$$Z_{\pm} = Z_{11} \pm Z_{12}, \tag{3.83}$$

where the Z_{ij} with $i, j = 1, 2$ are the 2×2 mixing matrix elements entering:

$$ZQ^X = \begin{pmatrix} Z_{11} & Z_{12} \\ Z_{12} & Z_{22} \end{pmatrix} \begin{pmatrix} Q_1^X \\ Q_2^X \end{pmatrix} \tag{3.84}$$

with the diagonalized form being:

$$ZQ_{\pm}^X = Z_{\pm} Q_{\pm}^X. \tag{3.85}$$

The $Z_{\pm}$ factors can be obtained either by using RBC-UKQCD's standard NPR package which includes the calculation of renormalization factors for operators belong to (84,1) and (20,1) representations or performing a NPR calculation with only two Q_i^X operators involved. We can compare the results to confirm that our NPR results are consistent. Details of these comparisons can be found in Chapter 5.

Below we will describe how we perform the NPR calculation using only two Q_i^X operators in three steps. We choose X to be "cu" for simplicity since the renormalization factors for other X values are identical.

3.4.2 Non-perturbative renormalization: the RI-SMOM renormalization scheme

To begin with, we specify the regularization independent(RI) scheme where the connection to the $\overline{MS}$ scheme is achieved and where the NPR is performed. We choose the Rome-Southampton scheme as the RI scheme and we need to renormalize the results on the lattice using the same scheme. The corresponding renormalization factors are denoted as $Z^{lat \to RI}$. The RI scheme we choose to renormalize lattice operators is further specified to be the RI-SMOM(γ_μ, γ_μ) scheme where "S" denotes that the input momenta are non-exceptional and symmetrical. The first γ_μ denotes the fact that the projectors used for the operator mixing matrix M are constructed from γ

matrices and the second γ_μ denotes the scheme in which the quark wave function renormalization factor Z_q is calculated.

The renormalization condition is imposed as:

$$\frac{Z^{lat\to RI}}{Z_q^2} M = F, \tag{3.86}$$

where the operator mixing matrix M is calculated from the off-shell amputated four-quark Green's functions Γ_i and projectors $\mathcal{P}_j$. The matrix F is the operator mixing matrix calculated at tree level with the same operators and projectors. The factor Z_q^2 is introduced to renormalize the four external quark fields.

The off-shell four-quark Green's functions G_i with $i = 1, 2$ are defined as:

$$G_i(p_1, p_2) = \frac{1}{V} \sum_x \langle Q_i^{cu}(x) s(p_1) \overline{u}(p_2) c(p_1) \overline{d}(p_2) \rangle. \tag{3.87}$$

If written explicitly using Equation 3.69 and 3.70, the G_i are given by:

$$\begin{aligned} G_1(p_1, p_2)^{abcd}_{\alpha\beta\gamma\delta} = \frac{1}{V} \sum_{x,\mu} e^{-2i(p_2-p_1)x} &\left\{ (\gamma_5 S_s^\dagger(x, p_1)\gamma_5)^{aa'} \gamma^\mu (1-\gamma_5) S_d(x, p_2)^{a'b} \right\}^{\alpha\beta} \\ &\left\{ \gamma_5 S_c^\dagger(x, p_1)\gamma_5)^{cc'} \gamma^\mu (1-\gamma_5) S_u(x, p_2)^{c'd} \right\}^{\gamma\delta}, \end{aligned} \tag{3.88}$$

$$\begin{aligned} G_2(p_1, p_2)^{abcd}_{\alpha\beta\gamma\delta} = \frac{1}{V} \sum_{x,\mu} e^{-2i(p_2-p_1)x} &\left\{ (\gamma_5 S_s^\dagger(x, p_1)\gamma_5)^{aa'} \gamma^\mu (1-\gamma_5) S_d(x, p_2)^{c'b} \right\}^{\alpha\beta} \\ &\left\{ \gamma_5 S_c^\dagger(x, p_1)\gamma_5)^{cc'} \gamma^\mu (1-\gamma_5) S_u(x, p_2)^{a'd} \right\}^{\gamma\delta}, \end{aligned} \tag{3.89}$$

where $S_q(x, p)$ is a propagator with quark flavor q, a momentum source with momentum p, and a sink position x. Here γ_5-hermiticity, i.e. $\gamma_5 S^\dagger(x, y)\gamma_5 = S(y, x)$, is used and we label spin indices with Greek letters $\alpha, \beta, \gamma, \delta$ and color indices with Latin letters a, b, c, d.

The SMOM scheme requires that:

$$p_1^2 = p_2^2 = (p_1 - p_2)^2 \equiv \mu, \tag{3.90}$$

where we also define our renormalization scale μ. This choice of a non-exceptional momentum scheme suppresses the long-distance contributions due to the gluon exchange between the external legs. The momenta in lattice units, which we choose for our NPR calculation performed on the $32^3 \times 64$ lattice ensemble are:

$$p_1^{lat} = [4, 4, 0, 0], \tag{3.91}$$

$$p_2^{lat} = [0, 4, 4, 0], \tag{3.92}$$

where one can easily check that Equation 3.90 is satisfied. The energy scale μ can be calculated by:

$$\mu = |p_1| = \sqrt{\sum_{i=1}^{4} (\frac{2\pi p_{1,i}^{lat}}{L_i a})^2}, \tag{3.93}$$

where L_i denotes lattice size in the ith dimension and we have $a^{-1} = 2.38$ GeV.

We contract the operators and evaluate the five-point diagrams as shown in Figure 3.7. The momenta of the quark lines are introduced by using fixed momentum sources and the calculations and gauge field averaging are performed on Landau gauge fixed ensembles.

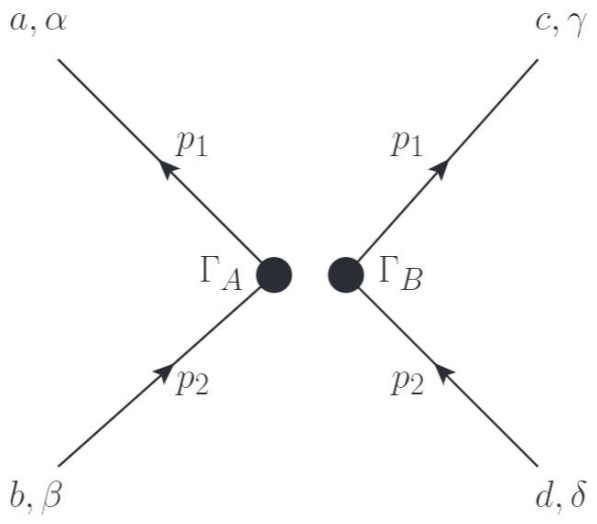

Figure 3.7: Five-point diagrams evaluated in NPR for Δm_K operators. Γ_A and Γ_B denote the spin structure of the vertex.

The amputated Green's functions are then obtained by multiplying $G_i$with the inverse of the

external quark propagators $S(p)$ with momentum p:

$$\Gamma_i(p_1,p_2)^{abcd}_{\alpha\beta\gamma\delta} = G_i(p_1,p_2)^{a'b'c'd'}_{\alpha'\beta'\gamma'\delta'}(\langle\gamma_5 S_s^\dagger(p_1)\gamma_5\rangle^{-1})^{a'a}_{\alpha'\alpha}(\langle S_u(p_2)\rangle^{-1})^{b'b}_{\beta'\beta}(\langle\gamma_5 S_c^\dagger(p_1)\gamma_5\rangle^{-1})^{c'c}_{\gamma'\gamma}(\langle S_d(p_2)\rangle^{-1})^{d'd}_{\delta'\delta}, \tag{3.94}$$

where the $\langle ...\rangle$ denotes the ensemble average. In our NPR calculation, the quark flavors are degenerate and the quark propagators are obtained by calculating the quark propagators with a momentum source:

$$S(p) = \sum_x S(x,p)e^{-ipx}. \tag{3.95}$$

We use two projectors with the same spin and color structures as the two operators Q_i^{cu}:

$$(\mathcal{P}_1)^{abcd}_{\alpha\beta\gamma\delta} = [(1-\gamma_5)\gamma^\mu]_{\alpha\beta}[(1-\gamma_5)\gamma_\mu]_{\gamma\delta}\delta^{ab}\delta^{cd}, \tag{3.96}$$

$$(\mathcal{P}_2)^{abcd}_{\alpha\beta\gamma\delta} = [(1-\gamma_5)\gamma^\mu]_{\alpha\beta}[(1-\gamma_5)\gamma_\mu]_{\gamma\delta}\delta^{ad}\delta^{cb}. \tag{3.97}$$

Combining the amputated Green's function with the projectors, we get the operator mixing matrix:

$$M_{ij} = \Gamma_i\mathcal{P}_j. \tag{3.98}$$

Here we have suppressed the spin and color indices where the same letters appearing in Equation 3.94, 3.96 and 3.97 are contracted. Because of the Fierz identity, one can easily check $M_{11} = M_{22}$ and $M_{12} = M_{21}$. Therefore, in the NPR evaluation, we need only to calculate Γ_1 and matrix elements M_{11} and M_{12}.

Accordingly, we can easily work out the tree-level mixing matrix:

$$F = \frac{1}{(12\times 4)^2}\begin{pmatrix} 1 & 1/3 \\ 1/3 & 1 \end{pmatrix}. \tag{3.99}$$

The quark field renormalization factor Z_q is calculated from Z_V and $\Lambda_{A/V}$ based on:

$$\frac{Z_q}{Z_V} = \frac{1}{2}(\Lambda_A + \Lambda_V) \tag{3.100}$$

where Z_V is the renormalization constant for the local vector correction. The three-point amplitudes Λ_A and Λ_V are to be evaluated using local currents and are given by:

$$\Lambda_V(p) = \frac{1}{48} Tr\Big(\sum_\mu \Gamma_V^\mu (\gamma_\mu \otimes I_3) \Big), \tag{3.101}$$

$$\Lambda_A(p) = \frac{1}{48} Tr\Big(\sum_\mu \Gamma_A^\mu (\gamma_\mu \gamma_5 \otimes I_3) \Big), \tag{3.102}$$

where the amputated Green's functions Γ_V^μ and Γ_A^μ shown in Figure 3.8 are given by:

$$\Gamma_V^\mu = (\langle \gamma_5 S^\dagger(p) \gamma_5 \rangle^{-1}) \Big\langle \frac{1}{V} \sum_x \gamma_5 S^\dagger(x,p) \gamma_5 \gamma_\mu S(x,p) \Big\rangle (\langle S(p) \rangle^{-1}), \tag{3.103}$$

$$\Gamma_A^\mu = (\langle \gamma_5 S^\dagger(p) \gamma_5 \rangle^{-1}) \Big\langle \frac{1}{V} \sum_x \gamma_5 S^\dagger(x,p) \gamma_5 \gamma_\mu \gamma_5 S(x,p) \Big\rangle (\langle S(p) \rangle^{-1}). \tag{3.104}$$

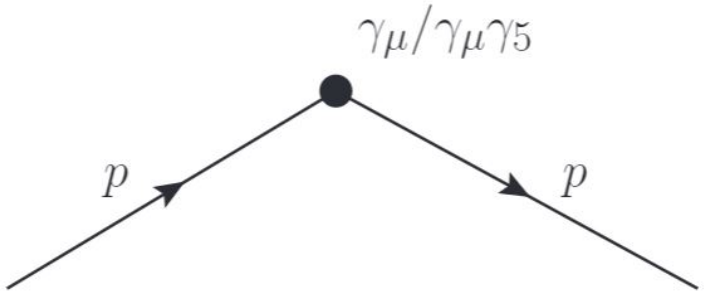

Figure 3.8: Three-point diagrams used to calculate $\Lambda_{A/V}$ in the γ scheme.

For our calculation of Δm_K on the $64^3 \times 128$ lattice ensemble, we performed the NPR calculation on a $32^3 \times 64$ lattice ensemble with lattice spacing almost the same as the 64^3 lattice. By using $Z_V = 0.7447$ from Reference [12] and calculating Λ_A and Λ_V, we obtain $Z_q = 0.7720$.

3.4.3 Perturbation theory: conversion from RI-SMOM to $\overline{MS}$ scheme

We have chosen the RI-SMOM(γ_μ, γ_μ) scheme for our NPR calculation and the connection matrix Δr to the $\overline{MS}$ scheme with four-flavor $SU(4) \times SU(4)$ chiral symmetry calculated perturbatively is given by:

$$\Delta r = \frac{\alpha_s(\mu)}{4\pi} \begin{pmatrix} \frac{-12\ln(2)}{N_c} + \frac{8}{N_c} & -8 + 12\ln(2) \\ -8 + 12\ln(2) & \frac{-12\ln(2)}{N_c} + \frac{8}{N_c} \end{pmatrix}, \tag{3.105}$$

and for $N_c = 3$, we obtain:

$$\Delta r = \frac{\alpha_s(\mu)}{4\pi} \begin{pmatrix} -4\ln(2) + \frac{8}{3} & -8 + 12\ln(2) \\ -8 + 12\ln(2) & -4\ln(2) + \frac{8}{3} \end{pmatrix}, \tag{3.106}$$

where $\alpha_s(\mu)$ is the coupling constant calculated from the two-loop perturbation calculation and its formula is given by Equation (III.19) in [9]. To calculate $\alpha_s(\mu)$, Λ_{QCD} in four-flavor theory, denoted as $\Lambda^{(4)}_{QCD}$ is required. $\Lambda^{(4)}_{QCD}$ is calculated from $\Lambda^{(5)}_{QCD}$, which is the Λ_{QCD} in five-flavor theory, by requiring that the value of coupling at bottom quark mass $\alpha_s(m_b)$ is the same from both four- and five-flavor calculations. The value of $\Lambda^{(5)}_{QCD}$ is specified by the known value of $\alpha_s(m_Z)$, the coupling at Z boson mass.

We choose to have the scale $\mu = 2.64$ GeV, which is calculated from the momentum scale we have on the $32^3 \times 64$ lattice ensemble. Using the parameters shown in Table 3.3, especially $\Lambda_{QCD} = 0.33$ GeV, we obtain $\alpha_s(\mu = 2.64\text{GeV}) = 0.27074$ and Δr values as shown in Table 3.4.

m_t	m_W	m_Z	$\alpha_s(m_Z)$	$m_b(m_b)$	$\Lambda^{(5)}_{QCD}$	$\Lambda^{(4)}_{QCD}$
172.2 GeV	80.4 GeV	91.1876 GeV	0.1184	4.19 GeV	231 MeV	330 MeV

Table 3.3: The values of input parameters for the calculation of Wilson coefficients.

3.4.4 Perturbation theory: calculation of the Wilson coefficients in the $\overline{MS}$ scheme.

The final step is to calculate the the Wilson coefficients in the $\overline{MS}$ scheme which evolve from the M_W scale to our scale $\mu = 2.64$ GeV according to the renormalization group theory, using

Equation (XII.44)-(XII.61) in [9]. The values of $C_i^{\overline{\rm MS}}$ which have been calculated in our earlier Δm_K calculation [16] can be found in Table 3.4 and we continue to use these values in our Δm_K calculation. The numbers from each steps and the Wilson coefficients C_i^{lat} for our lattice operators are also summarized in Table 3.4.

$C_1^{\overline{\rm MS}}$	$C_2^{\overline{\rm MS}}$	$\Delta r_{11} = \Delta r_{22}$	$\Delta r_{12} = \Delta r_{21}$	Z_V	Z_q	$Z_{11} = Z_{22}$	$Z_{12} = Z_{21}$	$C_1^{\rm lat}$	$C_2^{\rm lat}$
-0.260	1.118	-2.28×10^{-3}	6.85×10^{-3}	0.7447	0.7720	0.5642	-0.03934	-0.1859	0.6382

Table 3.4: The Wilson coefficients, the RI $\rightarrow \overline{\rm MS}$ matching matrix elements, the non-perturbative lat $\rightarrow$ RI operator renormalization matrix elements in (γ_μ, γ_μ) scheme and their final product C_i^{lat}, calculated at the scale $\mu = 2.64$ GeV.

Chapter 4: Data analysis of Δm_K calculation

In this chapter, we will discuss the data analysis method used in our Δm_K calculation. In Section 4.1, we will discuss how we process the data and obtain the quantities needed from fitting the data to theoretical formulas of two-point, three-point and four-point correlation functions. In Section 4.2, we will discuss data analysis for type-4 diagrams with multiple source-sink separations. Because these data analysis methods are generic to calculations on several lattices, we will only introduce the notations of the parameters and present the values we used in our calculation in Chapter 6. In Section 4.3 and Section 4.4, we will discuss the data format we use and the jackknife method introduced for the evaluation of statistical errors.

4.1 Fitting of correlation functions

4.1.1 Fitting two-point correlation functions

We obtain the normalization factors for meson operators and meson masses from fitting two-point correlation functions to the time dependence shown in Equation 3.16.

Taking the periodic boundary condition that we imposed on the $64^3 \times 128$ lattice in the time direction, the time dependence becomes:

$$C_M^{\mathrm{2pt}}(t) \approx N_M^2(e^{-m_M t} + e^{-m_M(\mathcal{T}-t)}) = 2N_M^2 e^{-\frac{m_M \mathcal{T}}{2}} \cosh(\frac{\mathcal{T}}{2} - t), \tag{4.1}$$

where M denotes the meson state, N_M is the normalization factor and $\mathcal{T}$ is the lattice size in time direction. We can see that for $t \ll (\mathcal{T} - t)$, we can neglect the second term and Equation 3.16 is reproduced.

We can accordingly define the effective mass as:

$$m_{\text{eff}}(t) \equiv \cosh^{-1}\Big[\frac{C^{2\text{pt}}(t+1)+C^{2\text{pt}}(t-1)}{2C^{2\text{pt}}(t)}\Big] \tag{4.2}$$

and in the region where the contributions from excited states and effects from the boundary condition are negligible, we expect a constant with a value of the meson mass m:

$$m_{\text{eff}}(t) = \cosh^{-1}\Big[\frac{e^{-m(t+1)}+e^{-m(t-1)}}{e^{-mt}}\Big] = \cosh^{-1}\Big[\cosh(m)\Big] = m. \tag{4.3}$$

Thus we can decide the range of our fitting based on the plateau in the plot of effective mass as a function of t.

4.1.2 Fitting three-point correlation functions

To remove the exponentially increasing terms, we have to calculate matrix elements such as: $\langle n|Q_i|K^0\rangle$, $\langle n|\bar{s}d|K^0\rangle$ and $\langle n|\bar{s}\gamma^5 d|K^0\rangle$. In our calculation, we don't need to calculate both $\langle\overline{K^0}|Q_i'|n\rangle$ and $\langle n|Q_i'|K^0\rangle$ since the two matrix elements are connected by CP transformation:

$$\langle\overline{K^0}|Q_i'|n\rangle = \langle\overline{K^0}|(CP)^{-1}CPQ_i'(CP)^{-1}CP|n\rangle = \epsilon(n)\langle n|Q_i'|K^0\rangle^*, \tag{4.4}$$

where $\epsilon(n)$ can take value ±1 depending on whether the $|n\rangle$ is the odd or even under CP. Thus we only calculate $\langle n|Q_i'|K^0\rangle$ and multiply it by the corresponding CP eigenvalue $\epsilon(n)$ to obtain $\langle\overline{K^0}|Q_i'|n\rangle$. For the light states considered in our calculation, we have:

$$\epsilon(\pi) = \epsilon(\eta) = 1, \tag{4.5}$$

$$\epsilon(0) = \epsilon(\pi\pi) = -1. \tag{4.6}$$

We need to calculate the $\langle\pi|Q_i'|K^0\rangle$ and $\langle\pi\pi_{I=0}|Q_i'|K^0\rangle$ matrix elements. To obtain these matrix elements from three-point correlation functions, based on the time dependence of the three-point

correlation functions shown in Equation 3.14 ,we can accordingly define the function to be fitted as:

$$\widetilde{C}^{Q_i}_{K\to\pi}(\Delta,t) \equiv \frac{C^{Q_i}_{K\to\pi}(\Delta,t)}{N_\pi N_K e^{-m_\pi(\Delta-t)}e^{-m_K t}}. \tag{4.7}$$

where Δ is the time separation between the kaon source and the pion sink and t is the time separation between the weak operator Q_i and the kaon source. An alternative definition which we use in our calculation is given by taking the ratio between three-point and two-point correlation functions:

$$\widetilde{C}^{Q_i}_{K\to\pi}(\Delta,t) \equiv \frac{N_\pi N_K C^{Q_i}_{K\to\pi}(\Delta,t)}{C^{2\mathrm{pt}}_\pi(\Delta-t)C^{2\mathrm{pt}}_K(t)}, \tag{4.8}$$

Similarly for the $\overline{s}d$ operator, we have the function to be fitted as:

$$\widetilde{C}^{\overline{s}d}_{K\to\pi}(\Delta,t) \equiv \frac{N_\pi N_K C^{\overline{s}d}_{K\to\pi}(\Delta,t)}{C^{2\mathrm{pt}}_\pi(\Delta-t)C^{2\mathrm{pt}}_K(t)}. \tag{4.9}$$

We expect $\widetilde{C}^{Q_i}_{K\to\pi}(\Delta,t)$ and $\widetilde{C}^{\overline{s}d}_{K\to\pi}(\Delta,t)$ to be constants, in the region of various values of Δ and t where the contributions from excited states and effects from the periodicity in time are negligible, and their values should be equal to the matrix elements $\langle\pi^0|Q_i|K^0\rangle$ and $\langle\pi^0|\overline{s}d|K^0\rangle$ separately.

In order to calculate the $\langle\pi^0|Q'_i|K^0\rangle$ and $\langle\pi\pi_{I=0}|Q'_i|K^0\rangle$ matrix elements, we need to calculated the coefficients defined in Equation 4.10. The corresponding ratio functions to be fitted are defined as:

$$\mathcal{R}^{Q_i}_{\mathrm{s}i}(\Delta,t) \equiv \frac{C^{Q_i}_{K\to\eta}(\Delta,t)}{C^{\overline{s}d}_{K\to\eta}(\Delta,t)}, \quad \mathcal{R}^{Q_i}_{\mathrm{p}i}(\Delta,t) \equiv \frac{C^{Q_i}_{K\to 0}(\Delta,t)}{C^{\overline{s}\gamma_5 d}_{K\to 0}(\Delta,t)}. \tag{4.10}$$

We expect the ratio functions have constant values, in the region of various values of Δ and t where the contributions from excited states and effects from the periodicity in time are negligible, and their values should equal to the coefficients $c_{\mathrm{s}i}$ and $c_{\mathrm{p}i}$ defined in Equation 4.10 separately.

4.1.3 Fitting three-point correlation functions with multiple source-sink separations

The diagrams with self-loop propagators are usually noisy and for disconnected diagrams, the statistical noise does not decrease as the disconnected parts are separated farther from each

other. We therefore increase the statistics of the diagrams with self-loop propagators by combining correlation functions with different source-sink separations. It's important to note that for three point correlation functions, we calculate connected and disconnected diagrams together with N_{sep} source-sink separations $\Delta \in \{\Delta_{\text{min}}, \Delta_{\text{min}} + \Delta_{\text{step}}, \Delta_{\text{min}} + 2\Delta_{\text{step}}, ..., \Delta_{\text{max}}\}$, where $\Delta_{\text{step}} = \frac{\Delta_{\text{max}} - \Delta_{\text{min}}}{N_{\text{sep}}}$. However, for four-point correlation functions, we calculate type-1, type-2 and type-3 diagrams with a single value of Δ and calculate disconnected type-4 diagrams with multiple values of Δ.

For the three-point correlation functions, we relabel the variables of the correlation functions. We define the time separation between the weak operator and the meson sink to be:

$$\delta = \Delta - t, \tag{4.11}$$

and we average the three-point quantities with the same δ value among all the allowed source-sink separations Δ as shown in Figure 4.1.

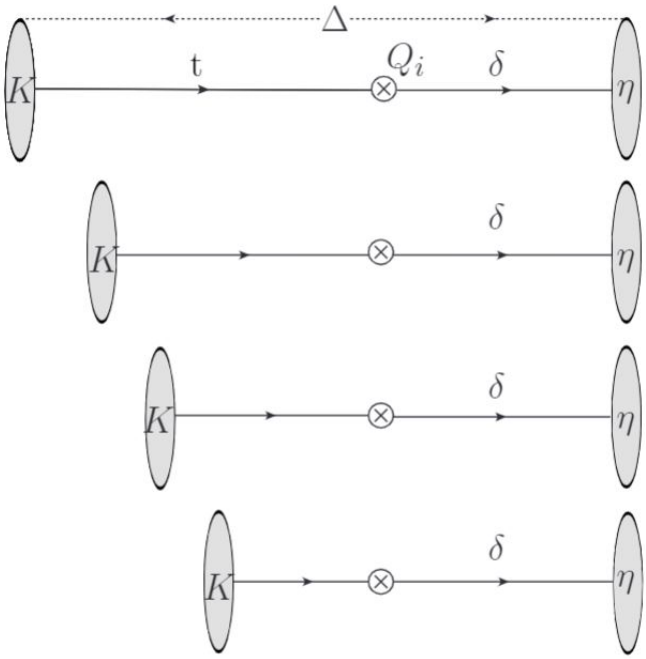

Figure 4.1: Error-weighted average among three-point correlation functions with multiple source-sink separation Δ for a specific operator-sink separation δ.

For the fitting of kaon to eta three-point correlation functions, we first obtain $\mathcal{R}_{si}^{Q_i}(\Delta, \delta)$ with

the same δ value for all allowed source-sink separations Δ and perform an error-weighted average to obtain:

$$\widetilde{\mathcal{R}}_{si}^{Q_i}(\delta) = \left\langle \mathcal{R}_{si}^{Q_i}(\Delta,\delta) \right\rangle_\Delta = \left\langle \frac{C_{K\to\eta}^{Q_i}(\Delta,\delta)}{C_{K\to\eta}^{\bar{s}d}(\Delta,\delta)} \right\rangle_\Delta , \tag{4.12}$$

where $\left\langle ... \right\rangle_\Delta$ denotes the error weighted average among all possible Δ values.

We then obtain the coefficients c_{si} by fitting the plateaus in the plots of $\widetilde{\mathcal{R}}_{si}^{Q_i}(\delta)$ to constants. In order to avoid excited state contamination, when performing the fitting, we include only $\widetilde{\mathcal{R}}_{si}^{Q_i}(\delta)$ with $\delta \geq t_{\text{min}}$, where t_{min} is the minimum time separation we set between the operator and meson sink.

Similarly, for the matrix elements $\langle \pi\pi_{I=0}|Q_i'|K^0\rangle$, we first average $C_{K\to\pi\pi_{I=0}}^{Q_i'}(\Delta,\delta)$ with the same δ value among all the allowed source-sink separations Δ and obtain:

$$\widetilde{\overline{C}}_{K\to\pi\pi_{I=0}}^{Q_i'}(\delta) = \left\langle \widetilde{C}_{K\to\pi\pi_{I=0}}^{Q_i'}(\Delta,t) \right\rangle_\Delta = \left\langle \frac{N_{\pi\pi_{I=0}} N_K C_{K\to\pi\pi_{I=0}}^{Q_i'}(\Delta,\delta)}{C_{\pi\pi_{I=0}}^{\text{2pt}}(\Delta-t) C_K^{\text{2pt}}(t)} \right\rangle_\Delta , \tag{4.13}$$

where $\left\langle ... \right\rangle_\Delta$ denotes the error weighted average among all possible Δ values. We then obtain the matrix elements $\langle \pi\pi_{I=0}|Q_i'|K^0\rangle$ by fitting the plateaus in the plots of $\widetilde{\overline{C}}_{K\to\pi\pi_{I=0}}^{Q_i'}(\delta)$ to constants.

As we can see from Figure 4.1, the statistics of the quantities with smaller δ values is larger compared to the case of larger δ where only a few source-sink separations will be possible.

4.1.4 Fitting four-point correlation functions with single-integration method

The fitting of the integrated correlator in Equation 3.5 can be separated into fitting the integrated correlator with Q_1' and Q_2':

$$\mathcal{A}_{ij}^S(T) = N_K^2 e^{-m_K(t_f - t_i)} \sum_n \frac{\langle \overline{K^0}|Q_i'|n\rangle\langle n|Q_j'|K^0\rangle}{m_K - E_n} \{-1 + e^{-(E_n - m_K)T}\}. \tag{4.14}$$

The relationship between $\mathcal{A}_{ij}^{S}(T)$ in Equation 4.14 and $\mathcal{A}^{S}(T)$ in Equation 3.5 is thus given by:

$$\mathcal{A}^{S}(T) = \lambda_u^2 \sum_{i,j=1,2} C_i C_j \mathcal{A}_{ij}^{S}(T), \tag{4.15}$$

where the C_i are Wilson coefficients and $\lambda_u = V_{ud}V_{us}^* = \cos\theta_c \sin\theta_c$.

To find out the T_{cut} where the exponential terms are negligible and calculate Δm_K, we analyze the four-point correlation functions in the following steps:

1. Perform an average of unintegrated correlators over all allowed values of kaon source time t_i:

$$G(\Delta, t_x, t_y) = \frac{1}{L_t} \sum_{t_i=1}^{L_t} G(t_1 = t_x + t_i, t_2 = t_y + t_i, t_i, t_f = t_i + \Delta). \tag{4.16}$$

   For each Δ value, we have the time difference between the two weak operators, $\delta = |t_x - t_y|$ ranging from 0 to Δ and for each δ values we perform an average over all the possible t_x and t_y pairs:

$$\overline{G}(\Delta, \delta) = \frac{1}{\Delta'' - \delta + 1} \sum_{t_x = t_{\text{min,K}}}^{\Delta' - \delta} G(\Delta, t_x, t_x + \delta), \tag{4.17}$$

   where $\Delta'' = \Delta - 2t_{\text{min,K}}$, $\Delta' = \Delta - t_{\text{min,K}}$ and $t_{\text{min,K}}$ is the minimum time separation between the operator and the kaon source or the kaon sink. We divided the averaged unintegrated correlator $\overline{G}(\Delta, \delta)$ by the factor $N_K^2 e^{-m_K \Delta}$ to normalize it and obtain:

$$\widetilde{G}(\delta) = \frac{\overline{G}(\Delta, \delta)}{N_K^2 e^{-m_K \Delta}}. \tag{4.18}$$

2. Subtract light states from the averaged unintegrated correlator:

$$\begin{aligned} \widetilde{G}^{\text{sub}}(\delta) &= \widetilde{G}(\delta) - \sum_{n \in \{n_l\}} \langle \overline{K^0} | H_W | n \rangle \langle n | H_W | K^0 \rangle e^{(m_K - E_n)\delta} \\ &= \sum_{n \neq n_l} \langle \overline{K^0} | H_W | n \rangle \langle n | H_W | K^0 \rangle e^{(m_K - E_n)\delta}, \end{aligned} \tag{4.19}$$

   where $\{n_l\}$ denotes the set of light states n_l to be subtracted. We can plot the subtracted

unintegrated correlator as a function of δ and identify an appropriate value of $\delta = \delta_{\text{cut}}$ where the value of the correlator is consistent with zero within the errors.

3. Perform a single-integration over δ of the subtracted correlator between $\delta = 0$ and $\delta = T$ to obtain:

$$\widetilde{\mathcal{A}}^S(T) = \sum_{\delta=1}^{T} \widetilde{G}^{\text{sub}}(\delta) + \frac{1}{2}\widetilde{G}^{\text{sub}}(0) = \sum_{n \neq n_l} \frac{\langle \overline{K^0} | H_W | n \rangle \langle n | H_W | K^0 \rangle}{m_K - E_n} \{-1 + e^{-(E_n - m_K)T}\}. \quad (4.20)$$

With this combination of $\delta > 0$ and $\delta = 0$ terms, the sums in Equation 4.20 are equivalent to a continuum integral over δ up to terms of $O(a^2)$, provided the sum over δ extends to the region where $\widetilde{G}(\delta) = 0$.

We can separate the subtracted integrated correlators $\widetilde{\mathcal{A}}^S(T)$ into the subtracted correlators with operators Q'_1 and Q'_2:

$$\begin{aligned} \widetilde{\mathcal{A}}^S_{ij}(T) &= \sum_{\delta=1}^{T} \widetilde{G}^{\text{sub}}_{ij}(\delta) + \frac{1}{2}\widetilde{G}^{\text{sub}}_{ij}(0) \\ &= \sum_{n \neq n_l} \frac{\langle \overline{K^0} | Q'_i | n \rangle \langle n | Q'_j | K^0 \rangle}{m_K - E_n} \{-1 + e^{-(E_n - m_K)T}\}, \end{aligned} \quad (4.21)$$

where $\widetilde{G}^{\text{sub}}_{ij}$ is the subtracted four-point correlator with weak operators Q'_i and Q'_j:

$$\begin{aligned} \widetilde{G}^{\text{sub}}_{ij}(\delta) &= \widetilde{G}_{ij}(\delta) - \sum_{n \in \{n_l\}} \langle \overline{K^0} | Q'_i | n \rangle \langle n | Q'_j | K^0 \rangle e^{(m_K - E_n)\delta} \\ &= \sum_{n \neq n_l} \langle \overline{K^0} | Q'_i | n \rangle \langle n | Q'_j | K^0 \rangle e^{(m_K - E_n)\delta}, \end{aligned} \quad (4.22)$$

and $\widetilde{G}_{ij}(\delta)$ is similar to the $\widetilde{G}(\delta)$ in Equation 4.18 but with the two H_W operators replaced by operators Q'_i and Q'_j.

4. Plot the single-integrated correlator as a function of T and find a value of $T = T_{\text{cut}}$ where $\widetilde{\mathcal{A}}^S_{ij}$

converges to a constant within errors:

$$\widetilde{\mathcal{A}}_{ij}^{S}(T_{\text{cut}}) \approx -\sum_{n\neq n_l} \frac{\langle\overline{K^0}|Q_i'|n\rangle\langle n|Q_j'|K^0\rangle}{m_K - E_n}. \tag{4.23}$$

The limits δ_{cut} and T_{cut} are expected to be close to each other.

5. Add light state contributions explicitly to $\widetilde{\mathcal{A}}_{ij}^{S}(T_{\text{cut}})$ and obtain the constant k_{ij} which is given by:

$$\begin{aligned} k_{ij} &\equiv \widetilde{\mathcal{A}}_{ij}^{S}(T_{\text{cut}}) - \sum_{n\in\{n_l\}} \frac{\langle\overline{K^0}|Q_i'|n\rangle\langle n|Q_j'|K^0\rangle}{m_K - E_n} \\ &\approx -\sum_{n} \frac{\langle\overline{K^0}|Q_i'|n\rangle\langle n|Q_j'|K^0\rangle}{m_K - E_n}. \end{aligned} \tag{4.24}$$

The value of Δm_K is then given by:

$$\Delta m_K^{\text{lat}} = \frac{G_F^2}{2}\lambda_u^2 \sum_{i,j=1,2} (-2) \times C_i^{\text{lat}} C_j^{\text{lat}} k_{ij}. \tag{4.25}$$

After we separate the contributions to Δm_K according to operator combinations $Q_i'Q_j'$, we can further categorise the contributions from different diagram topologies for each $Q_i'Q_j'$ combination.

Compared to the double-integration method used in earlier Δm_K calculations[1] [7], the method discussed here leads to a result with smaller statistical errors. Details about the comparison between results from these two methods can be found in Chapter 6.

Type-1 and type-2 diagrams are all connected and contain no self-loop propagators. For each diagram, we have one of the weak operator on site x and another weak operator on site y. If we denote the spacial volume as V and the size of time integration range as T, the number of the point-source-point-sink propagators we need to calculate is of order $O(TV)$ and number of contractions is of order $O(TV^2)$. In addition, because all parts of the diagrams are connected to each other, we cannot decompose the diagrams into independent pieces and calculate them separately. This large

number of propagators and contractions is not practical.

In our calculation, instead of calculating $O(TV)$ propagators, we simplify the calculation to reduce the number of propagators to be of order $O(T)$ and the number of contractions to be of order $O(TV)$. To do this, we specify one of the weak operators and sum over all sites $y = (\vec{r}, t_y)$ with the same time value t_s, and the other operator as the source on site $x = (4t_x, 4t_x, 4t_x, t_x)$, for all $t_x \in [t_{min}, t_{max}]$ which is the range of integration. By doing this, only one of the sites on each time slice t_x is sampled and we multiply it by the spacial volume factor V to keep the normalization same as the case where all the point-source-point-sink propagator pairs are calculated. This is demonstrated in Figure 4.2. As we can see, such a simplification introduces asymmetry between the operators on the site x and y. The two cases shown in Figure 4.2a and 4.2b in fact are the same correlation function calculated. In fact, we calculate the contractions both ways and average them to double the statistics.

For type-3 diagrams, as shown in Figure 4.3, the two weak operators are not connected directly by quark lines, thus we can decompose the calculation of the diagrams into upper and lower pieces for a specific source-sink separation. The number of propagators to be calculated for the upper and lower pieces are of order $O(TV)$ and we use A2A propagators which have been discussed in Chapter 3, to reduce this cost to $O(T)$.

For type-4 diagrams, the left half and the right half of each diagram are not connected by quark propagators. Therefore, we can calculate and contract the propagators by breaking the calculation into left and right pieces. The number of propagators to be calculated for the left and right pieces are also of order $O(TV)$ and A2A propagators are used to reduce this cost to $O(T)$.

4.2 Data analysis of type-4 diagrams

As shown in Figure 4.4, type-4 diagrams can be assembled from left and right pieces:

$$G^{\text{tp4}}(t_1, t_2, t_i, t_f) = G^{\text{left}}(t_1, t_i) \times G^{\text{right}}(t_2, t_f), \tag{4.26}$$

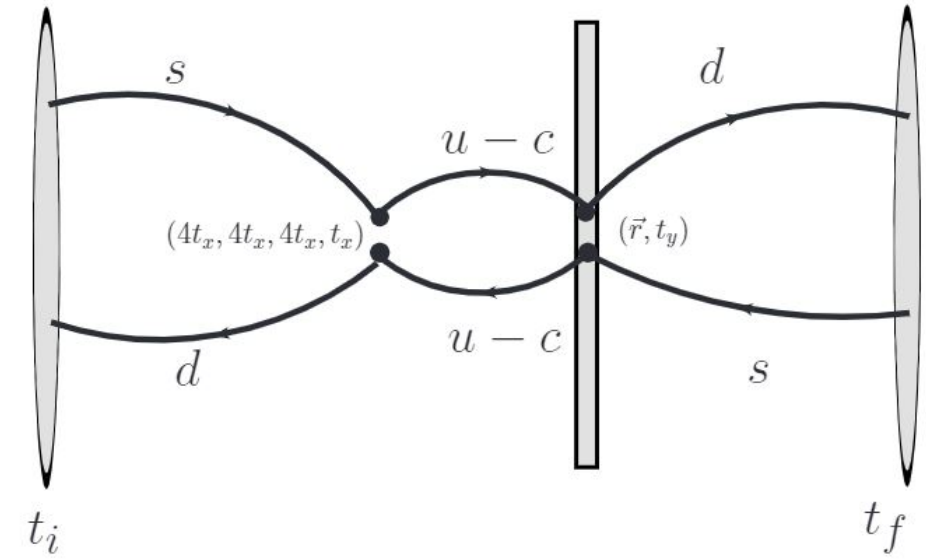

(a)

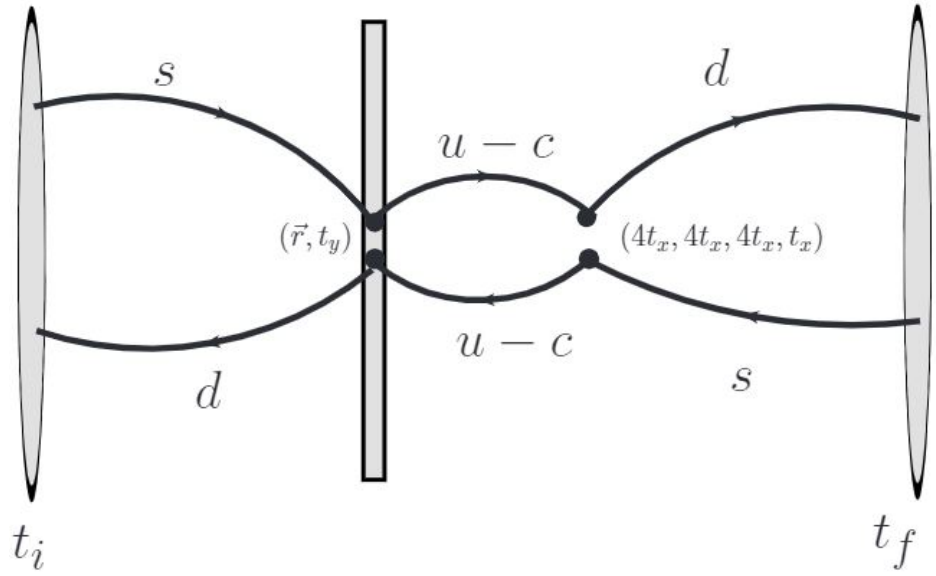

(b)

Figure 4.2: Type-1 and type-2 diagrams having point-source-point-sink propagators with different sink sites and a single point source but corresponding to the same quantity. The vertical grey band means there are multiple point sinks within the spacial volume at the same time.

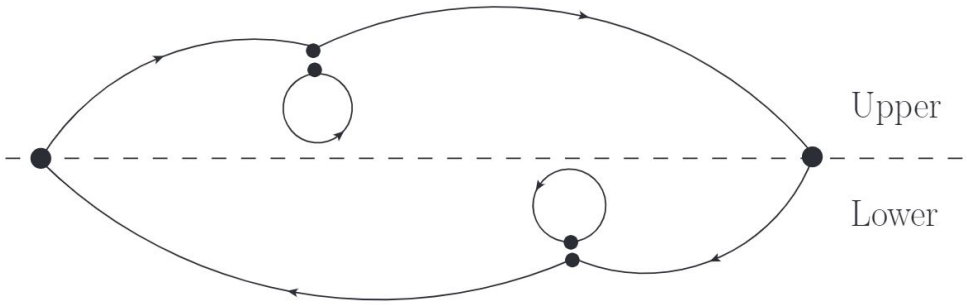

Figure 4.3: A typical type-3 diagram having separable upper and lower pieces. The single dots correspond to the K^0 and $\overline{K^0}$ operators while the paired dots correspond to the weak four-quark operator.

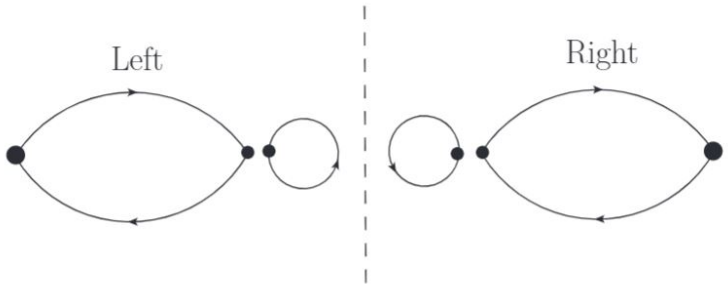

Figure 4.4: A typical type-4 diagram having disconnected left and right pieces.The single dots correspond to the K^0 and $\overline{K^0}$ operators while the paired dots correspond to the weak four-quark operator.

and thus we can calculate left and right pieces separately and assemble type-4 diagrams with all allowed source-sink separations Δ to increase the statistics.

4.2.1 Fitting type-4 diagrams with multiple source-sink separations

We obtain the error weighted average of the four-point type-4 correlation functions $\overline{\overline{G}}(\delta)$ in three steps:

1. Combine the left and right pieces of diagrams averages for all possible kaon sources on all time slices and normalize them to get the type-4 correlators:

$$G(\Delta, t_x, t_y) = \frac{1}{L_t} \sum_{t_i=1}^{L_t} G^{\text{tp4}}(t_1 = t_x + t_i, t_2 = t_y + t_i, t_i, t_f = t_i + \Delta). \tag{4.27}$$

2. For each Δ value, we have the time difference between the two weak operators, $\delta = |t_x - t_y|$ ranging from 0 to Δ and for each δ values we perform an average over all the possible t_x and t_y pairs:

$$\overline{G}(\Delta, \delta) = \frac{1}{\Delta'' - \delta + 1} \sum_{t_x=t_{\text{min,K}}}^{\Delta'-\delta} G(\Delta, t_x, t_x + \delta), \tag{4.28}$$

   where $\Delta'' = \Delta - 2t_{\text{min,K}}$, $\Delta' = \Delta - t_{\text{min,K}}$ and $t_{\text{min,K}}$ is the minimum time separation between the operator and the kaon source or the kaon sink.

3. We then normalize $\overline{G}(\Delta, \delta)$ and perform an error-weighted average over all allowed values of Δ to obtain the type-4 unintegrated correlators:

$$\overline{\overline{G}}(\delta) = \left\langle \frac{\overline{G}(\Delta, \delta)}{N_K^2 e^{-m_K \Delta}} \right\rangle_\Delta, \tag{4.29}$$

   where $\left\langle ... \right\rangle_\Delta$ denotes the error weighted average among all allowed Δ values.

4.2.2 Removal of random source correlations in type-4 diagrams

We are using a random source to build the self-loop propagators $S_x^R(x)$ which are obtained by averaging propagators calculated from $n_{\rm hit}$ random hits. The details about how to build the self-loop propagators using A2A propagators have been discussed in Section 3.3.2. The type-4 diagrams are then constructed as a product of left and right factors, each contracted from an operator Q_i including a product containing a self-loop propagator. We can symbolically write the left and right factors as sums of contractions calculated from each random hit i:

$$G^{\rm left} = \frac{1}{n_{\rm hit}} \sum_{i=1}^{n_{\rm hit}} L_i, \quad G^{\rm right} = \frac{1}{n_{\rm hit}} \sum_{j=1}^{n_{\rm hit}} R_j. \tag{4.30}$$

When we multiply the left and right factors together to obtain a type-4 correlator:

$$G^{\rm tp4} = (\frac{1}{n_{\rm hit}} \sum_{i=1}^{n_{\rm hit}} L_i) \times (\frac{1}{n_{\rm hit}} \sum_{j=1}^{n_{\rm hit}} R_j), \tag{4.31}$$

there are $n_{\rm hit}$ pairs with a left piece L_i and a right factor R_i which are calculated from the same random hit and therefore have unwanted correlations. Thus we need to remove all these terms which are given by:

$$C = \sum_{i=1}^{n_{\rm hit}} L_i \times R_i, \tag{4.32}$$

and rewrite our subtracted type-4 diagrams with a new normalization factor as:

$$G^{\rm tp4} = \frac{1}{n_{\rm hit}^2 - n_{\rm hit}} \Big(\sum_{i=1}^{n_{\rm hit}} L_i \times \sum_{j=1}^{n_{\rm hit}} R_j - \sum_{i=1}^{n_{\rm hit}} L_i \times R_i \Big) \tag{4.33}$$

or equivalently to be:

$$\begin{aligned} G^{\rm tp4} &= \frac{n_{\rm hit}}{n_{\rm hit} - 1} \Big[G^{\rm left} \times G^{\rm right} - \frac{1}{n_{\rm hit}^2} C \Big] \\ &= \frac{n_{\rm hit}}{n_{\rm hit} - 1} \Big[(\frac{1}{n_{\rm hit}} \sum_{i=1}^{n_{\rm hit}} L_i) \times (\frac{1}{n_{\rm hit}} \sum_{j=1}^{n_{\rm hit}} R_j) - \frac{1}{n_{\rm hit}^2} \sum_{i=1}^{n_{\rm hit}} L_i \times R_i \Big]. \end{aligned} \tag{4.34}$$

For a diagram contracted from $\overline{s}d$ or $\overline{s}\gamma_5 d$ operators, at most one of the left or right pieces contains a self-loop propagator. Therefore there is no correlated hit contribution to be subtracted.

Furthermore, instead of calculating all the n_{hit} hits to obtain C, we make an simplification in which the average of only n_{sub} hits are calculated:

$$\langle L_i \times R_i \rangle = \frac{1}{n_{\text{sub}}} \sum_{i=1}^{n_{\text{sub}}} L_i \times R_i \tag{4.35}$$

and C is approximated as:

$$\sum_{i=1}^{n_{\text{hit}}} L_i \times R_i \approx \langle C \rangle = \langle L_i \times R_i \rangle \times n_{\text{hit}} = \frac{n_{\text{hit}}}{n_{\text{sub}}} \sum_{i=1}^{n_{\text{sub}}} L_i \times R_i. \tag{4.36}$$

Substituting this into Equation 4.34, we obtain:

$$\begin{aligned} G^{\text{tp4}} &= \frac{n_{\text{hit}}}{n_{\text{hit}} - 1} \left[G^{\text{left}} \times G^{\text{right}} - \frac{1}{n_{\text{hit}}} \langle C \rangle \right] \\ &= \frac{n_{\text{hit}}}{n_{\text{hit}} - 1} \left(\frac{1}{n_{\text{hit}}} \sum_{i=1}^{n_{\text{hit}}} L_i \right) \times \left(\frac{1}{n_{\text{hit}}} \sum_{j=1}^{n_{\text{hit}}} R_j \right) - \frac{1}{(n_{\text{hit}} - 1) \times n_{\text{sub}}} \sum_{i=1}^{n_{\text{sub}}} L_i \times R_i \end{aligned} \tag{4.37}$$

4.3 Calculating Δm_K from four-point correlation function data

As discussed in Section 4.1.4 and Section 4.2.1, we use the averaged unintegrated correlator for the calculation of Δm_K using single-integration method. The averaged single-integrated correlator in Equation 4.20 is obtained from averaged unintegrated correlator in Equation 4.19 :

$$\widetilde{\mathcal{A}}^S(T) = \sum_{\delta=1}^{T} \widetilde{G}(\delta) + \frac{1}{2} \widetilde{G}(0). \tag{4.38}$$

In this section, we will show how our four-point correlation function data is used in the calculation of the averaged unintegrated correlator $\widetilde{G}(\delta)$. In our lattice calculation, we distinguish the weak operator contracted to the kaon source and the weak operator contracted with the kaon sink. In

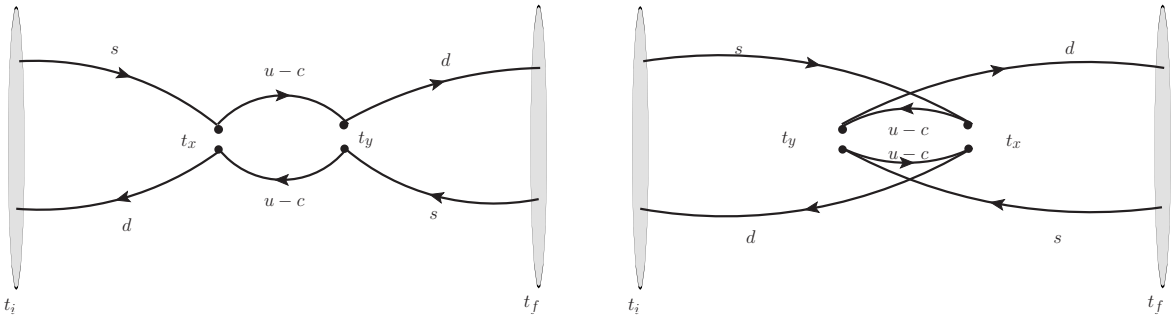

(a) data matrix element $\mathcal{G}^{\Delta}_{t_1,t_2}$, with $t_1 < t_2, t_x = t_1, t_y = t_2$ (b) data matrix element $\mathcal{G}^{\Delta}_{t_2,t_1}$, with $t_1 < t_2, t_x = t_2, t_y = t_1$

Figure 4.5: The four-point contraction data stored in a matrix $\mathcal{G}^{\Delta}_{t_x,t_y}$, where the t_x labels the operator contracted to the kaon source while the t_y labels the operator contracted to the kaon sink. t_1 and t_2 label the matrix indices according to the time of the two operators.

our analysis of the data obtained from lattice calculation, we first average the contracted four-point correlation functions over all allowed kaon source positions t_i as in Equation 4.16, and save them in a two-dimensional data matrix $\mathcal{G}^{\Delta}_{t_x,t_y}$, where the superscript Δ denotes the source-sink separation of the four-point correlation functions. The first index t_x labels the time difference between the kaon source and the operator contracted to the kaon source. The second index t_y labels the time difference between the kaon sink and the operator contracted to the kaon sink. Thus, for a certain set of values $t_1 = 5, t_2 = 10$ as an example, the related data matrix elements, both $\mathcal{G}^{\Delta}_{5,10}$ and $\mathcal{G}^{\Delta}_{10,5}$ shown in Figure 4.5a and 4.5b, should contribute to the same correlator $G(\Delta, t_x = 5, t_y = 10)$ defined in Equation 4.16, therefore the connection between our data matrix element and the averaged correlation function is given by:

$$\begin{aligned}
\widetilde{G}(\delta) &= \frac{\overline{G}(\Delta,\delta)}{N_K^2 e^{-m_K \Delta}} \\
&= \frac{1}{N_K^2 e^{-m_K \Delta}} \left[\frac{1}{\Delta'' - \delta + 1} \sum_{t_x = t_{\min,\mathrm{K}}}^{\Delta' - \delta} G(\Delta, t_x, t_x + \delta) \right] \\
&= \frac{1}{N_K^2 e^{-m_K \Delta}} \left[\frac{1}{\Delta'' - \delta + 1} \sum_{t = t_{\min,\mathrm{K}}}^{\Delta' - \delta} \left(\mathcal{G}^{\Delta}_{t,t+\delta} + \mathcal{G}^{\Delta}_{t+\delta,t} \right) \right], \quad \delta \neq 0,
\end{aligned} \tag{4.39}$$

where $\Delta'' = \Delta - 2t_{\text{min,K}}$, $\Delta' = \Delta - t_{\text{min,K}}$ and $t_{\text{min,K}}$ is the minimum time separation between the operator and the kaon source or the kaon sink. And for $\delta = 0$, the connection between our data matrix element and the averaged correlation function is given by:

$$\begin{aligned}\widetilde{G}(\delta = 0) &= \frac{\overline{G}(\Delta, \delta = 0)}{N_K^2 e^{-m_K \Delta}} \\ &= \frac{1}{N_K^2 e^{-m_K \Delta}} \left[\frac{1}{\Delta'' + 1} \sum_{t=t_{\text{min,K}}}^{\Delta'} 2\mathcal{G}_{t,t}^{\Delta} \right], \quad \delta = 0.\end{aligned} \tag{4.40}$$

Note, $\mathcal{G}_{t,t}^{\Delta}$ is defined the same as $\mathcal{G}_{t_x,t_y}^{\Delta}$ but with the specific values $t_x = t_y = t$.

4.4 Fitting Δm_K with statistical errors

After calculation of various correlation functions from N configurations, we need to fit the data with respect to the theoretical formula to extract the quantities we need to obtain Δm_K. At the same time, as shown in Equation 4.20-4.25, Δm_K is a complicated combination of the results from fitting two-point, three-point and four-point correlation functions. We evaluate the corresponding the statistical error of Δm_K using the jackknife method.

4.4.1 Fitting with the jackknife method

Suppose we have raw data blocks $R_i(t)$, with $i = 1, 2, ..., N$ from N lattice configurations, with t being the variable in a theoretical function $f(\Theta, t)$ to be fitted to determine the parameter Θ. Firstly, we create N single-jackknife blocks, with each single-jackknife block average $S_i(t)$ generated by $N - 1$ raw data blocks:

$$S_i(t) = \frac{1}{N-1} \sum_{j \neq i} R_j(t). \tag{4.41}$$

Then we can obtain the parameter Θ_i from fitting $S_i(t)$ to the theoretical function $f(\Theta, t)$ for each i, by minimizing the following quantity:

$$\chi_i^2 = \sum_{t,t'} [f(\Theta_i, t) - S_i(t)][f(\Theta_i, t') - S_i(t')]C^{(i)-1}(t, t'), \tag{4.42}$$

where $C^{(i)}$ is the correlation matrix for the ith jackknife block. In order to calculate $C^{(i)}$, we need to calculate the average over the jth double-jackknife block related to the fitting of ith single-jackknife block. The double-jackknife block is obtained by leaving out two data elements from the raw data block R and the average is given by:

$$D_j^{(i)} = \frac{(\sum_k R_k) - R_i - R_j}{N-2}, j \neq i. \tag{4.43}$$

In the cases where the average over the ith single-jackknife block S_i are available, we can also obtain $D_j^{(i)}$ from S_i:

$$D_j^{(i)} = \frac{(S_i + S_j) \times (N-1) - \sum_k S_k}{N-2}, j \neq i. \tag{4.44}$$

In our analysis, we have two sets of code with one of them using Equation 4.43 and the other one using Equation 4.44. We perform jackknife fitting using both sets of code and same results are obtained.

The correlation matrix $C^{(i)}$ is then given by:

$$C^{(i)}(t, t') = \frac{N-2}{N-1} \sum_{j \neq i} \left[D_j^{(i)}(t) - \overline{D}^{(i)}(t)\right]\left[D_j^{(i)}(t') - \overline{D}^{(i)}(t')\right], \tag{4.45}$$

where $D_j^{(i)}$ is the average over the jth double-jackknife block related to the fitting of ith single-jackknife block and $\overline{D}^{(i)}(t)$ is the mean of the $D_j^{(i)}$ which is given by:

$$\overline{D}^{(i)}(t) = \frac{1}{N-1} \sum_{j \neq i} D_j^{(i)}(t) = \frac{1}{N-1}\Big[\sum_k R_k(t) - R_i(t)\Big] = S_i(t). \tag{4.46}$$

If we only perform a uncorrelated fit, Equation 4.42 is simplified to be:

$$\chi_i^2 = \sum_t \frac{[f(\Theta_i, t) - S_i(t)]^2}{\sigma_i^2(t)}, \tag{4.47}$$

where $\sigma_i^2(t)$ is given by:

$$\sigma_i^2(t) = C^{(i)}(t,t) = \frac{N-2}{N-1} \sum_{j \neq i} \left[D_j^{(i)}(t) - \overline{D}^{(i)}(t) \right]^2. \tag{4.48}$$

After the fitting for each single-jackknife block, the mean of the fitting parameter Θ is given by[17]:

$$\overline{\Theta} = \frac{1}{N} \sum_{i=1}^{N} \Theta_i \tag{4.49}$$

with the statistical error:

$$\sigma_{\overline{\Theta}}^2 = \frac{N-1}{N} \sum_{i=1}^{N} (\Theta_i - \overline{\Theta})^2. \tag{4.50}$$

4.4.2 Application to Δm_K data analysis

On the ith configuration, after averaging over all possible kaon source time t_{src}, we obtain the raw data of the correlation function $\overline{G}_i^R(\Delta, \delta)$ as defined in Equation 4.17.

Then we perform jackknife resampling on the raw data from N configurations and obtain a single-jackknifed ensemble $\{\overline{G}_i^J(\Delta, \delta)\}, i = 1, ..., N$. The superscript J denotes that the single-jackknife resampling is performed. For type-1, type-2 and type-3 diagrams, we have only one Δ value. Thus for each single-jackknife block i, we remove the exponential time dependence using fitting results from two-point and three-point correlation functions from the same jackknife block, like $m_{K,i}^J, m_{\pi\pi,i}^J, m_{\eta,i}^J$ and obtain the single-jackknife unintegrated correlation function $\widetilde{G}_i^J(\delta)$ as defined in Equation 4.19.

For the case where we perform error weighted average among multiple source-sink separation Δ for each operator time difference δ, like for type-4 diagrams, we also need single-jackknifed $\overline{G^J}_i(\Delta, \delta)$ to obtain the error-weighted averaged unintegrated correlation functions $\overline{\widetilde{G^J}}_i(\delta)$ defined

in Equation 4.29.

Then, we obtain $(\Delta m_K)_i$ from the single-integrated correlator for each jackknife block and calculate the mean to be:

$$\langle \Delta m_K \rangle = \frac{1}{N} \sum_{i=1}^{N} (\Delta m_K)_i, \tag{4.51}$$

with the statistical error:

$$\sigma^2_{\Delta m_K} = \frac{N-1}{N} \sum_{i=1}^{N} \Big((\Delta m_K)_i - \langle \Delta m_K \rangle \Big)^2. \tag{4.52}$$

4.4.3 Sample all-mode averaging(AMA) corrections and the super-jackknife method

The super-jackknife method is used to estimate the uncertainty of combined data sets. In our calculation, for type-3 and type-4 diagrams, three-point and two-point functions, we have data from "sloppy" calculations to be combined with data from sample AMA corrections which have been discussed in Section 3.3.3. Here I will present the application of super-jackknife method in our calculation.

For a certain quantity Y, a pion correlator as an example, from the data $\{y_i\}_{i=1,\ldots,N_s}$ caculated on N_s "sloppy" configurations, we obtain the jackknife "sloppy" ensemble $\{Y_i\}_{i=1,\ldots,N_s}$ with $Y_i = \frac{1}{N_s-1} \sum_{j\neq i} y_j$. Similarly, from the corrections $\{\Delta y_i\}_{i=1,\ldots,N_c}$ calculated on other N_c configurations, we obtain the jackknife correction ensemble $\{\Delta Y_i\}_{i=1,\ldots,N_c}$ with $\Delta Y_i = \frac{1}{N_c-1} \sum_{j\neq i} \Delta y_j$. As shown in Figure 4.6, we then combine the two jackknife ensembles to form a super-jackknife ensemble $\{Y'_k\}_{k=1,\ldots,N_s+N_c}$ with $N_s + N_c$ elements, where the super-jackknife data block Y'_k is given by:

$$Y'_k = Y_k + \overline{\Delta Y}, \quad k = 1, \ldots N_s \tag{4.53}$$

$$Y'_k = \overline{Y} + \Delta Y_{k-N_s}, \quad k = N_s + 1, \ldots N_s + N_c \tag{4.54}$$

where $\overline{\Delta Y} = \frac{1}{N_c} \sum_{j=1}^{N_c} \Delta Y_j$ is the mean value of the corrections and $\overline{Y} = \frac{1}{N_s} \sum_{i=1}^{N_s} Y_i$ is the mean value of the "sloppy" results.

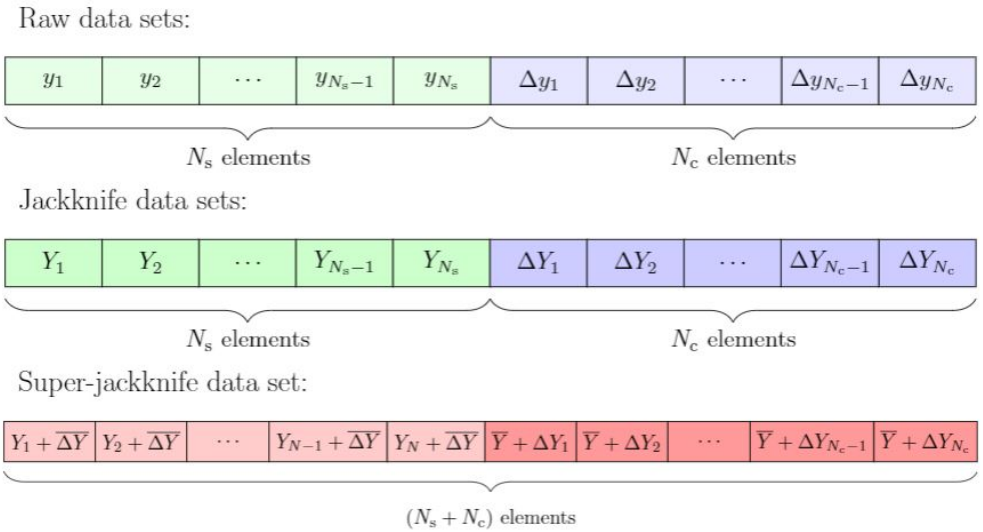

Figure 4.6: Combination of two jackknife ensembles with the super-jackknife method.

After the fitting for each super-jackknife block, the mean of the fitting parameter Θ is given by:

$$\overline{\Theta} = \frac{1}{N_s + N_c} \sum_{i=1}^{N_s+N_c} \Theta_i \tag{4.55}$$

with the statistical error:

$$\sigma^2_{\overline{\Theta}} = \frac{N_s + N_c - 1}{N_s + N_c} \sum_{i=1}^{N_s+N_c} (\Theta_i - \overline{\Theta})^2. \tag{4.56}$$

Chapter 5: Systematic errors and normalization factors

In this chapter, we will discuss the systematic errors of our Δm_K calculation. In Section 5.1, we will discuss corrections to Δm_K from finite volume effects. In Section 5.2, we will discuss estimation of the systematic error introduced by the around-the-world effects. In Section 5.3, by using a free-field calculation, we will show that the four-point contractions in our calculation method yields results consistent with the Inami-Lim calculation[3] in the local limit. In Section 5.4, we will show consistency of NPR factors used for Δm_K with other published NPR values. Last but not least, in Section 5.5, we will estimate the systematic error from finite lattice spacing effects.

5.1 Finite volume effects

Lattice calculations are performed with a finite space-time volume rather than an infinite volume and therefore corrections from finite volume effects are needed. In the case where there is no multi-particle state, finite volume corrections are exponentially suppressed in the lattice size L and can be made small. However, in the case where multi-particle states exist, the scattering among these particles in the finite volume leads to correction terms suppressed by power of L which are usually not negligible.

In our Δm_K calculation, the intermediate states include multiple particle states and the finite-volume effects coming from the scattering among these particles have to be corrected. Especially, we are interested in the contribution to the finite-volume effects from the two-pion intermediate state. This has been discussed in [8] and the finite volume correction to Δm_K, $\delta(\Delta m_K)^{FV}$, is obtained from the correction to the kaon mixing matrix element M_{12} which is given by:

$$\delta(\Delta m_K)^{FV} = 2Re(\delta M_{12}), \tag{5.1}$$

$$M_{12}^{\infty} = M_{12}^{V} + \delta M_{12}, \tag{5.2}$$

where M_{12}^{∞} is the matrix element calculated in infinite volume given by:

$$M_{12}^{\infty} = \mathcal{P} \int_{2m_\pi}^{\infty} dE \sum_{\alpha} \frac{\langle \overline{K^0} | H_W | \alpha, m_K \rangle^{\infty\infty} \langle \alpha, m_K | H_W | K^0 \rangle}{m_K - E}, \tag{5.3}$$

where E labels the intermediate-state energy and α labels the other degrees of freedom. M_{12}^{V} is the matrix element calculated in finite volume V and is given by:

$$M_{12}^{V} = \sum_{n} \frac{\langle \overline{K^0} | H_W | n \rangle^{V'V'} \langle n | H_W | K^0 \rangle}{m_K - E_n}. \tag{5.4}$$

The correction δM_{12} is given by:

$$\delta M_{12} = -\cot(h(m_K)) \frac{dh(E)}{dE}\Big|_{E=m_K} \times f(m_K), \tag{5.5}$$

where $f(m_K)$ is a product of finite-volume matrix elements with volume V' which leads to $E_{\pi\pi} = m_K$:

$$f(m_K) = \langle \overline{K}^0 | H_W | \pi\pi_{E=m_K} \rangle^{V'V'} \langle \pi\pi_{E=m_K} | H_W | K^0 \rangle. \tag{5.6}$$

The function $h(E)$ is obtained from Lüscher's quantization condition for a two-pion system in a spatial box of size $L \times L \times L$ with periodic boundary conditions:

$$h(E, L) \equiv \phi(\frac{kL}{2\pi}) + \delta_0(E) = \phi(q) + \delta_0(k) = n\pi, \tag{5.7}$$

$$E^2 = 4(m_\pi^2 + k^2), \quad q \equiv kL/2\pi, \tag{5.8}$$

where $n = 1, 2, ...$ labels the energy levels in increasing order and $\phi(q)$ is a kinematic function defined in [18] which can be calculated using Equation (3) and (A9) in [19]. $\delta_0(k)$ is the S-wave scattering phase shift.

As for the derivative term $\frac{dh}{dE}$ evaluated at $E = m_K$ in Equation 5.5, we calculate it using:

$$\frac{dh}{dE} = \frac{d\phi(q)}{dq}\frac{dq}{dE} + \frac{d\delta_0(k)}{dk}\frac{dk}{dE} = \frac{q\phi'(q) + k\delta_0'(k)}{4\pi k^2}E. \tag{5.9}$$

We approximate the derivative term $\delta_0'(k)$ with the scattering length a_0:

$$\delta_0'(k) \equiv \frac{d\delta_0(k)}{dk} \approx a = \lim_{k\to 0}\frac{\delta_0(k)}{k}. \tag{5.10}$$

and approximate the phase shift $\delta_0(k)$ appeared in $\cot(h(m_K))$ as:

$$\delta_0(k) \approx \delta_0(0) + \frac{d\delta_0(k)}{dk}k \approx a_0 k, \tag{5.11}$$

especially for $k = k_{m_K}$, where $m_K^2 = 4(m_\pi^2 + k_{m_K}^2)$ is satisfied. The approximation we make is intended to yield an estimate on the magnitude of the finite volume corrections with a relative low accuracy. The scattering length a_0 can be solved from the energy of the two-pion state $E_{\pi\pi}$ using Equation (3.1) and (3.2) in [20]:

$$E_{\pi\pi} = 2m_\pi - \frac{4\pi a}{m_\pi L^3}\left\{1 + c_1\frac{a}{L} + c_2\frac{a^2}{L^2}\right\} + O(L^{-6}), \tag{5.12}$$

$$c_1 = -2.837297, c_2 = 6.375183. \tag{5.13}$$

For the two-pion state with $I = 2$, $f(m_K)$ is negligible compared to the value for the two-pion state with $I = 0$, and we will consider only the contribution from the two-pion $I = 0$ state. The results for the finite volume corrections to our Δm_K calculation on the 64I lattice ensemble is given in Table 5.1.

$2f(m_k)$	$h = \delta + \phi$	$\cot h$	dh/dE	$\cot h \times dh/dE$	$\delta(\Delta m_K)^{FV}$
−0.0086(25)	−0.49(6)	−1.85(27)	33.5(4)	−62(10)	−0.54(18)

Table 5.1: The $\pi\pi_{I=0}$ contribution to the finite volume correction of Δm_K, and the relevant terms. The last term is the finite volume corrections to Δm_K, in units of 10^{-12} MeV.

5.2 The around-the-world effects

The around-the-world effects, refer to contributions to the correlation functions where propagation occurs through the boundary in the time direction, a contribution which would decrease exponentially as the length of the lattice volume in the time direction is increased. In our calculation of the three-point correlators in addition to the time dependence described in Chapter 4 and suggested by the propagation paths shown in Figure 5.1a, we have the alternative path contributing to the around-the-world effects as shown in Figure 5.1b. We expect the time-dependence of the three-point correlation functions with the around-the-world effects included to be approximately given by:

$$C^{Q_\pm}_{K\to\pi}(\Delta,t) \propto \langle\pi|Q_\pm|K^0\rangle e^{-m_K t} e^{-m_\pi(\Delta-t)} + \langle 0|Q_\pm|K^0,\pi\rangle e^{-m_K t} e^{-m_\pi[T-(\Delta-t)]}, \tag{5.14}$$

where the first term on the right hand side is the term we fit as discussed in Chapter 4 and the second term on the right hand side is due to the around-the-world effects. For a small value of t which is also large enough so that contributions from the excited states are negligible, the second term is greatly suppressed by a factor of $\frac{e^{-m_\pi(T-\tau)}}{e^{-m_\pi\tau}} = e^{-m_\pi(T-2\tau)}$, where $\tau = \Delta - t$.

To better estimate the relative magnitude of the around-the-world effects, we need not only know the suppression from the exponential time dependence, but also the magnitudes of the matrix elements $\langle\pi|Q_\pm|K^0\rangle$ and $\langle 0|Q_\pm|K^0,\pi\rangle$. We notice[21] that when the operator is outside the region between the source and sink as shown in Figure 5.2, the correlation function can be written as:

$$C^{Q_\pm}_{K\to\pi}(\Delta, t=\Delta+t') \propto \langle 0|Q_\pm|K^0,\pi\rangle e^{-m_K\Delta} e^{-(m_K+m_\pi)t'} + \langle\pi|Q_\pm|K^0\rangle e^{-m_K[T-(\Delta+t')]} e^{-m_\pi t'}, \tag{5.15}$$

where t' denotes the time difference between the operator and pion sink and for simplicity we neglect the effects of $K-\pi$ scattering and use $m_K + m_\pi$ for this two particle energy. The ratio between the exponential factors of the second term and the first term is $\frac{e^{-m_K(T-\tau')}}{e^{-m_K\tau'}} = e^{-m_K(T-2\tau')}$, where $\tau' = \Delta + t'$, and therefore when $\tau' < \frac{T}{2}$, the first term dominates.

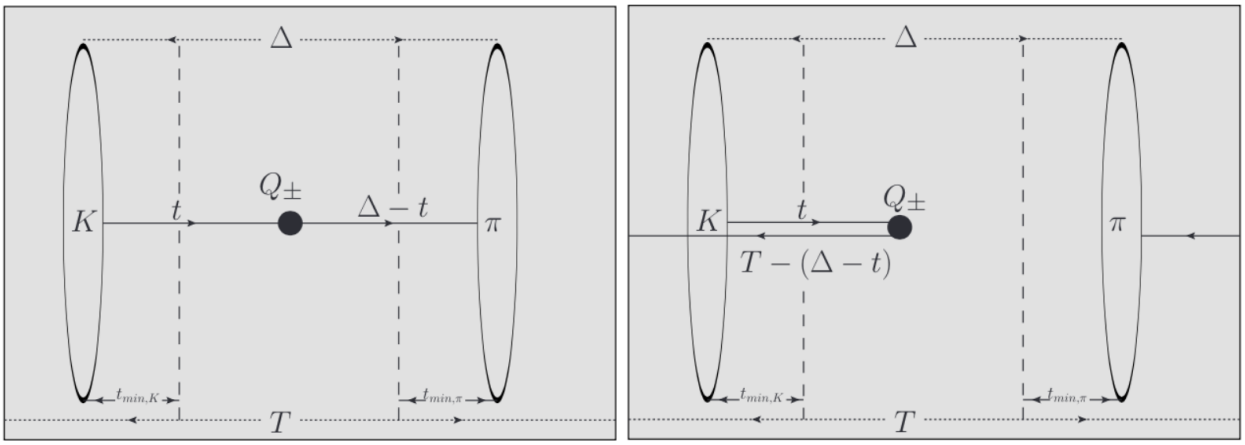

(a) (b)

Figure 5.1: $K \to \pi$ correlator when the operator is located in the region between kaon source and pion sink, showing two possible propagation paths: (a) the conventional path and (b) the around-the-world path. Δ denotes the source and sink separation and t denotes the time difference between the operator and kaon source. T denotes the lattice size in the time direction.

Thus we can obtain an estimate of $\langle 0|Q_\pm|K^0,\pi\rangle$ in the region when $\tau' < \frac{T}{2}$ by fitting the quantity:

$$\widetilde{C}^{Q_\pm}_{K,\pi\to 0}(\Delta, t = \Delta + t') \equiv \frac{N_\pi N_K C^{Q_\pm}_{K,\pi\to 0}(\Delta, t = \Delta + t')}{C^{\text{2pt}}_\pi(t') C^{\text{2pt}}_K(\Delta + t')} \tag{5.16}$$

to a constant.

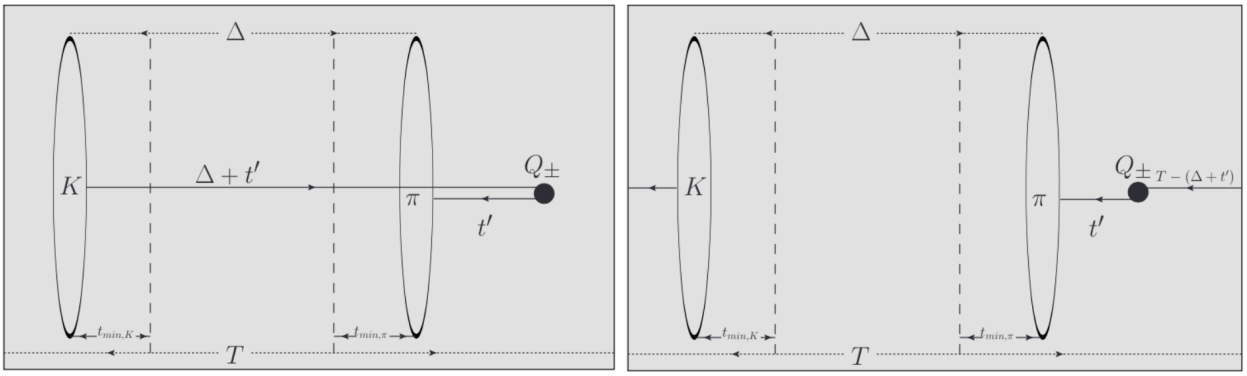

(a) (b)

Figure 5.2: $K \to \pi$ correlator when the operator is located outside the region between kaon source and pion sink, showing two possible propagation paths: (a) the conventional path and (b) the around-the-world path. Δ denotes the source and sink separation and t denotes the time difference between the operator and kaon source. T denotes the lattice size in the time direction.

We will estimate the magnitudes of the around-the-world effects in our three-point calculations. Details of the analysis of the around-the-world effects for the calculations on the $64^3 \times 128$ lattice ensemble will be discussed in Chapter 6.

5.3 Free-field verification of the four-point contractions in the local limit

A valuable test of our computational setup can be obtained by specializing to the case of no gauge field interactions and requiring that in the local limit(m_u and m_c large) our four-point contractions agree with the local Inami-Lim free field calculation.

As discussed in Chapter 2.2, we can calculate Δm_K from box diagrams with or without integrating out charm quarks. Starting from the box diagrams shown in Figures 5.3a and 5.3b, by integrating out the W bosons, we obtain the four-point diagrams shown in Figures 5.3c and 5.3d. If the inner quark loops are then integrated out, we obtain the three-point diagrams shown in Figures 5.3e and 5.3f.

In the QCD-free case, there is no strong coupling and thus we can calculate Δm_K in two equivalent ways:

- Apply the single-integration method to the four-point correlation functions.
- Extract the matrix element from the three-point correlation functions and multiply it with the Inami-Lim factor obtained from integrating out inner up and charm loops in the four-point diagrams.

Thus, if no extra factor is introduced in the relatively more complicated four-point calculation, we expect the same result from calculations performed both ways.

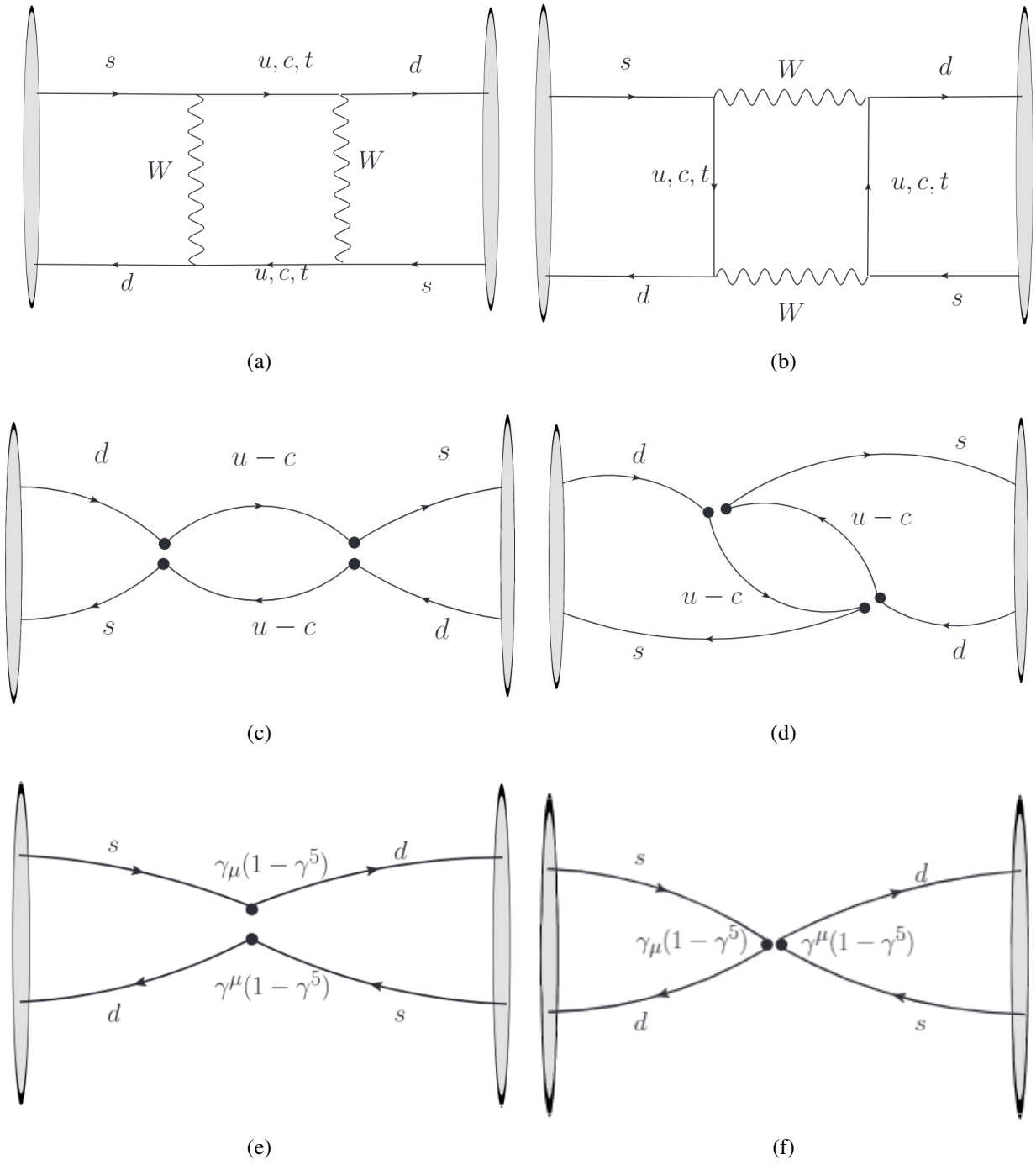

Figure 5.3: Diagrams related to QCD-free Δm_K calculation with different effective weak Hamiltonian.

5.3.1 Calculation with four-point correlation functions

As discussed in Section 3.1, Δm_K can be extracted from the single-integrated four-point correlation function $\mathcal{A}^S(T)$:

$$\Delta m_K^{\text{4pt}} = -2\frac{\lim_{T\to\infty}\mathcal{A}^s(T)}{N_K^2 e^{-m_K(t_f-t_i)}} = \frac{G_F^2}{2}\lambda_u^2\sum_{i,j=1,2}(-2)\times C_i^{lat}C_j^{lat}k_{ij}, \tag{5.17}$$

where C_i are Wilson coefficients, $\lambda_u = V_{ud}V_{us}^* = \cos\theta_c\sin\theta_c$ and k_{ij} is defined in Equation 4.24 in Section 4.1.4.

Based on Equation (XII.21) in [9], in the QCD-free case, we find the Wilson coefficients $C_\pm = 1$ in the effective Hamiltonian:

$$H_W = \frac{G_F}{\sqrt{2}}\sum_{q,q'=u,c}V_{qd}V_{q's}^*(C_+Q_+^{qq'} + C_-Q_-^{qq'}), \tag{5.18}$$

where $Q_\pm^{qq'} = \frac{1}{2}(Q_1^{qq'} \pm Q_2^{qq'})$. Equivalently, the Wilson coefficients for operators Q_1 and Q_2 are $C_1 = 0, C_2 = 1$. Thus we only need to calculate the two diagrams contracted from two Q_2 operators as shown in Figure 5.3c and 5.3d and the formula for Δm_K is simplified to be:

$$\Delta m_K^{\text{4pt}} = \frac{G_F^2}{2}\lambda_u^2\times(-2)\times C_2^{lat}C_2^{lat}k_{22} = \frac{G_F^2}{2}\lambda_u^2\times(-2)\times k_{22}. \tag{5.19}$$

5.3.2 Connection between the four-point and three-point diagrams

As we can see in Figure 5.4, for the QCD-free case, we could contract part of the two bilocal operators to form a inner loop and then integrate the inner loop appearing in the four-point diagrams in momentum space analytically and compare what we will call the "partially contracted" operator pair of two Q_2 operators with the local operator to obtain the factor related to the loop integral.

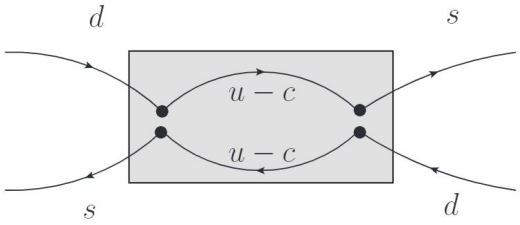

(a) Operator O^{4pt}, which is a partially contracted operator pair of two Q_2 operators.

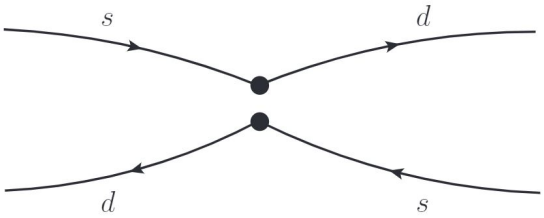

(b) local operator O_{LL}

Figure 5.4: The connection between O^{4pt}, the partially contracted operator pair of two Q_2 operators and the local operator O_{LL}.

Integrating the inner loop for two bi-local operator Q_2 gives:

$$O^{4pt} = -\frac{1}{2!}\frac{(2\pi)^4}{(2\pi)^8}\lambda_u^2(\frac{G_F}{\sqrt{2}})^2\int d^4k\Big[\bar{s}\gamma^\mu(1-\gamma_5)\not{k}\frac{m_c^2-m_u^2}{(m_c^2+k^2)(m_u^2+k^2)}\gamma^\nu(1-\gamma_5)d\Big]^2. \quad (5.20)$$

After integrating over the k^2, if we assume the ratio $\frac{m_u^2}{m_c^2}$ is small, we obtained the partially contracted operator :

$$O^{4pt} = \frac{N}{64}\frac{G_F^2}{\pi^2}\lambda_u^2 m_c^2[\bar{s}\gamma^\mu(1-\gamma_5)d[\bar{s}\gamma^\mu(1-\gamma_5)d], \quad (5.21)$$

where N is the factor relating the spinor product:

$$[\bar{s}\gamma^\mu(1-\gamma_5)\gamma^\alpha\gamma^\nu(1-\gamma_5)d][\bar{s}\gamma^\nu(1-\gamma_5)\gamma^\alpha\gamma^\mu(1-\gamma_5)d] \quad (5.22)$$

and local operator:

$$O_{LL} = [\bar{s}\gamma^\mu(1-\gamma_5)d][\bar{s}\gamma^\mu(1-\gamma_5)d], \quad (5.23)$$

where the matrix γ^α comes from the term $\not{k}$ which appears in the loop integral.

We find $N = 4$ and obtain the connection between the partially contracted parts of bi-local operators Q_2 and the local operator O_{LL}:

$$O^{4pt} = \frac{G_F^2}{16\pi^2}\lambda_u^2[\bar{s}\gamma^\mu(1-\gamma_5)d][\bar{s}\gamma^\mu(1-\gamma_5)d] = \frac{G_F^2}{16\pi^2}\lambda_u^2 m_c^2 O_{LL}. \quad (5.24)$$

This is consistent with Equation (XII.1) in [9] which uses the Inami-Lim function when $m_u = 0$ and $\frac{m_c}{m_W} \ll 1$.

If the up quark mass is not much smaller than the charm quark mass and the ratio $\frac{m_u^2}{m_c^2}$ is not small, the loop integral in 5.20 can be calculated as:

$$\mathcal{I}^{4\text{pt}} = \int_0^\infty dx \frac{(m_c^2 - m_u^2)^2 x^2}{(m_c^2 + x)^2 (m_u^2 + x)^2} = \frac{1 + 4\alpha^2 ln(\alpha) - \alpha^4}{1 - \alpha^2} m_c^2, \tag{5.25}$$

where $x = k^2$ and $\alpha = \frac{m_u}{m_c}$. This leads to a more useful connection formula between the local operator and the partially contracted bi-local operator pair:

$$O^{4\text{pt}} = \frac{G_F^2}{16\pi^2} \lambda_u^2 \mathcal{I}^{4pt} O_{LL} \tag{5.26}$$

The connection between local operator O_{LL} and bi-local operator pair of two Q_2 operators also leads to the connection between the four-point and the three-point diagrams we calculate in the QCD-free case. If the inner quark loop in the four-point diagram shown in Figure 5.3c is integrated out, we obtain the three-point diagram shown in Figure 5.3e multiplied by the factor $\mathcal{I}^{4pt}$. This is also valid for four-point diagram shown in Figure 5.3d and the three-point diagram shown in Figure 5.3f.

5.3.3 Calculation with three-point correlation functions

Based on Equations (XII.1-3) in [9] and using the normalization convention $\langle K^0(\vec{p_1}) | K^0(\vec{p_2}) \rangle = \delta^3(\vec{p_1} - \vec{p_2})$, we obtain the formula of Δm_K calculated from three-point correlation functions:

$$\Delta m_K^{3\text{pt}} = \frac{G_F^2}{8\pi^2} M_W^2 \lambda_c^2 \frac{m_c^2}{M_W^2} \langle \overline{K^0} | O_{LL} | K^0 \rangle, \tag{5.27}$$

where O_{LL} is given in Equation 5.23, and the approximated Inami-Lim functions $S(x_u) = 0$, $S(x_c) \doteq x_c \equiv \frac{m_c^2}{M_W^2}$ are used. If the up quark mass is not neglected, according to the analysis in

Section 5.3.2, Δm_K calculated from three-point correlation functions is given by:

$$\Delta m_K^{3\text{pt}} = \frac{G_F^2}{8\pi^2}\lambda_c^2 \mathcal{I}^{4\text{pt}} \langle \overline{K^0} | O_{LL} | K^0 \rangle, \tag{5.28}$$

where $\mathcal{I}^{4\text{pt}}$ is defined in Equation 5.25. The matrix element $\langle \overline{K^0} | O_{LL} | K^0 \rangle$ can be extracted from the three-point diagrams shown in Figure 5.3e and 5.3f.

We can compare the contributions to Δm_K from each four-point diagram and its corresponding three-point diagram and expect consistent results. In our comparison, we choose to compare the contribution from the four-point diagram (c) and the three-point diagram (e) in Figure 5.3. Therefore we would like to calculate two quantities:

$$\Delta m_K^{4\text{pt}'} = \frac{G_F^2}{2}\lambda_u^2 \times (-2) \times C_2^{lat} C_2^{lat} k'_{22} = \frac{G_F^2}{2}\lambda_u^2 \times (-2) \times k'_{22}, \tag{5.29}$$

and

$$\Delta m_K^{3\text{pt}'} = \frac{G_F^2}{8\pi^2}\lambda_c^2 \mathcal{I}^{4\text{pt}} \langle \bar{K}^0 | O_{LL} | K^0 \rangle', \tag{5.30}$$

where the prime indicates the contributions from only the specific contractions shown in (c) and (e) of Figure 5.3. Similar to the QCD calculation, we can create free quark propagators, contract the propagators and fit the correlation functions to extract quantities like the normalization factors of the meson operators and the masses which determine the time dependence of the three- and four-point correlators. Thus, we will compare these free-field four- and three-point functions by examining them in nearly the same way as is done for similar quantities in an interacting theory.

5.3.4 Comparison between BG/Q supercomupter and analytic calculation

Firstly, the free-field calculation is performed on the BG/Q supercompter using a $64^3 \times 128$ lattice. The lattice size we can use for the comparison is limited by the computational power and a $64^3 \times 128$ lattice is the largest size feasible. However, we may need a larger lattice to do the calculation with smaller finite lattice spacing errors and around-the-world effects. An alternative approach is to use the analytic expression for the free-field domain wall fermion propagators. Thus,

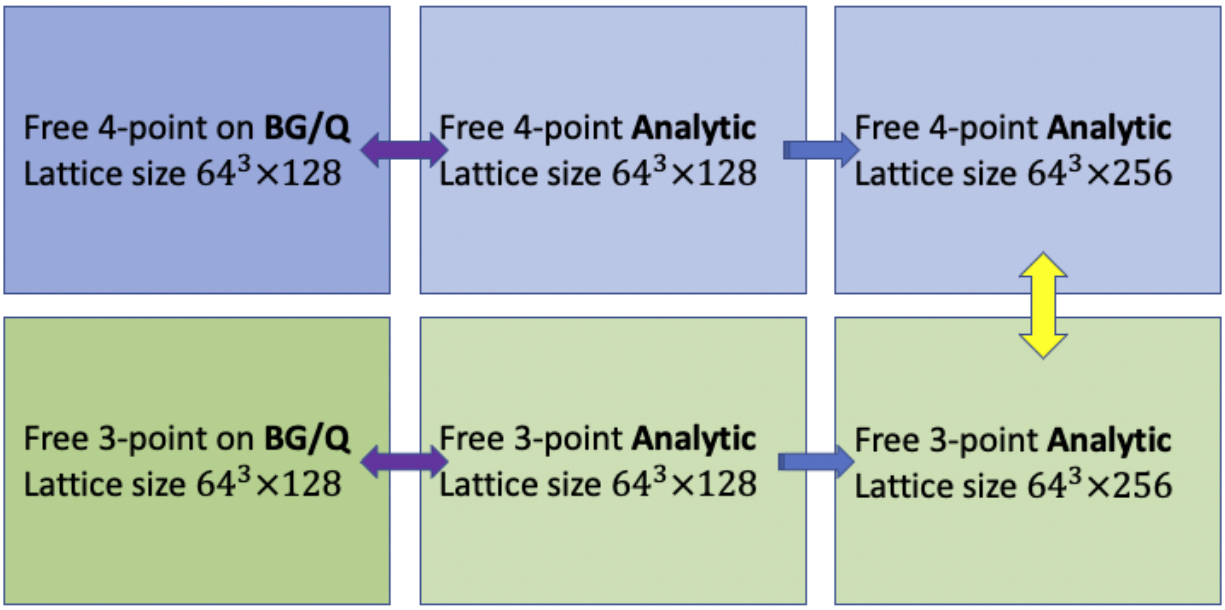

Figure 5.5: The relationship between the BG/Q and our analytic free-field calculations. The yellow double-arrow represents the comparison between four- and three-point results. The purple double-arrow represents the comparison between BG/Q and analytic results. The blue single arrow represents the extended calculation using analytic expressions.

we first confirm the consistency between the BG/Q results and the analytic results, on this smaller lattice, and then focus on the analytic comparison with larger lattice. This sequence of comparisons is shown in Figure 5.5.

Some key quantities obtained from BG/Q supercomputer and analytic calculations are compared by taking their ratios and the results of these comparisons are shown in Table 5.2. For the two-point correlation functions $G^{2\text{pt}}(t)$ calculated in both ways, we take their ratios for all allowed values of time separation t. The averages of these ratios for all t are listed in the column labeled by "Ratio AVE" and the differences of the ratios are estimated by the standard deviations listed in the column labeled by "Ratio STD" and the largest discrepancies from 1 among the ratios are listed in the column labeled by "Max Ratio Discrepancy". For the three-point calculations, we compare the extracted matrix elements $\langle \overline{K^0} | O_{LL} | K^0 \rangle$. For the four-point calculations, we compare the four-point correlation function $G(\Delta, t_x, t_y)$ for all allowed t_x and t_y within the integration box of size $T = 10$.

The consistency is confirmed by the ratios having values close to 1 with minor discrepancies from the numerical precision and finite lattice size in the fifth dimension.

Quantity	Ratio AVE	Ratio STD	Max Ratio Discrepancy
Pion Corr.	1.0000	4.68×10^{-4}	4.5×10^{-3}
Kaon Corr.	1.0000	4.90×10^{-4}	4.8×10^{-3}
$\langle \overline{K^0} \vert O_{LL} \vert K^0 \rangle$	1.0000	4.90×10^{-4}	1.0×10^{-3}
Diagram (c) in Fig. 5.3	1.0000	5.77×10^{-4}	1.3×10^{-3}

Table 5.2: Ratios of the quantities obtained from BG/Q numerical calculations and analytic calculations. The lattice size is $64^3 \times 128$ and $m_c = 0.15$.

5.3.5 Results

In order to insure that the inner quark loop in the four-point calculation is local compared to the distance scale that characterizes the external quark lines, we choose to have the masses of down and strange quark light while the masses of up and charm quark appearing in the inner loop heavy. For our choices, shown in Table 5.3, the up quark is not much lighter than the charm quark and the three-point results should be obtained using Equation 5.30. We perform comparisons with different charm masses and the input parameters are shown in Table 5.3.

We then obtain the unintegrated correlators which are plotted in Figure 5.6 and 5.7 and integrate them over all the allowed values of δ, which is the time separation between the two bi-local operators.

Lattice size	m_d	m_s	m_u	m_c	$\Delta m_K^{4\text{pt}'}/\Delta m_K^{3\text{pt}'}$ ratio
$64^3 \times 256$	0.03	0.03	0.1125	0.15	0.9713
$64^3 \times 256$	0.03	0.03	0.1125	0.25	0.9584

Table 5.3: The input parameters used in the QCD-free analytic calculation and the $\Delta m_K^{4\text{pt}'}/\Delta m_K^{3\text{pt}'}$ ratios at $T = 30$ are included.

As shown in Figures 5.8 and 5.9, as the integration upper limit T is increasing, the ratio between the four- and three-point results approaches a constant close to 1 for each value of m_c.

The ratios between the four-point and three-point results for a large value of T are shown in Table 5.3. With the ratios only deviating from 1 only by a few percents, which is consistent with

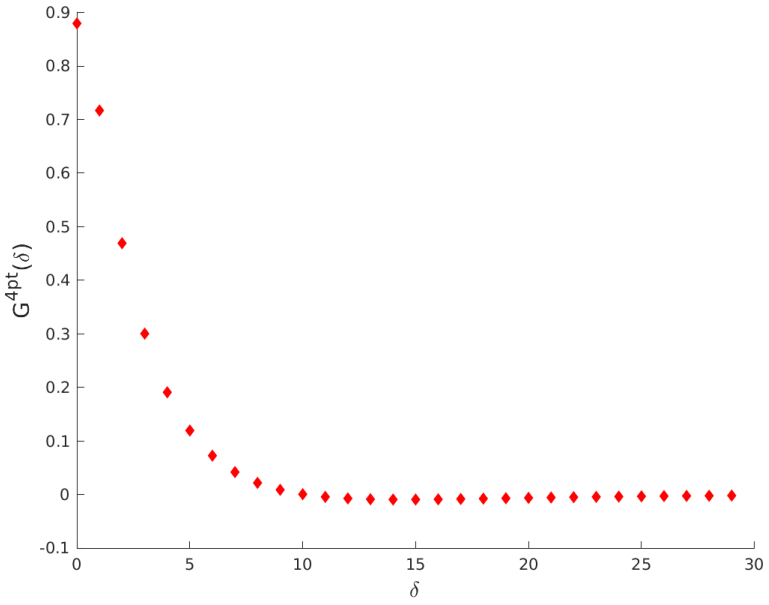

Figure 5.6: The unintegrated four-point correlator plotted as a function of δ. $m_c = 0.15$, with other quarks masses shown in Table 5.3.

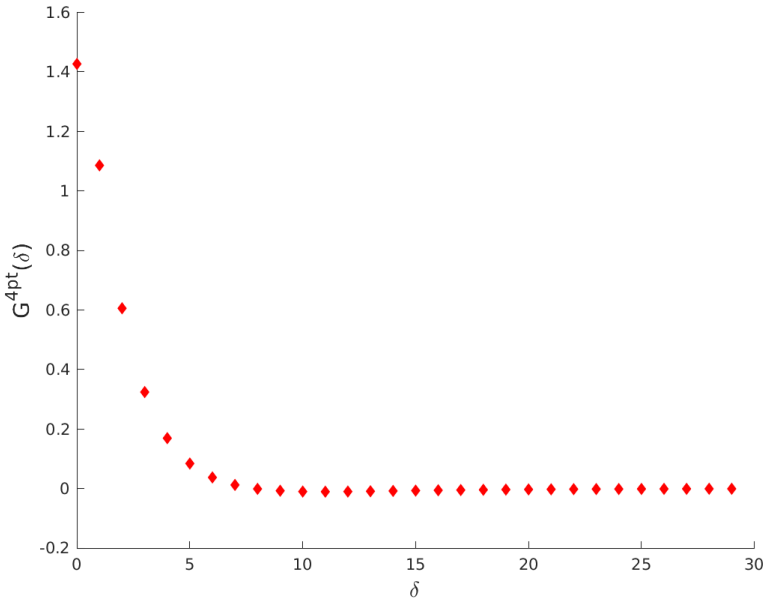

Figure 5.7: The unintegrated four-point correlator plotted as a function of δ. $m_c = 0.25$, with other quarks masses shown in Table 5.3.

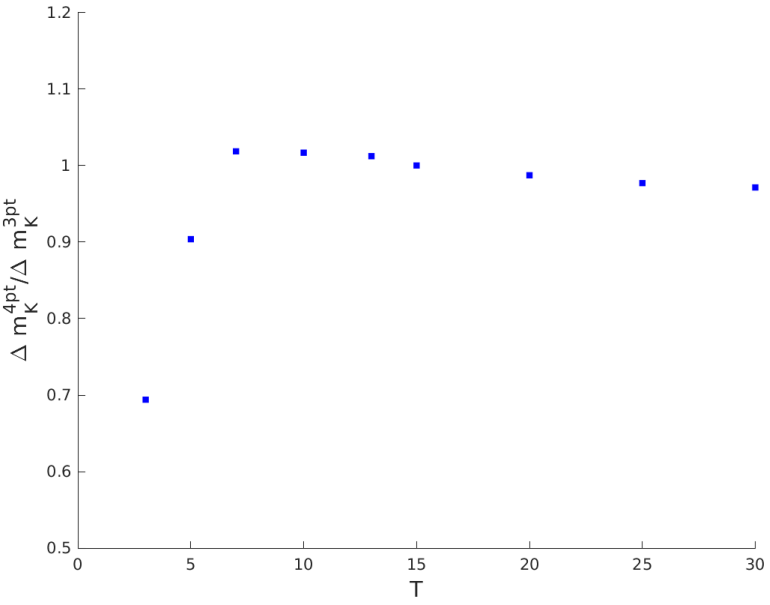

Figure 5.8: The ratio between the four-point and three-point results plotted as a function of the integration upper limit T with $m_c = 0.15$.

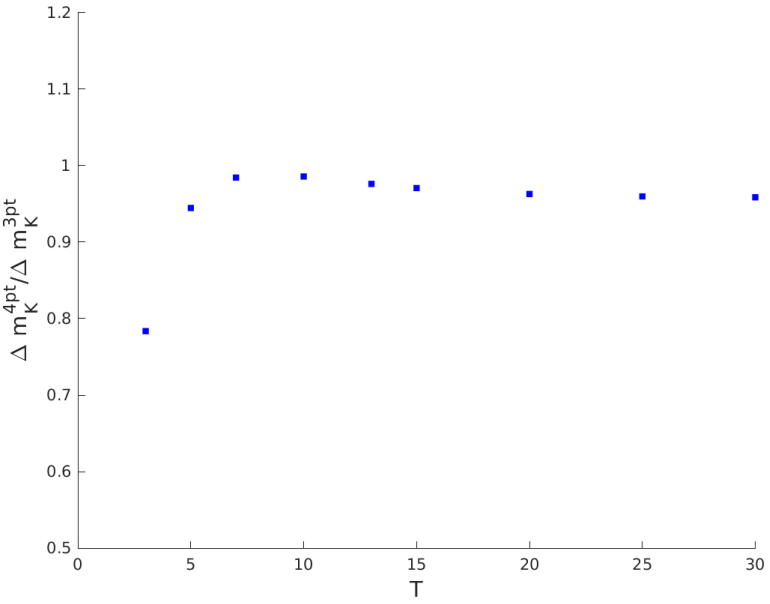

Figure 5.9: The ratio between the four-point and three-point results plotted as a function of the integration upper limit T with $m_c = 0.25$.

the uncertainty from finite volume effects, we conclude that using the analytic method, which is verified to be equivalent to BG/Q numerical calculation in the free-field case, the contraction results of four-point diagrams agree with the results of the Inami-Lim calculation when m_c and m_u are massive.

5.4 Consistency of NPR factors used for Δm_K with other published NPR values

It is important to compare the NPR factors that we use in this thesis with published values where possible. However, the published NPR factors are calculated under $SU(3) \times SU(3)$ flavor symmetry while our NPR is performed under $SU(4) \times SU(4)$ flavor symmetry. We need to identify those NPR factors which are common to both cases.

The sum of matrix elements $Z_+ = Z_{11} + Z_{12}$ in our Δm_K NPR corresponds to the renormalization of the Q_+ operator which belongs to the $(84, 1)$ irreducible representation of $SU(4) \times SU(4)$. As discussed in Section 3.4.1, an operator belonging to the $(84, 1)$ representation has a tensor of coefficients which is traceless and symmetric under permutations of upper and lower indices. In the case of $SU(3) \times SU(3)$ flavor symmetry, an operator belonging to the $(27, 1)$ irreducible representation, also has a tensor of coefficients which is traceless and symmetric under permutations of these indices. Consequently, this $(27, 1)$ $SU(3) \times SU(3)$ operator also belongs to the (84,1) representation and will have the same renormalization factor as that for operators which belong to the $(84, 1)$ representation.

The previously calculated Δm_K NPR factors[6] on the 24I lattice ensemble in the $(\gamma_\mu, \not{q})$ scheme at a scale $\mu = 2.15$ GeV can be compared with an earlier published $Z_{(27,1)}^{(\gamma_\mu, \not{q})}$ value [22]. The numbers can be found in Table 5.4 and we can verify that $Z_{(84,1)} = Z_{11} + Z_{12} = Z_{(27,1)}$.

$Z_{11} = Z_{22}$	$Z_{12} = Z_{21}$	$Z_{11} + Z_{12}$	$Z_{\text{raw}}^{lat \to RI} / Z_q^2$	$Z_q^{\not{q}}$	$Z_{(27,1)}$
0.5916	-0.05901	**0.5326**	0.825(7)	0.8016(3)	**0.5301(48)**

Table 5.4: The Wilson coefficients from Δm_K NPR[6](left half) and from Table VII of [22] at a scale $\mu = 2.15$ GeV.

In addition, we have a previously published NPR factor Z_{B_K} for the quantity B_K[12] which is

given by:

$$Z_{B_K}^{(A,B)} = \frac{Z_{(27,1)}^{(A,B)}}{Z_A^2}, \tag{5.31}$$

where Z_A can be calculated from $\Lambda_{A/V}$ and Z_q as defined in Equations 3.100 and 3.101. Here the label A denotes the type of projectors which defines the renormalization scheme and B denotes the scheme in which quark fields are renormalized.

As shown in Table 5.5, on the 32I lattice, we can use our Δm_K NPR factor, $Z_{(84,1)}^{(\gamma_\mu,\gamma_\mu)} = Z_{11} + Z_{12}$ calculated at a scale $\mu = 3.00$ GeV and Z_A from [12] to obtain a Z_{B_K} value consistent with the published Z_{B_K} value in [12].

$Z_{(84,1)}^{(\gamma_\mu,\gamma_\mu)}$	Z_A	Z_{B_K} from Δm_K NPR	Z_{B_K} in [23]
0.5195(2)	0.7447(1)	**0.9368(6)**	**0.9396(2)**

Table 5.5: The NPR factor $Z^{\text{lat}\to\text{RI}}$ obtained in a Δm_K calculation which together with Z_A from [12] gives the value for Z_{B_K} shown in the third column which can be compared with the results for Z_{B_K} from Table XIX in [23] (right half) at a scale $\mu = 3.00$ GeV, for (γ_μ, γ_μ) scheme.

5.5 Finite lattice spacing effects

5.5.1 Elimination of $O(a)$ finite lattice spacing errors

Because we are using chiral fermions, we expect only $O(a^2)$ finite lattice spacing errors. However, on the lattice, when a time integral is replaced by a sum over time slices, this may introduce finite lattice spacing errors $\sim O(a)$. In the double-integration method, it can be demonstrated that this effect is eliminated by the symmetry of the integration. In our single-integration method, after the exponentially growing contribution from states with $E_n < m_K$ has been removed the resulting unintegrated correlator vanishes near the integration limits, so that any $O(a)$ contribution is suppressed.

5.5.2 Sources of $O(a^2)$ finite lattice spacing errors

After eliminating the $O(a)$ finite lattice spacing errors, we have to estimate the remaining $O(a^2)$ finite lattice spacing errors. The first possible source is associated with the heavy charm quark we have included in our lattice calculation. The effect should be proportional to the dimensionless quantity $(m_c a)^2$. Determination of the size of this term will allow us to estimate its contribution to our systematic error.

5.6 Scaling test on lattices with different lattice spacings

A scaling test, in which we measure the same physical quantities on several lattices with different lattice spacings, can help us determine the size of the $O(a^2)$ finite lattice spacing error and give an estimate of how large these effects are.

Thus, in order to estimate the finite lattice spacing errors for our Δm_K calculation, we perform scaling tests focusing on the matrix elements obtained from three-point correlation functions and four-point integrated correlators using two different lattice spacings. It's economical to start with a smaller lattice where the relatively large $m_c a$ value is examined. We perform the scaling tests on the 24I and 32I ensembles and details about these two lattices are listed in Table 3.1.

To obtain the input valence quark masses for the two ensembles which result in meson masses on the two lattices which are consistent, we first set the physical values of meson masses to be the ones obtained from the calculation on the 32IF ensemble using its unitary quark masses. Then based on several meson masses obtained on the 24I and 32I ensembles for various valence quark masses[12], we perform interpolations to obtain the valence quark masses which yield physical meson masses consistent with the 32IF meson masses described above using formulas from chiral effective theory. The calculated valence quark masses and the expected meson masses are shown in Table 5.6.

Lattice	m_x	m_y	$m_{\pi,\text{pre}}a$	$m_{\pi,\text{pre}}$/MeV	$m_{K,\text{pre}}a$	$m_{K,\text{pre}}$/MeV	$m_c a$
24I	0.00667	0.0321	0.2079	371.15	0.3125	557.83	0.15:0.05:0.35
32I	0.00649	0.0249	0.1557	371.15	0.2332	557.83	$(0.15{:}0.05{:}0.35)\frac{1.785}{2.383}$
Lattice	$m_{x,\text{uni}}$	$m_{y,\text{uni}}$	$m_{\pi,\text{uni}}a$	$m_{\pi,\text{uni}}$/MeV	$m_{K,\text{uni}}a$	$m_{K,\text{uni}}$/MeV	$m_c a$
32IF	0.0047	0.0186	0.1179	371.15	0.1772	557.83	-

Table 5.6: Parameters related to the lattices for measurements. m_x is the valence mass for light quarks: up and down. m_y is the valence mass for strange quark. The predicted pion mass $m_{\pi,\text{pre}}$ and the predicted kaon mass $m_{K,\text{pre}}$ are displayed both in lattice units and in physical units.

5.6.1 Results from two-point functions

As discussed in Section 4.1, we can obtain meson masses from two-point correlation functions. We expect our input valence quark masses to produce mesons with equal physical masses on the two different lattices. The results listed in Table 5.7 and Table 5.8 verify that not only light mesons like pion and kaon, but also heavy charmed mesons with relatively large values of m_c, have consistent masses. We can therefore conclude the quantities we have calculated on these two ensembles with different lattice spacings are consistent in physics.

Lattice	N_{conf}	m_π/MeV	$m_\pi a$	$m_{\pi,\text{pre}}a$	m_K/MeV	$m_K a$	$m_{K,pre}a$
24I	186	371.3(7)	0.2080(4)	0.2079	556.2(7)	0.3116(4)	0.3125
32I	222	371.4(6)	0.1558(2)	0.1557	557.5(6)	0.2340(3)	0.2332

Table 5.7: The light meson masses resulting from light and heavy quark masses obtained from interpolation calculations on the 32I and 24I ensembles.

m_c 24I	m_c/GeV 24I	m_c^R/GeV 24I	m_D 24I/GeV	m_c 32I	m_c/GeV 32I	m_c^R/GeV 32I	m_D 32I/GeV
0.15	0.26775	0.4079	1.0891(27)	0.11	0.26775	0.4068	1.1151(9)
0.20	0.357	0.5439	1.2599(31)	0.15	0.357	0.5423	1.2940(10)
0.25	0.44625	0.6799	1.4142(37)	0.19	0.44625	0.6779	1.4563(11)
0.30	0.5355	0.8158	1.5550(43)	0.22	0.5355	0.8135	1.6057(11)
0.35	0.62475	0.9518	1.6836(50)	0.26	0.62475	0.9491	1.7442(12)

Table 5.8: m_c masses and corresponding D meson mass m_D for the 24I and 32I ensembles, with renormalized masses using mass renormalization factors $Z^\gamma_{m,24\text{I}} = 1.5235(13)$ and $Z^\gamma_{m,32\text{I}} = 1.5192(39)$[12].

.

5.6.2 Scaling of three-point matrix elements

We can then examine how the matrix elements extracted from three-point functions scale on these lattice ensembles. The three-point diagrams which contribute to $\langle \pi | Q_i | K^0 \rangle$ matrix elements are shown in Figure 5.10. Compared to the eye diagrams shown in Figures 5.10c and 5.10d having self-loop parts, the figure-8 diagrams shown in Figures 5.10a and 5.10b have relatively low statistical errors and don't involve the heavy charm quark which is the most probable source of large discretization error.

If we can compare the results for only the contribution of the figure-8 diagrams to these three-point functions, we can test the scaling violation with high precision. To perform such scaling violation tests on the three-point functions and also on the four-point functions which we will present later, we have to establish that the set of diagrams we are studying is a well-defined portion of the full physical amplitude by itself and have a continuum limit as the lattice spacing a approaches 0. We would expect that the difference between such a diagram and its continuum limit can be described by ca^2 where c is approximately a constant and the possible logarithmic corrections to the ca^2 behavior is neglected.

Here for the case of the contribution of figure-8 diagrams to these three-point functions, we can justify our comparison by creating an alternative interpretation for the process being studied. If we view the transition being computed as $K \to D$ in an unphysical four-quark theory in which the charm quark is degenerate with the light up and down quarks, the eye-diagrams containing the $(u - c)$ self loops vanish and we can interpret the figure-8 diagrams as the only diagrams that would contribute, provided we neglect the 1% effects arising from our failure to match the sea quark masses on the 24I and 32I ensembles. Thus, if we further make sure that both the three-point function and the corresponding NPR factors are being calculated consistently in this partially quenched four/three-quark theory, we can expect that the figure-8 diagrams alone have a meaningful scaling limit with the finite lattice spacing error behaving as ca^2.

However, the above argument is limited to the figure-8 diagrams. We can also make a more direct argument for a collection of diagrams to be studied in isolation in a lattice calculation which

is more generic and applies to both figure-8 diagrams and four-point connected-only diagrams that we will present later, based on a lower-level understanding of renormalization and the continuum limit. Like the current case of the figure-8 diagrams, within a natural collection of the diagrams, the diagrams have fermion propagators contracted with a fixed topology. At the same time, for a lattice calculation with a specific contraction of quark propagators, the path integral provides a sum over all possible gluon emissions, gluon self-interactions and closed fermion loop insertions. For such a specific quark propagator topology, provided the quark propagator topology does not introduce new divergent sub-diagrams not present in QCD, the renormalizability and chiral symmetry of DWF QCD will lead to a continuum limit with a ca^2 scaling behavior. However, even if new divergent sub-diagrams do appear, such as the vertex correction arising from the exchange of a gluon between two of the legs of a four-quark vertex resulting from an insertion of H_W, provided that we have included these same diagrams when performing the NPR subtractions, we can still obtain a well-defined collection of diagrams having a continuum limit with a ca^2 scaling behavior.

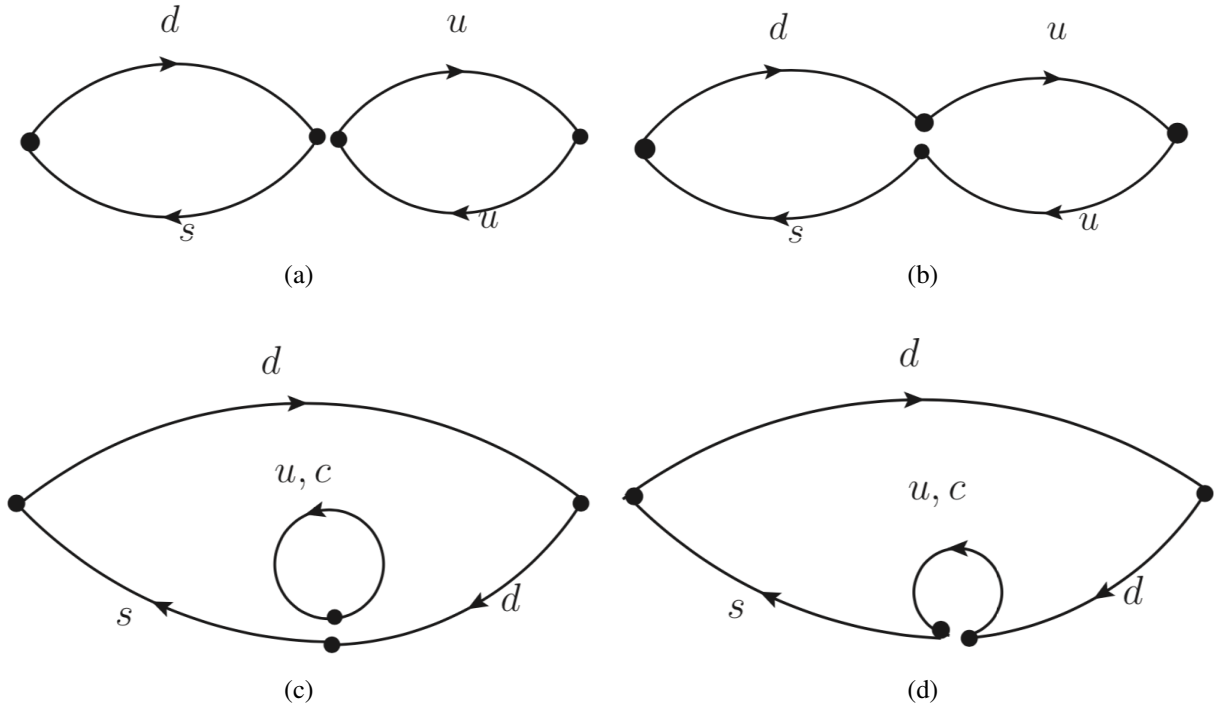

Figure 5.10: K to π diagrams. The upper two are figure-8 diagrams contracted with operator Q_1 (a) and Q_2 (b). The lower two are eye diagrams contracted with operator Q_1 (c) and Q_2 (d).

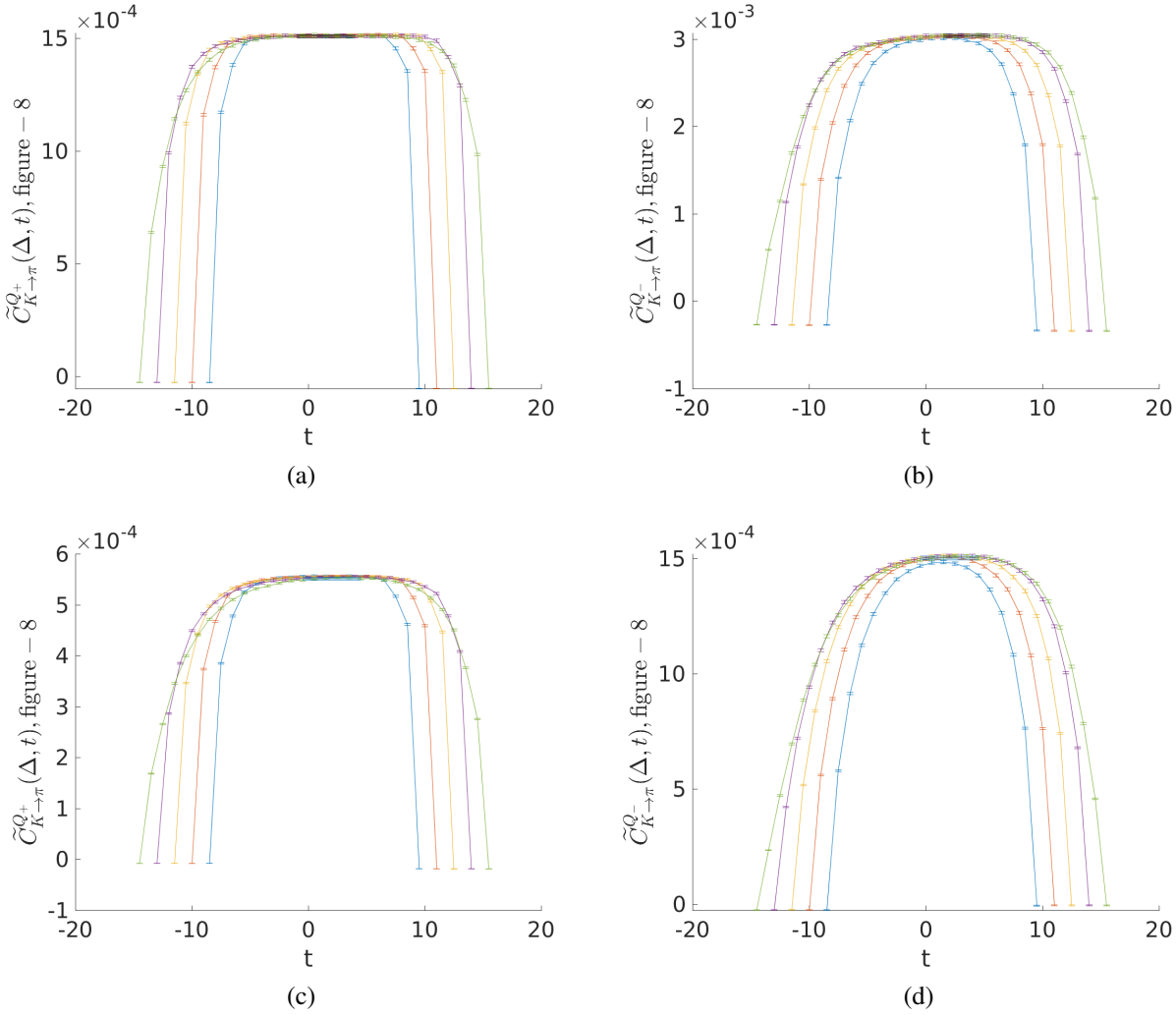

Figure 5.11: The three-point correlation functions $\widetilde{C}^{Q_+}_{K\to\pi}(\Delta,t)$ and $\widetilde{C}^{Q_-}_{K\to\pi}(\Delta,t)$ calculated from figure-8 diagrams plotted as functions of t, the time of the operator. The kaon source is at the time of the first data point on the left on each curve. The upper two plots are results from the 24I ensemble. The lower two plots are results from the 32I ensemble. We use $N_{\text{sep}} = 5$ source-sink separations shown in Table 5.9. The values of $\langle\pi|Q_+|K^0\rangle$ and $\langle\pi|Q_-|K^0\rangle$ are obtained from the fitting of plateaus. The mean values and errors from uncorrelated fits are plotted as three straight lines within the fitting range.

Based on the relationship $Q_\pm = (Q_1 \pm Q_2)$, we can easily obtain the matrix elements $\langle\pi|Q_\pm|K^0\rangle$ from linear combinations of results from Q_i operators. In Figure 5.11, we plot the three-point correlation functions $\widetilde{C}^{Q_\pm}_{K\to\pi}(\Delta, t)$ calculated from figure-8 diagrams by which we have divide the time dependence according to Equation 4.8 with the source-sink separations listed in Table 5.9. For each case, as the source-sink separation becomes larger and the effects from the excited states become negligible, a plateau region near the middle of the curve appears. We fit each three-point function in the plateau region to a constant and obtain the contribution from the figure-8 diagrams to the three-point matrix elements. The plateaus also indicate that correlation functions calculated from the figure-8 diagrams alone have the same expected physical time dependence.

N_{sep}	Δ_{min}	Δ_{max}	Δ_{step}
5	18	30	3

Table 5.9: Multiple source-sink separations used in the plots of the three-point correlation functions on the 24I and 32I ensembles, shown in Figure 5.11.

μ/GeV	Irrep	Z factors		Matrix elements in physical Unit		Scaling violation
		32I	24I	32I	24I	
		(a^{-1} =2.38GeV)	(a^{-1} =1.78GeV)	(a^{-1} =2.38GeV)	(a^{-1} =1.78GeV)	
2.15	(84,1)	0.52997(11)	0.47143(8)	0.003957(18)	0.004045(18)	-2.19 %
	(20,1)	0.58755(14)	0.57493(26)	0.011949(65)	0.009936(59)	18.39 %
2.64	(84,1)	0.52489(6)	0.46996(6)	0.003919(18)	0.004032(18)	-2.84 %
	(20,1)	0.60358(11)	0.58239(11)	0.012275(67)	0.010065(60)	19.78 %

Table 5.10: The Z factors of NPR in (γ_μ, γ_μ) scheme and $\langle\pi|Q_\pm|K^0\rangle$(figure-8 only) in physical units on the two lattice ensembles and different scale μ. The relative scaling violations are listed in the last column.

μ/GeV	Irrep	Z factors		Matrix elements in physical Unit		Scaling violation
		32I	24I	32I	24I	
		(a^{-1} =2.38GeV)	(a^{-1} =1.78GeV)	(a^{-1} =2.38GeV)	(a^{-1} =1.78GeV)	
2.15	(84,1)	0.60490(35)	0.55073(40)	0.004516(21)	0.004725(22)	-4.51%
	(20,1)	0.67062(61)	0.67164(46)	0.013638(74)	0.011608(69)	16.08%
2.64	(84,1)	0.58968(16)	0.53025(13)	0.004403(20)	0.004549(21)	-3.27%
	(20,1)	0.67807(31)	0.65711(32)	0.013790(75)	0.011357(68)	19.35%

Table 5.11: The Z factors of NPR in $(\gamma_\mu, \not{q})$ scheme and $\langle\pi|Q_\pm|K^0\rangle$(figure-8 only) in physical units on the two lattice ensembles and different scale μ. The relative scaling violations are listed in the last column.

The results for these figure-8 diagrams are listed in Table 5.10 and Table 5.11 at $\mu = 2.15$ GeV

and $\mu = 2.64$ GeV. The figure-8 matrix element of the operator Q_+ which belongs to the (84,1) representation has a small scaling violation of size $\sim 2-4\%$, while the figure-8 matrix element of the operator Q_- which belongs to the (20,1) representation has a large scaling violation of size $\sim 20\%$.

Even in the absence of a heavy charm quarks, such an unexpectedly large scaling violation as appears in the matrix element of Q_- operator is not unique. As shown in our previously published paper[24], $K \to \pi\pi$ matrix elements calculated from operators belonging to the (8,8) irreducible representation also show similarly large finite lattice spacing errors as shown in Table XIV of Reference [24].

5.6.3 Scaling of four-point single-integrated correlation functions

Similar to the three-point scaling tests, we perform a series of scaling tests for the contribution from four-point diagrams of type 1 and type 2, which are all connected. We also need to calculate three-point matrix elements $\langle\pi|Q_\pm^{lat}|K^0\rangle$ to remove the exponentially increasing terms from the single-integrated four-point correlators.

In this case, only connected diagrams are calculated, and only up quark can appear in our intermediate states. When we calculate the three-point matrix elements $\langle\pi|Q_\pm^{lat}|K^0\rangle$, we must use the interpolating operator $O_{\pi^0} = i\overline{u}\gamma_5 u$ rather than $O_{\pi^0} = i(\overline{u}\gamma_5 u - \overline{d}\gamma_5 d)/\sqrt{2}$ and only include figure-8 diagrams shown in Figures 5.10a and 5.10b since without disconnected diagrams the combination $\overline{u}\gamma_5 u$ and $\overline{d}\gamma_5 d$ behave as independent degenerate mesons[6].

We perform the scaling tests on the single-integrated four-point correlation functions. For the relatively light input charm masses used here, the correlation function is highly non-local and limited by the lattice size, we can not use a sufficiently large T to extract Δm_K from the single integration as discussed in Section 3.1. However, because the single-integrated correlator itself is a physical quantity with a continuum limit, we can perform the scaling tests on the single-integrated four-point correlators for the operators $Q_\pm$ if we use consistent physical integration ranges on the two different lattices.

In Figure 5.12, we plot the unintegrated correlators with two Q_+ operators for various m_c values which yield equal D meson masses on the 24I and 32I ensembles. We find the unintegrated correlators on the 24I and 32I ensembles almost overlap with each other and have no significant scaling violations.

The red dashed line represents the cutoff value for the single-integration on the 32I ensemble and the black line represents the cutoff value for the single-integration on the 24I ensemble. To remove the $O(a)$ errors from difference in the integration range for the single integration, we perform interpolations on the 24I ensemble to match the integration cutoff value on the 32I ensemble, which is $T_{\text{cut}} = 5.87\ \text{GeV}^{-1}$ and evaluate the integral using the trapezoidal rule.

The single-integrated correlators with two Q_+ operators and a fixed integration cutoff $T_{\text{cut}} = 5.87\ \text{GeV}^{-1}$ are plotted as a function of D meson mass in Figures 5.13a and 5.13b. We take the ratios between the results on the two lattices with the same D meson masses in physical units for various charm masses. If the charm quark is the dominating source of scaling violation, as we reduce the charm mass, the ratio between different lattice spacing should approach 1. This can be verified in Figure 5.13c. On the 64I ensemble, the $m_c a = 0.32 \sim 0.33$ gives the physical D meson masses. To estimate the finite lattice spacing effect for our lattice calculation on the 64I ensemble, we mark the point where $m_c a = 0.32$ on the coarser 24I ensemble and find the scaling violation is about 5%.

Similarly, in Figure 5.14, we plot the unintegrated correlators with two Q_- operators for various m_c values which yield consistent D meson masses on the 24I and 32I ensembles. In contrast to the case with two Q_+ operators, we find the unintegrated correlators with two Q_- operators on the 24I and 32I ensembles have significant scaling violations. In Figures 5.15a and 5.15b, we plot the single-integrated correlators with two Q_- operators on the 24I and 32I ensembles. In Figure 5.15c, we plot the ratios between the results on the two lattices as a function of physical D meson mass. The scaling violation at $m_c a = 0.32$ is about 14%. However, we find the ratio for the case with two Q_- operators is not approaching 1 as the charm mass becomes smaller but instead approaching a ratio which is about 1.4. This indicates that in addition to the scaling violation introduced by

the heavy charm quark, the scaling error for the four-point integrated correlators with two Q_- operators, can be as large as 40%.

In our Δm_K calculation, we have combinations of four-point correlation functions with Q_+ and Q_- operators. Based on the scaling tests performed on the 24I and 32I ensembles, we estimate the finite lattice spacing error to be of order of 40%.

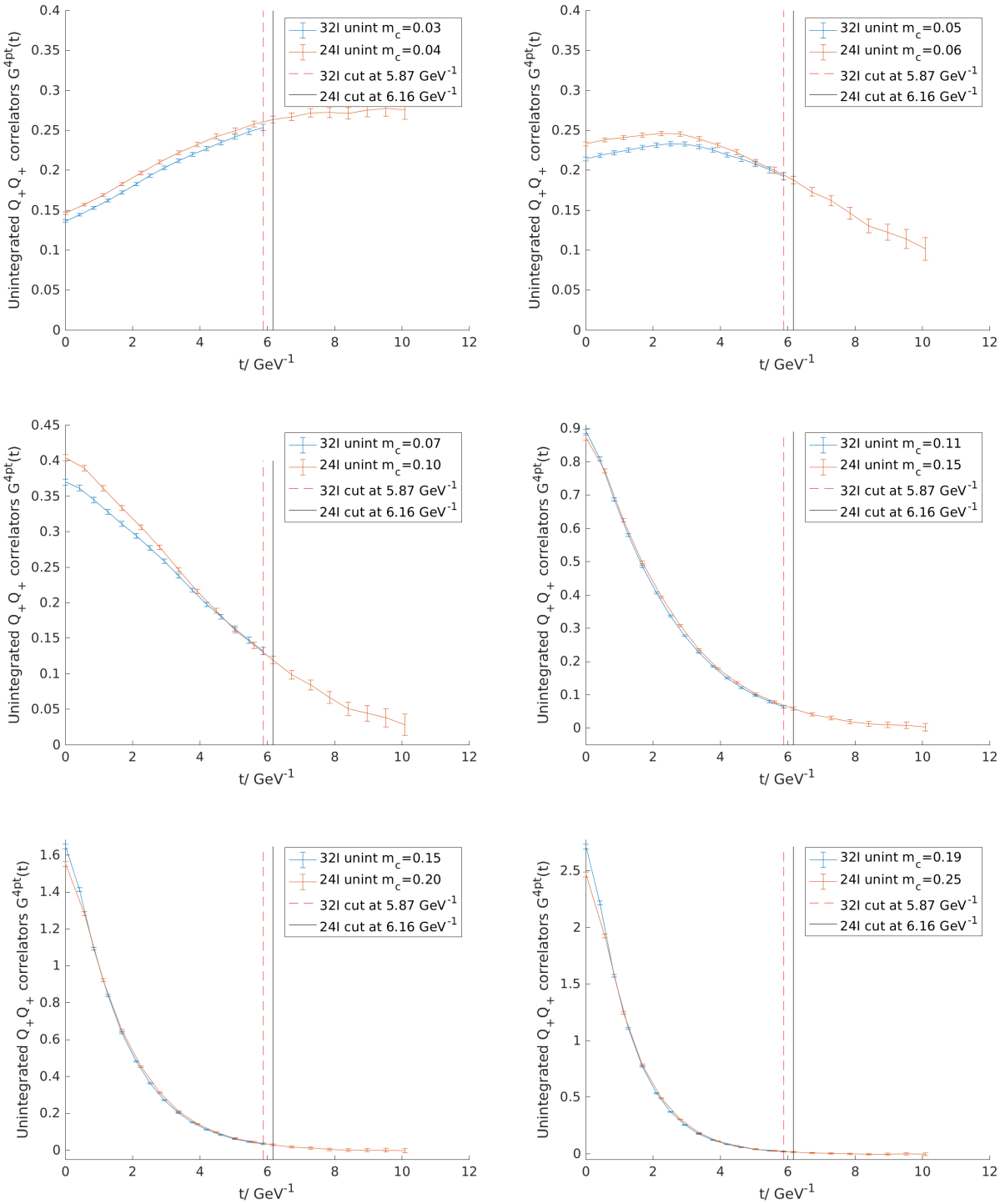

Figure 5.12: The 32I and 24I unintegrated correlators with two Q_+ operators at same physical D meson masses. The vertical lines are the cutoff physical time for the single-integration and an additional interpolation is performed to remove the $O(a)$ errors due to the difference of the integration range.

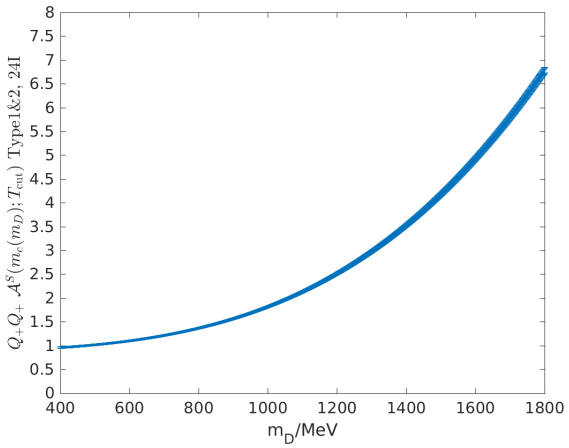

(a)

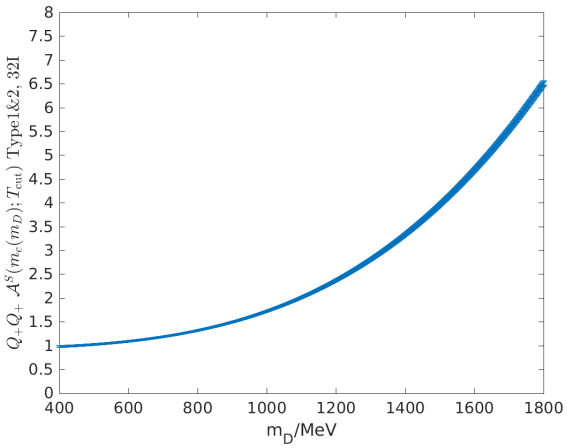

(b)

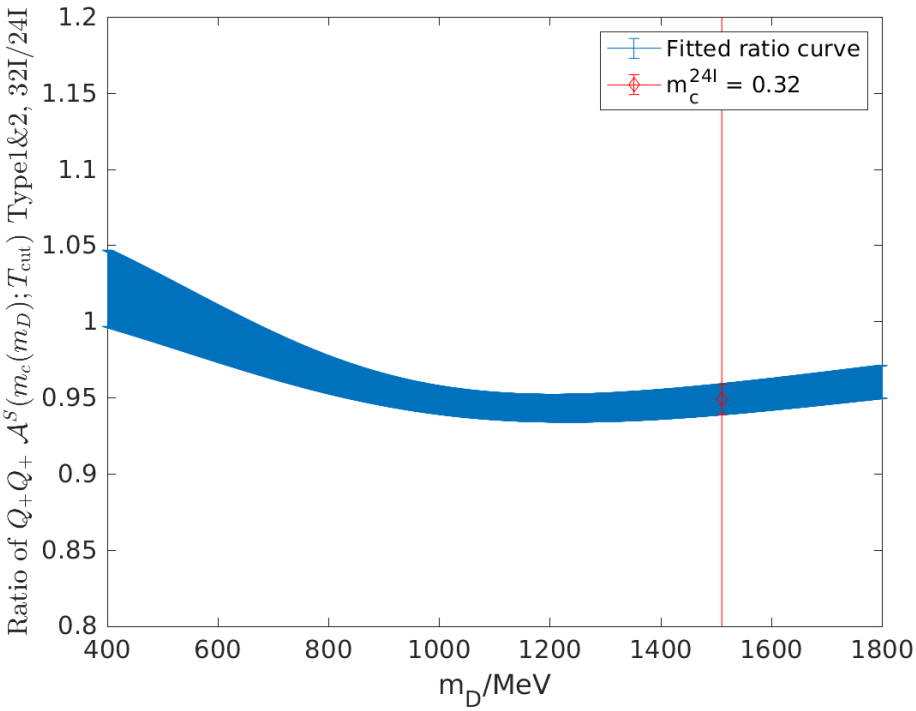

(c)

Figure 5.13: The single-integrated correlators with two Q_+ operators plotted as a function of m_D on the 24I ensemble (a) and on the 32I ensemble (b). Their ratio is plotted as a function of m_D in (c).

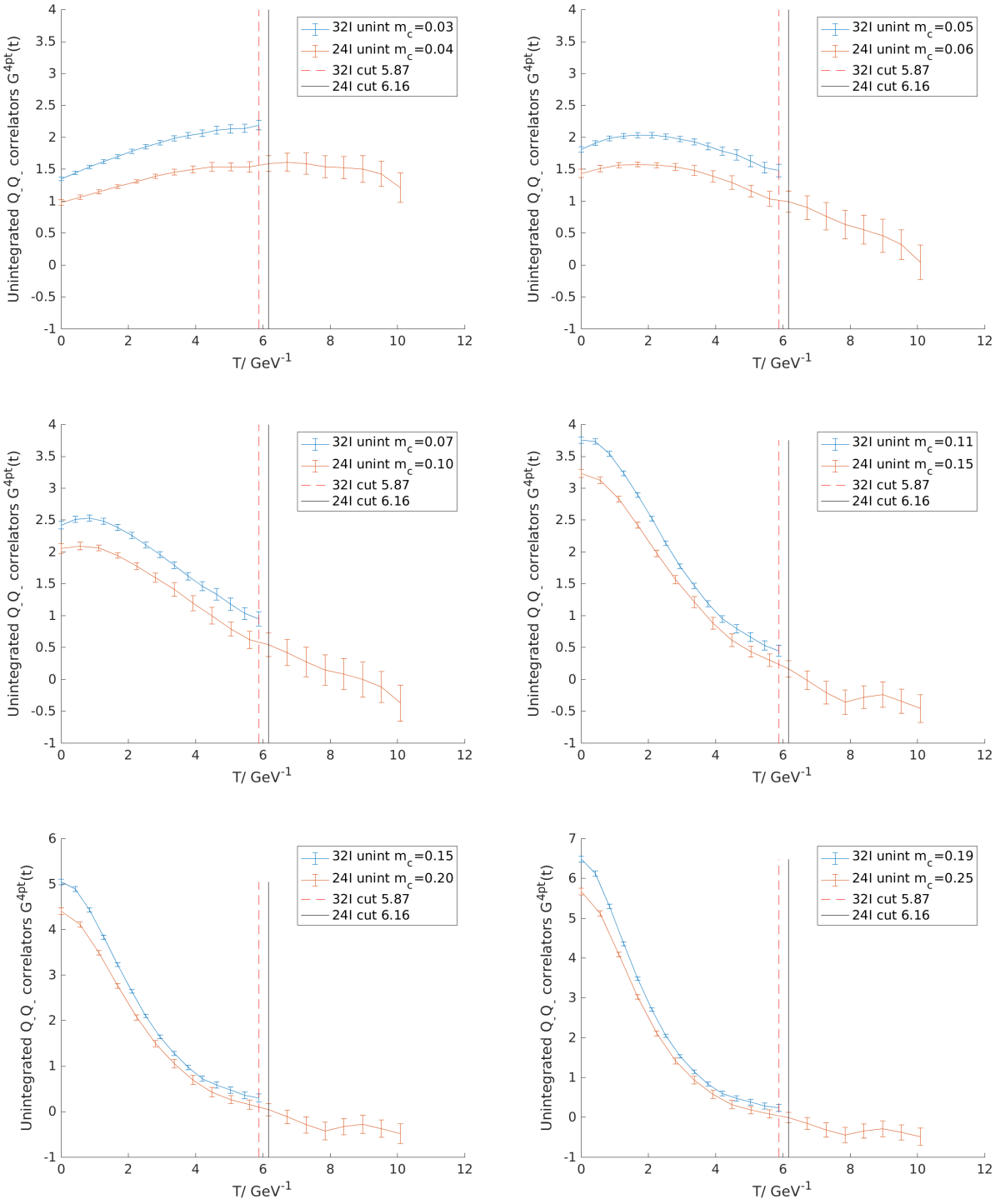

Figure 5.14: The 32I and 24I unintegrated correlators with two Q_- operators at same physical D meson masses. The vertical lines are the cutoff physical time for the single-integration and an additional interpolation is performed to remove the $O(a)$ errors due to the difference of the integration range.

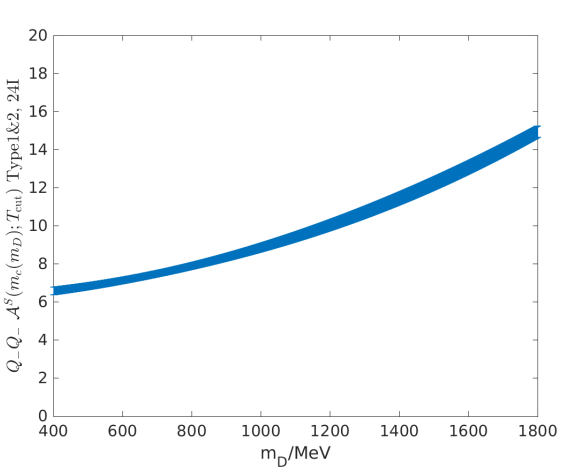

(a)

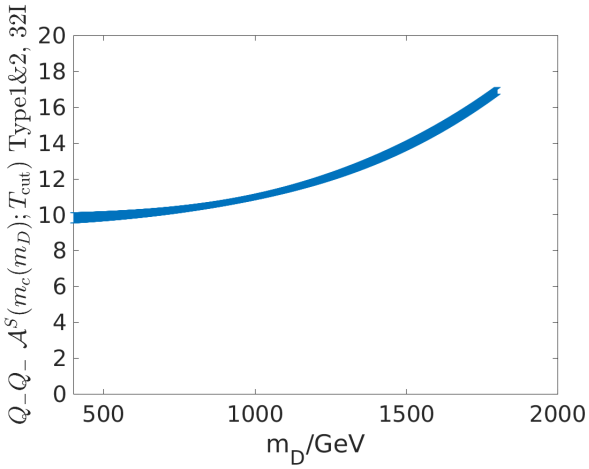

(b)

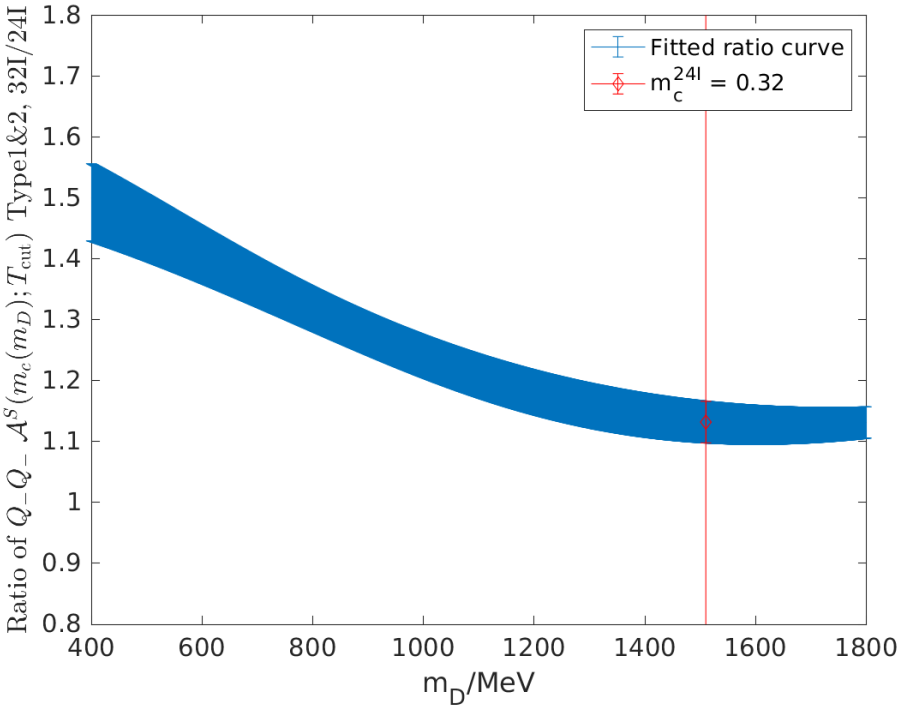

(c)

Figure 5.15: The single-integrated correlators with two Q_- operators plotted as a function of m_D on the 24I ensemble (a) and on the 32I ensemble (b). Their ratio is plotted as a function of m_D in (c).

Chapter 6: Δm_K calculation with physical quark masses

6.1 Details of calculation

The calculation was performed on the 64I ensemble and the details about the ensemble are listed in Table 3.1. For the 2+1 quark flavors, the valence quark masses are set to be their unitary values, and we include a physical valence charm quark with mass in lattice units of $m_c a = 0.31$, which is close to the value determined by fitting the D_s mass or η_c mass.

As discussed in Section 3.3.3, in our calculation, type-3 and type-4 diagrams are AMA corrected while type-1 and type-2 diagrams are only calculated as part of the exact measurements that are also used to determine the AMA corrections for the type-3 and type-4 diagrams. We have in total 152 configurations and the numbers of configurations used in different types of diagrams are listed in Table 6.1. For type-1, type-2 and type-3 diagrams, we use single separation $\Delta = 48$ between the kaon source and kaon sink and for type-4 diagrams, we use multiple source-sink separations $\Delta \in \{20, 21, ..., 48\}$ to increase the statistics. We set $t_{K,\text{min}}$ which is the minimum time difference between the weak operators and the kaon source or sink, to be 10.

Diagram types	sample AMA correction	# of Sloppy	# of Exact
Type-3&4	Y	116	36
Type-1&2	N	0	36

Table 6.1: Numbers of configurations with different CG precision for different types of diagrams in our Δm_K calculation with sample AMA correction.

The lattice calculation is performed on a BG/Q supercomputer partition with 8192 nodes. It takes about 5.5 hours for a "sloppy" calculation on one configuration and 20.5 hours for both "sloppy" and "exact" calculations on a BG/Q partition with 8192 nodes.

On each gauge configuration, we read in 2000 Lanczos eigenvectors calculated for light quarks which can be constructed from 400 base eigenvectors with multi-grid Lanczos technique[25],

which saves about 90% of the disk space for the storage of Lanczos eigenvectors. The eigenvectors are used in low-mode deflation and construction of A2A propagators for self-loop propagators. The high mode components of the A2A propagators are evaluated from 60 random volume sources.

6.2 Results

6.2.1 Two-point results

We plot the effective mass $m_{\text{eff}}(t)$ from two-point correlation functions as defined in Equation 4.2 for the mesons. The effective mass plots are shown in Figure 6.1 for K^0 and π ground states, Figure 6.2 for the $\pi-\pi$ states and Figure 6.3 for the η state. We fit the plateaus in the plots to obtain

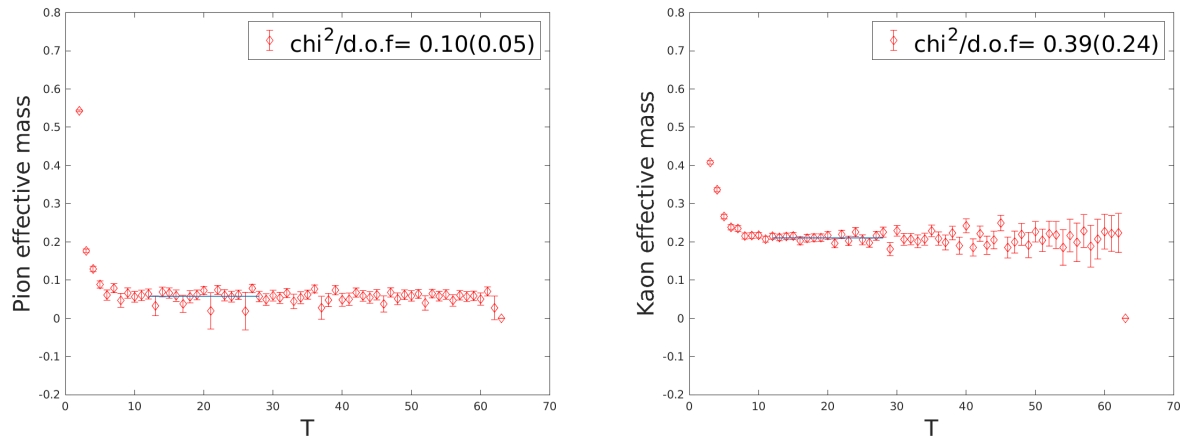

(a) (b)

Figure 6.1: Effective mass plots for the kaon (a) and pion (b) ground states. The mean values and errors from uncorrelated fits are plotted as three straight lines within the fitting range.

masses for our calculation. The results are shown in Table 6.2 in both lattice units (a^{-1} = 2.36 GeV) and physical units.

Unit	K^0	π	η	$\pi\pi_{I=0}$	$\pi\pi_{I=2}$
lattice	0.2104(1)	0.0574(1)	0.258(2)	0.1138(5)	0.1149(2)
MeV	496.5(3)	135.4(2)	609(37)	268.5(1.3)	271.1(5)

Table 6.2: Fitting results for meson masses and $\pi - \pi$ energies in lattice units (a^{-1} = 2.36 GeV) and in physical units.

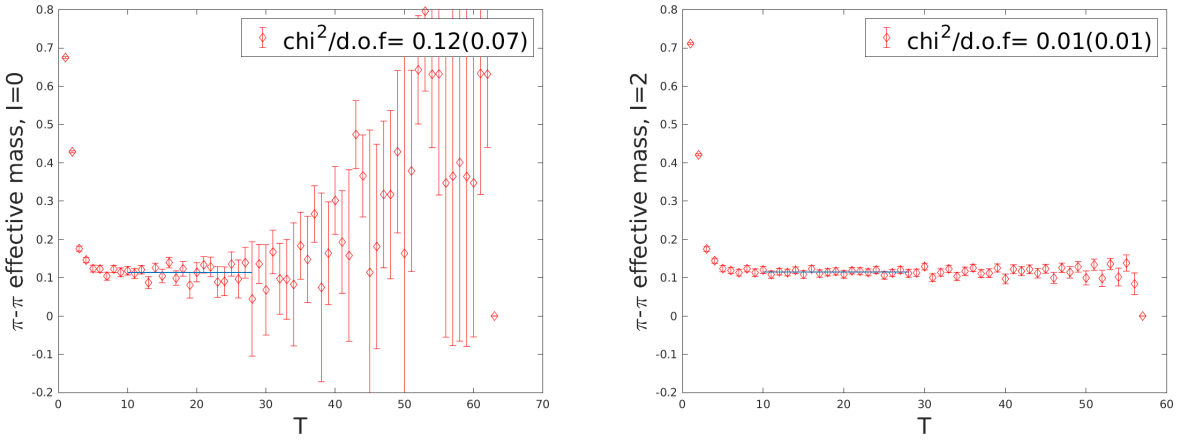

(a) (b)

Figure 6.2: Effective mass plots for the $\pi - \pi$, $I = 0$ (a) and $\pi - \pi$, $I = 2$ (b) ground states. The two single pion operators in both the source and sink are separated by 6 lattice units in time. The mean values and errors from uncorrelated fits are plotted as three straight lines within the fitting range.

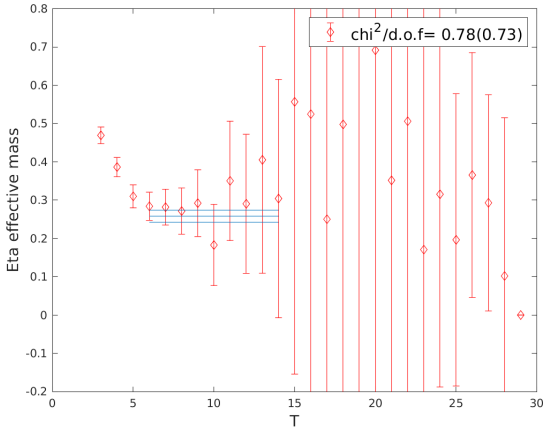

Figure 6.3: The effective mass plots for the η ground state.

These values are close to the experimental values of the meson masses and verify that our calculation on the 64I ensemble with physical quark masses produces mesons with physical masses we expect.

6.2.2 Three-point light-state matrix elements: overview

As discussed in Section 3.1.1, in our calculation of Δm_K, we have to subtract light state contributions from our unintegrated correlators and add light state contributions back to Δm_K after the single integration. We have to calculate $\langle\pi|Q_i'|K^0\rangle$, $\langle\pi\pi_{I=0}|Q_i'|K^0\rangle$ where the Q_i' operators are defined as:

$$Q_i' = Q_i - c_{\mathrm{p}i}\bar{s}\gamma_5 d - c_{\mathrm{s}i}\bar{s}d, \tag{6.1}$$

and the coefficients $c_{\mathrm{s}i}$ and $c_{\mathrm{p}i}$ are calculated from the ratios of the matrix elements:

$$c_{\mathrm{s}i} = \frac{\langle\eta|Q_i|K^0\rangle}{\langle\eta|\bar{s}d|K^0\rangle}, \quad c_{\mathrm{p}i} = \frac{\langle 0|Q_i|K^0\rangle}{\langle 0|\bar{s}\gamma_5 d|K^0\rangle}. \tag{6.2}$$

so that contributions from the $|0\rangle$ and $|\eta\rangle$ will vanish:

$$\langle 0|H_W - c_{\mathrm{p}}\bar{s}\gamma_5 d|K^0\rangle = 0, \quad \langle\eta|H_W - c_{\mathrm{s}}\bar{s}d|K^0\rangle = 0. \tag{6.3}$$

6.2.3 Three-point light-state matrix elements: K to π matrix elements

To calculate $\langle\pi|Q_i'|K^0\rangle$, we need to calculate $\langle\pi|Q_i|K^0\rangle$ and $\langle\pi|\bar{s}\gamma_5 d|K^0\rangle$ and combine them as below:

$$\langle\pi|Q_i'|K^0\rangle = \langle\pi|Q_i|K^0\rangle - c_{\mathrm{s}i}\langle\pi|\bar{s}d|K^0\rangle. \tag{6.4}$$

In Figure 6.4, we plot the three-point correlation functions as discussed in Section 4.1.2:

$$\widetilde{C}^{Q_i}_{K\to\pi}(\Delta, t) \equiv \frac{N_\pi N_K C^{Q_i}_{K\to\pi}(\Delta, t)}{C^{\mathrm{2pt}}_\pi(\Delta - t)C^{\mathrm{2pt}}_K(t)}, \tag{6.5}$$

$$\widetilde{C}^{\bar{s}d}_{K\to\pi}(\Delta,t) \equiv \frac{N_\pi N_K C^{\bar{s}d}_{K\to\pi}(\Delta,t)}{C^{2\mathrm{pt}}_\pi(\Delta-t)C^{2\mathrm{pt}}_K(t)}. \tag{6.6}$$

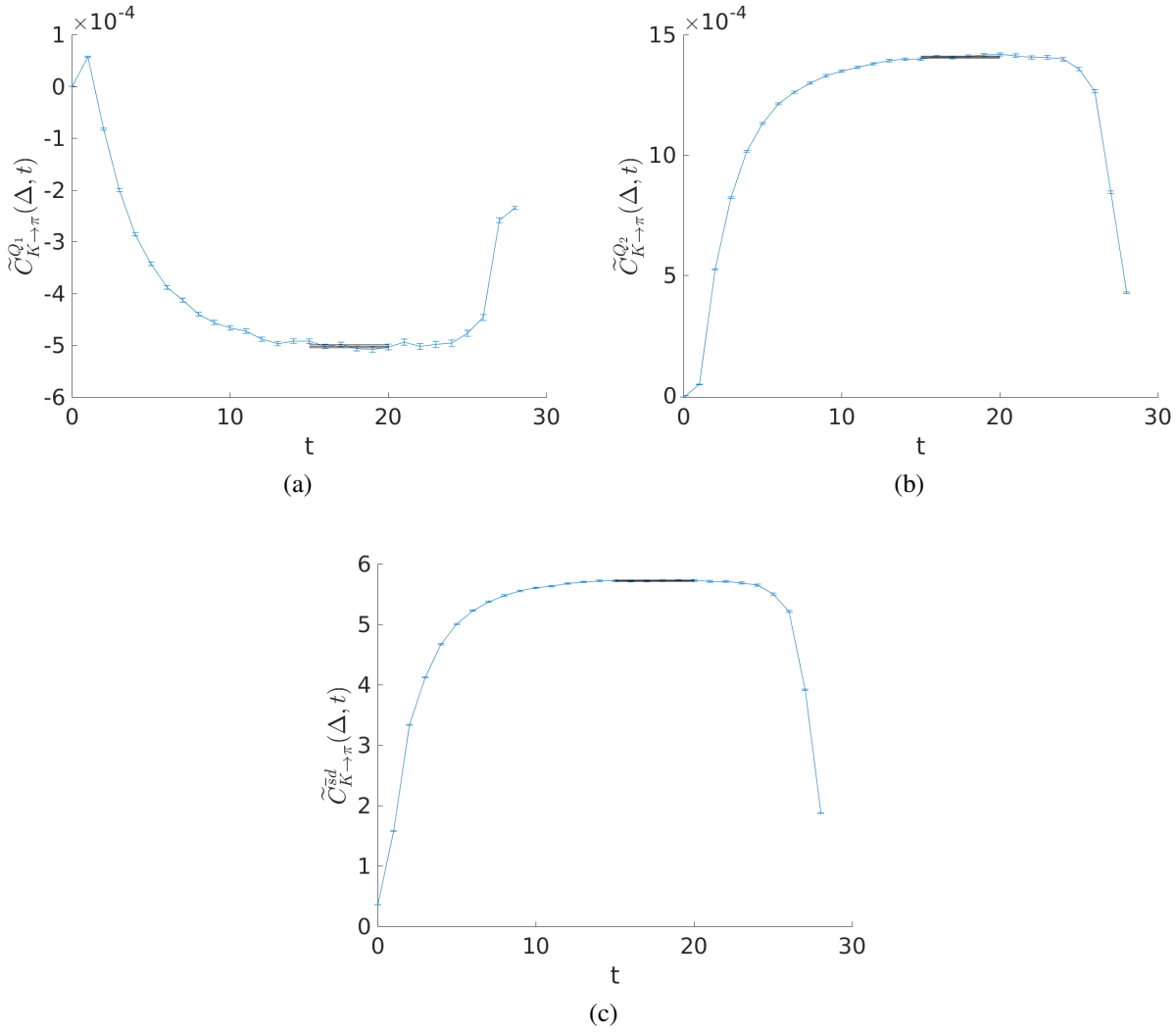

Figure 6.4: The three-point correlation functions $\widetilde{C}^{Q_1}_{K\to\pi}(\Delta,t)$ (a), $\widetilde{C}^{Q_2}_{K\to\pi}(\Delta,t)$ (b) and $\widetilde{C}^{\bar{s}d}_{K\to\pi}(\Delta,t)$ (c) plotted as functions of operator-kaon-source time separation t. We use a single source-sink separation $\Delta = 28$. The values of $\langle\pi|Q_1|K^0\rangle$, $\langle\pi|Q_2|K^0\rangle$ and $\langle\pi|\bar{s}d|K^0\rangle$ are obtained from the fitting of plateaus. The mean values and errors from uncorrelated fits are plotted as three straight lines within the fitting range.

We use a single source-separation $\Delta = 28$ and fit the correlation functions to constants in the region of various values of t where plateaus are observed and fitted values should be equal to the matrix elements $\langle\pi^0|Q_i|K^0\rangle$ and $\langle\pi^0|\bar{s}d|K^0\rangle$ separately. In Table 6.3, we list the values of these kaon to pion matrix elements. The coefficients c_{si} calculated from the kaon to eta matrix elements

will be shown in Section 6.2.4.

$\langle\pi\|Q_1\|K^0\rangle$	$\langle\pi\|Q_2\|K^0\rangle$	$\langle\pi\|\bar{s}d\|K^0\rangle$
$-5.02(3)\times10^{-4}$	$1.408(4)\times10^{-3}$	8.097(15)

Table 6.3: The K^0 to π matrix elements $\langle\pi|Q_1|K^0\rangle$, $\langle\pi|Q_2|K^0\rangle$ and $\langle\pi|\bar{s}d|K^0\rangle$ obtained from the fitting of plateaus.

Following the discussion in Section 5.2, we expect the time-dependence of the three-point correlation functions with the around-the-world effects included to be approximately given by:

$$C^{Q_i}_{K\to\pi}(\Delta,t)\propto\langle\pi|Q_i|K^0\rangle e^{-m_K t}e^{-m_\pi(\Delta-t)}+\langle 0|Q_i|K^0,\pi\rangle e^{-m_K t}e^{-m_\pi[T-(\Delta-t)]}, \tag{6.7}$$

and we can obtain the matrix element $\langle 0|Q_i|K^0,\pi\rangle$ outside the region between the kaon source and pion sink to estimate the around-the-world effects and justify our fitting formulas discussed in Section 4.1.2. We plot the three-point correlation functions:

$$\widetilde{C}^{Q_i}_{K,\pi\to0}(\Delta,t=\Delta+t')\equiv\frac{N_\pi N_K C^{Q_i}_{K,\pi\to0}(\Delta,t=\Delta+t')}{C^{2\mathrm{pt}}_\pi(t')C^{2\mathrm{pt}}_K(\Delta+t')} \tag{6.8}$$

and

$$\widetilde{C}^{\bar{s}d}_{K,\pi\to0}(\Delta,t=\Delta+t')\equiv\frac{N_\pi N_K C^{\bar{s}d}_{K,\pi\to0}(\Delta,t=\Delta+t')}{C^{2\mathrm{pt}}_\pi(t')C^{2\mathrm{pt}}_K(\Delta+t')} \tag{6.9}$$

in Figure 6.5 and fit each curve in the plateau region to constants which should equal to the matrix elements $\langle 0|Q_i|K^0,\pi\rangle$ and $\langle 0|\bar{s}d|K^0,\pi\rangle$ separately. The results are shown in Table 6.4.

$\langle 0\|Q_1\|K^0,\pi\rangle$	$\langle 0\|Q_2\|K^0,\pi\rangle$	$\langle 0\|\bar{s}d\|K^0,\pi\rangle$
$-1.90(2)\times10^{-3}$	$2.97(3)\times10^{-3}$	11.36(14)

Table 6.4: The estimated contribution from around-the-world K^0 and π to vacuum matrix element.

We can therefore estimate the around-the-world effects in our calculations of K^0 to π matrix elements by examining the ratios between the terms from the conventional propagation path and

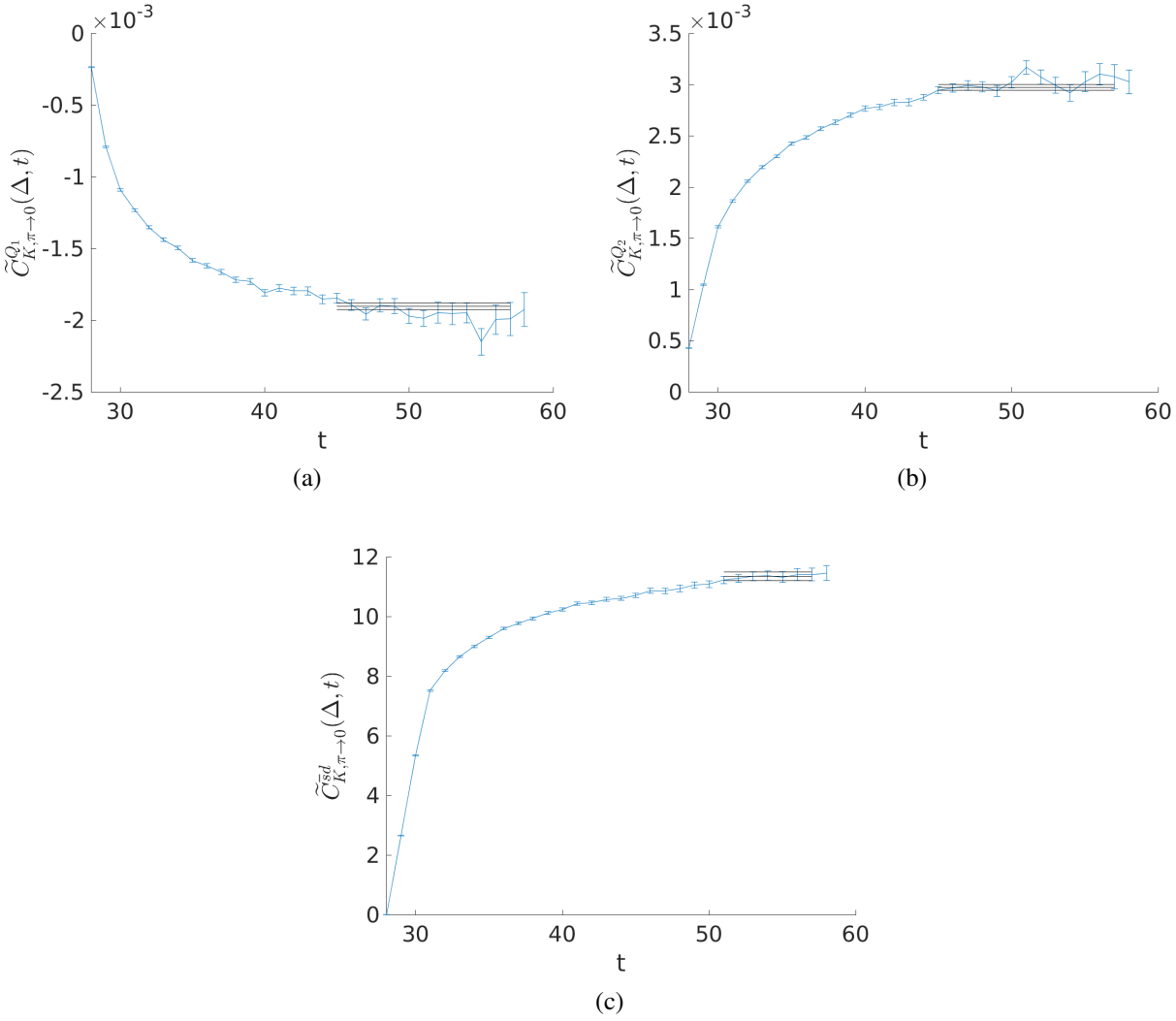

Figure 6.5: Around-the-world three-point functions $\widetilde{C}^{Q_1}_{K,\pi\to 0}(\Delta, t = \Delta + t')$ (a) and $\widetilde{C}^{Q_2}_{K,\pi\to 0}(\Delta, t = \Delta + t')$ (b) plotted as functions of operator-kaon-source time separation t. We use a single source-sink separation $\Delta = 28$. The values of $\langle 0|Q_1|K^0,\pi\rangle$, $\langle 0|Q_2|K^0,\pi\rangle$ and $\langle 0|\bar{s}d|K^0,\pi\rangle$ are obtained from the fitting of plateaus. The mean values and errors from uncorrelated fits are plotted as three straight lines within the fitting range.

the around-the-world path in Equation 6.7. For Q_1 operator, we have:

$$\mathcal{R}_1 = \frac{\langle 0|Q_1|K^0,\pi\rangle}{\langle \pi|Q_1|K^0\rangle} \times \frac{e^{-m_\pi(T-\tau)}}{e^{-m_\pi\tau}} = \frac{\langle \pi|Q_1|K^0\rangle}{\langle 0|Q_1|K^0,\pi\rangle} \times e^{-m_\pi(T-2\tau)} \tag{6.10}$$

where $\tau = \Delta - t$. If we take the maximum value of $\tau_{\max} = \Delta - t_{\min,\mathrm{K}} = 28 - 16 = 12$, we obtain the upper bound of the ratio of the around-the-world effects:

$$\mathcal{R}_{1,\max} = \frac{\langle \pi|Q_1|K^0\rangle}{\langle 0|Q_1|K^0,\pi\rangle} \times e^{-m_\pi(T-2\tau_{\max})} = \frac{-1.90\times10^{-3}}{-5.02\times10^{-4}} \times e^{-0.0574\times(128-2\times12)} = 0.0097 \sim 1.0\% \tag{6.11}$$

Similarly, we obtain the upper bound of the ratio for Q_2 matrix element:

$$\mathcal{R}_{2,\max} = \frac{\langle \pi|Q_2|K^0\rangle}{\langle 0|Q_2|K^0,\pi\rangle} \times e^{-m_\pi(T-2\tau_{\max})} = \frac{2.97\times10^{-3}}{1.41\times10^{-3}} \times e^{-0.0574\times(128-2\times12)} = 0.0054 \sim 0.5\% \tag{6.12}$$

and the upper bound of the ratio for $\bar{s}d$ matrix element:

$$\mathcal{R}_{\bar{s}d,\max} = \frac{\langle \pi|\bar{s}d|K^0\rangle}{\langle 0|\bar{s}d|K^0,\pi\rangle} \times e^{-m_\pi(T-2\tau_{\max})} = \frac{8.097}{11.36} \times e^{-0.0574\times(128-2\times12)} = 0.0018 \sim 0.2\% \tag{6.13}$$

Based on the values of $\mathcal{R}_{1,\max}$ $\mathcal{R}_{2,\max}$ and $\mathcal{R}_{\bar{s}d,\max}$, we can therefore conclude that the around-the-world effects are negligible and we can fit the three-point correlators using Equation 4.8 to obtain three-point matrix elements with negligible systematic errors from the around-the-world effects.

6.2.4 Three-point subtraction coefficients: $c_{\mathrm{s}i}$ and $c_{\mathrm{p}i}$

To calculate coefficients $c_{\mathrm{p}i} = \frac{\langle 0|Q_i|K^0\rangle}{\langle 0|\bar{s}\gamma_5 d|K^0\rangle}$, we obtain the kaon to vacuum matrix elements in a similar manner to the calculation of kaon to pion matrix elements and list them in Table 6.5. Then we take their ratios and the values of $c_{\mathrm{p}i}$ are listed in Table 6.7.

Compared to the coefficients $c_{\mathrm{p}i}$, the coefficients $c_{\mathrm{s}i} = \frac{\langle \eta|Q_i|K^0\rangle}{\langle \eta|\bar{s}d|K^0\rangle}$ have larger statistical errors due to the disconnected diagrams needed to calculate the kaon to eta matrix elements. To increase the

$\langle 0\|Q_1\|K^0\rangle$	$\langle 0\|Q_2\|K^0\rangle$	$\langle 0\|\bar{s}\gamma_5 d\|K^0\rangle$
$-1.284(3)\times 10^{-2}$	$2.449(4)\times 10^{-2}$	87.22(13)

Table 6.5: The kaon to vacuum matrix element, and the matrix element of $\bar{s}\gamma_5 d$ operator to be subtracted.

statistics, the calculations of c_{si} are performed with multiple values of source-sink separation Δ as described in Section 4.1.3. The total number of separations N_{sep}, the minimum separation Δ_{min}, the maximum separation Δ_{max} and Δ_{step} are listed in Table 6.6.

N_{sep}	Δ_{min}	Δ_{max}	Δ_{step}
5	16	40	6

Table 6.6: Parameters used for fitting three-point correlation functions with multiple source-sink separations.

We first obtain $\mathcal{R}_{si}^{Q_i}(\Delta,\delta)$ with the same δ values for all allowed source-sink separations Δ and perform an error-weighted average to obtain:

$$\widetilde{\mathcal{R}}_{si}^{Q_i}(\delta) = \left\langle \mathcal{R}_{si}^{Q_i}(\Delta,\delta)\right\rangle_{\Delta} = \left\langle \frac{C_{K\to\eta}^{Q_i}(\Delta,\delta)}{C_{K\to\eta}^{\bar{s}d}(\Delta,\delta)}\right\rangle_{\Delta}, \tag{6.14}$$

and then plot the ratios functions as shown in Figure 6.6 and fit the plateaus to constants which should equal the subtraction coefficients c_{si}. We have listed the fitting results of c_{si} in Table 6.7. We can see the coefficients c_{si} have relative large statistical errors which will significantly influence the statistical error of Δm_K. In the future, to further reduce the statistical error of Δm_K, we should focus on the statistical error reduction for the coefficients c_{si}.

c_{s1}	c_{s2}	c_{p1}	c_{p2}
$2.06(32)\times 10^{-4}$	$-3.12(21)\times 10^{-4}$	$-1.473(2)\times 10^{-4}$	$2.808(2)\times 10^{-4}$

Table 6.7: The subtraction coefficients for the scalar and pseudo-scalar operators determined from the kaon to eta and kaon to vacuum matrix elements of Q_1, Q_2, $\bar{s}d$ and $\bar{s}\gamma_5 d$ operators.

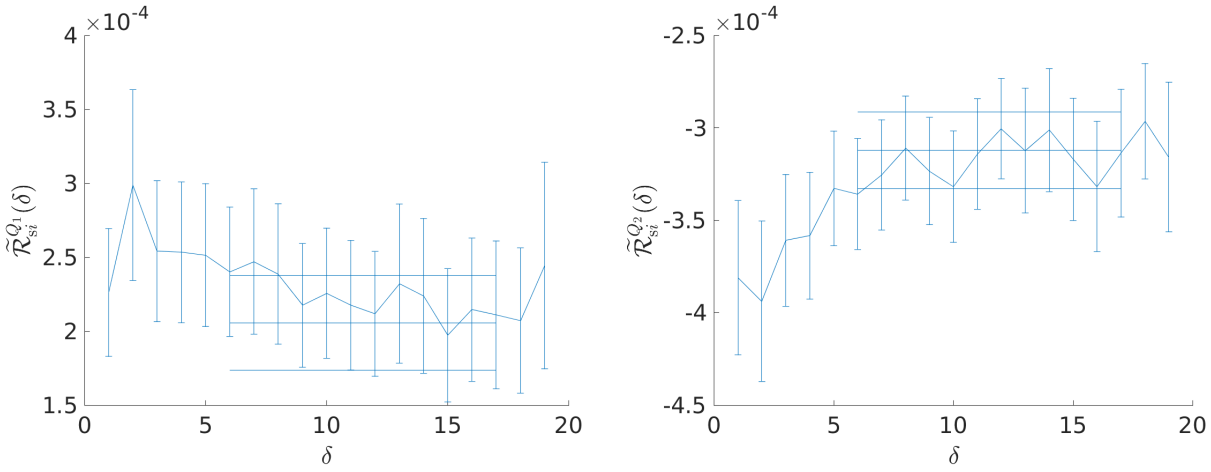

(a) (b)

Figure 6.6: The three-point ratio functions $\widetilde{\mathcal{R}}^{Q_1}_{si}(\delta)$ (a), and $\widetilde{\mathcal{R}}^{Q_2}_{si}(\delta)$ (b) plotted as functions of operator-pion-sink time separation δ. We use multiple source-sink separations which are shown in Table 6.6 to obtain $\mathcal{R}^{Q_i}_{si}(\Delta,\delta)$ and perform an error-weighted average over all allowed source-sink separations Δ for each δ value to obtain $\widetilde{\mathcal{R}}^{Q_i}_{si}(\delta)$. The values of c_{s1} and c_{s2} are obtained from the fitting of plateaus. The mean values and errors from uncorrelated fits are plotted as three straight lines within the fitting range.

6.2.5 Three-point light-state matrix elements: K to $\pi\pi$ matrix elements

To increase the statistics, the calculations of $\langle \pi\pi_{I=0}|Q'_i|K^0\rangle$ are performed with multiple values of source-sink separation Δ as described in Section 4.1.3. The total number of separations N_{sep}, minimum separation Δ_{min}, maximum separation Δ_{max} and Δ_{step} are listed in Table 6.6.

We first combine the kaon to two pion three-point correlation functions $C^{Q_i}_{K\to\pi\pi_{I=0}}(\Delta,\delta)$ with $C^{\bar{s}\gamma_5 d}_{K\to\pi\pi_{I=0}}(\Delta,\delta)$ multiplied by the subtraction coefficients $c_{\text{p}i}$ which are listed in Table 6.7 to obtain $C^{Q'_i}_{K\to\pi\pi_{I=0}}(\Delta,\delta)$. We then perform error-weighted average on $C^{Q'_i}_{K\to\pi\pi_{I=0}}(\Delta,\delta)$ with the same δ values over all allowed source-sink separations Δ to obtain:

$$\overline{\widetilde{C}}^{Q'_i}_{K\to\pi\pi_{I=0}}(\delta) = \left\langle \widetilde{C}^{Q'_i}_{K\to\pi\pi_{I=0}}(\Delta,t)\right\rangle_\Delta = \left\langle \frac{N_{\pi\pi_{I=0}} N_K C^{Q'_i}_{K\to\pi\pi_{I=0}}(\Delta,\delta)}{C^{\text{2pt}}_{\pi\pi_{I=0}}(\Delta-t)C^{\text{2pt}}_K(t)}\right\rangle_\Delta, \tag{6.15}$$

where $\left\langle ... \right\rangle_\Delta$ denotes the error weighted average among all possible Δ values. And then we plot

the three-point functions $\overline{\widetilde{C}}^{Q_i'}_{K\to\pi\pi_{I=0}}(\delta)$ shown in Figure 6.7 and fit the plateaus to constants which should equal the matrix elements $\langle\pi\pi_{I=0}|Q_i'|K^0\rangle$. Similarly, for kaon to the $\pi\pi, I = 2$ state matrix elements, we plot the three-point functions $\overline{\widetilde{C}}^{Q_i}_{K\to\pi\pi_{I=2}}(\delta)$ shown in Figure 6.8 and fit the plateaus to constants which should equal the matrix elements $\langle\pi\pi_{I=2}|Q_i|K^0\rangle$. Please note there is no mixed diagrams related to the $\bar{s}\gamma_5 d$ operator for the kaon to the $\pi\pi, I = 2$ state matrix elements and therefore there is no prime on the operators Q_i in the matrix elements $\langle\pi\pi_{I=2}|Q_i|K^0\rangle$.

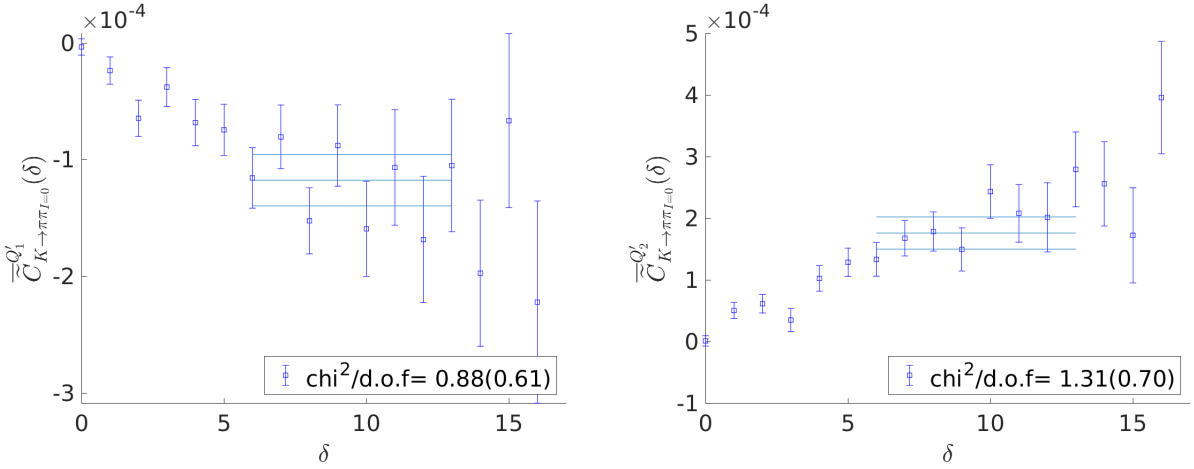

(a) (b)

Figure 6.7: The three-point functions $\overline{\widetilde{C}}^{Q_1'}_{K\to\pi\pi_{I=0}}(\delta)$ (a), and $\overline{\widetilde{C}}^{Q_2'}_{K\to\pi\pi_{I=0}}(\delta)$ (b) plotted as functions of the operator-two-pion-sink time separation δ. We use multiple source-sink separations which are shown in Table 6.6 to obtain $C^{Q_i'}_{K\to\pi\pi_{I=0}}(\Delta,\delta)$ and perform an error-weighted average over all allowed source-sink separations Δ for each δ value to obtain $\overline{\widetilde{C}}^{Q_i'}_{K\to\pi\pi_{I=0}}(\delta)$. The values of the matrix elements $\langle\pi\pi_{I=0}|Q_1'|K^0\rangle$ and $\langle\pi\pi_{I=0}|Q_2'|K^0\rangle$ are obtained from the fitting of plateaus. The mean values and errors from uncorrelated fits are plotted as three straight lines within the fitting range.

We have listed the fitting results of $\langle\pi\pi_{I=0}|Q_i'|K^0\rangle$ and $\langle\pi\pi_{I=2}|Q_i|K^0\rangle$ in Table 6.8.

$\langle\pi\pi_{I=2}\|Q_1\|K^0\rangle$	$\langle\pi\pi_{I=2}\|Q_2\|K^0\rangle$	$\langle\pi\pi_{I=0}\|Q_1'\|K^0\rangle$	$\langle\pi\pi_{I=0}\|Q_2'\|K^0\rangle$
$1.449(4)\times10^{-5}$	$1.449(4)\times10^{-5}$	$-11.8(2.2)\times10^{-5}$	$17.6(2.6)\times10^{-5}$

Table 6.8: The K to $\pi\pi$ matrix element for Isospin 0 and 2. The I=2 matrix elements for Q_1 and Q_2 have the same values because they come from the same three point diagrams because of the Fierz symmetry.

As shown in Table 6.8, we can see K to $\pi\pi$, $I = 2$ matrix elements are about a order of

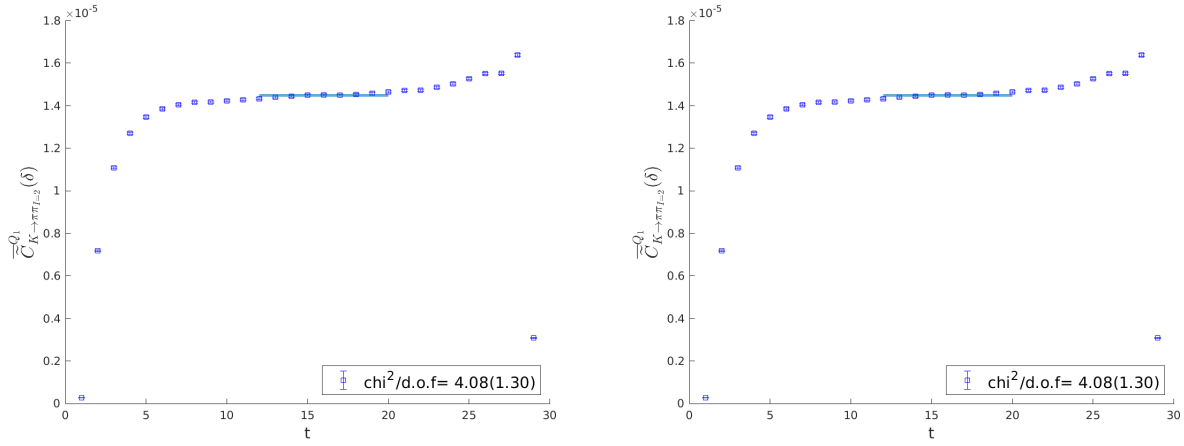

(a) (b)

Figure 6.8: The three-point functions $\overline{\approx}^{Q_1}_{K\to\pi\pi_{I=2}}(\delta)$ (a), and $\overline{\approx}^{Q_2}_{K\to\pi\pi_{I=2}}(\delta)$ (b) plotted as functions of the operator-two-pion-sink time separation δ. We use multiple source-sink separations which are shown in Table 6.6 to obtain $C^{Q_i}_{K\to\pi\pi_{I=2}}(\Delta,\delta)$ and perform an error-weighted average over all allowed source-sink separations Δ for each δ value to obtain $\overline{\approx}^{Q_i}_{K\to\pi\pi_{I=2}}(\delta)$. The values of the matrix elements $\langle\pi\pi_{I=2}|Q_1|K^0\rangle$ and $\langle\pi\pi_{I=2}|Q_2|K^0\rangle$ are obtained from the fitting of plateaus. The mean values and errors from uncorrelated fits are plotted as three straight lines within the fitting range.

magnitude smaller than the matrix elements for the $I = 0$ case and this is consistent with our expectation. Using the matrix elements of K to $\pi\pi$, $I = 0$ matrix elements, we can calculate the contribution to Δm_K from the $\pi\pi$, $I = 0$ state:

$$\Delta m_K^{(\pi\pi_{I=0})} = \frac{G_F^2}{2}\lambda_u^2 \sum_{i,j=1,2}(-2)\times C_i^{\text{lat}} C_j^{\text{lat}}\left[-\frac{\langle\overline{K^0}|Q_i'|\pi\pi_{I=0}\rangle\langle\pi\pi_{I=0}|Q_j'|K^0\rangle}{m_K - E_{\pi\pi}}\right] = 0.067(39)\times 10^{-12}\text{MeV}, \tag{6.16}$$

and find that it contributes only about 1% to the mass difference.

6.3 Contributions to Δm_K

As discussed in Section 3.1, in our single-integration method, we subtract the light states before integration and expect the resulting unintegrated correlator to decrease exponentially as the time separation between the two weak operator $\delta \equiv |t_1 - t_2|$ increases. By examining the values of the unintegrated correlators, we can identify the range of δ where the contributions are consistent with

zero and therefore avoid including their contributions to statistical errors.

The unintegrated four-point correlators as functions of δ are plotted in Figure 6.9. From the unintegrated correlators, we find for $\delta > 10$ the values of correlators are zero within uncertainties. Thus we choose the integration upper limit $T_{\text{cut}} = 10$ and obtain Δm_K from the single-integrated correlators $\mathcal{A}^S_{ij}(T = 10)$, where $i, j = 1, 2$ and T denotes the integration upper limit. The Δm_K value extracted from the single-integration method is shown in Table 6.9. We have used the Wilson coefficients in Table 3.4 following the same NPR schemes used in an earlier Δm_K calculation[2].

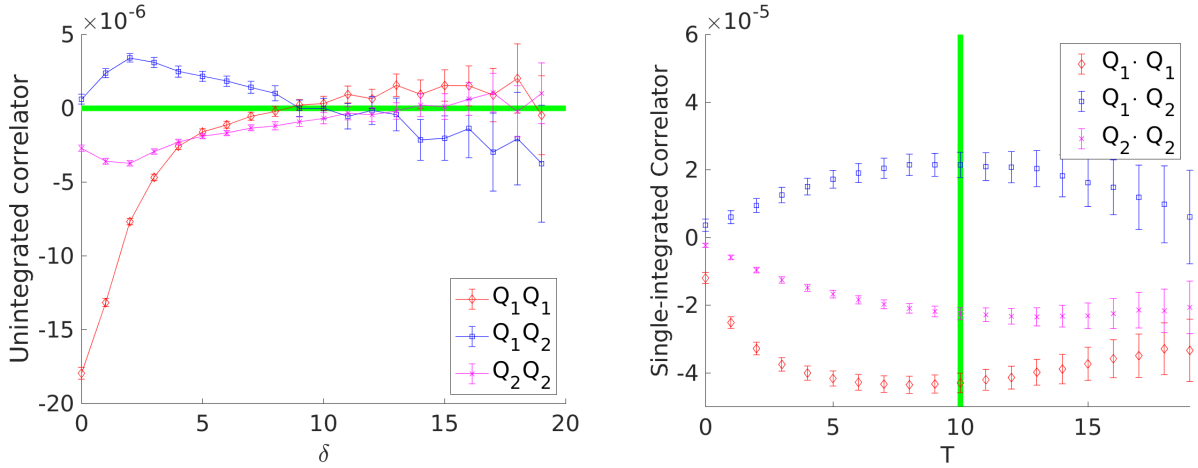

(a) (b)

Figure 6.9: The four-point correlators. (a) shows the unintegrated correlator obtained from an error-weighted average over all locations of the pair of operators subject to the constraint that neither operator is closer to the single kaon operators than 10 time units. (b) shows the correlators $\mathcal{A}^S_{ij}(T)$ obtain by integrating the data shown in the left plot over δ. Please note in each plot, the raw data from the lattice calculation is plotted and the y axis does not have meaningful units.

We also calculate Δm_K using double-integration method used in earlier calculations[1][7]. As shown in Figure 6.10, the double-integrated correlators show good linear time dependence as expected in the region $T \in [9, 19]$ and we therefore fit the curve to obtain Δm_K according to Equation (3.3) in Reference [7].The results are also listed in Table 6.9. Compared to the results using the double-integration method, the results from the single-integration method have smaller statistical errors, because we can exclude the statistical noise from the unintegrated correlators at large δ values.

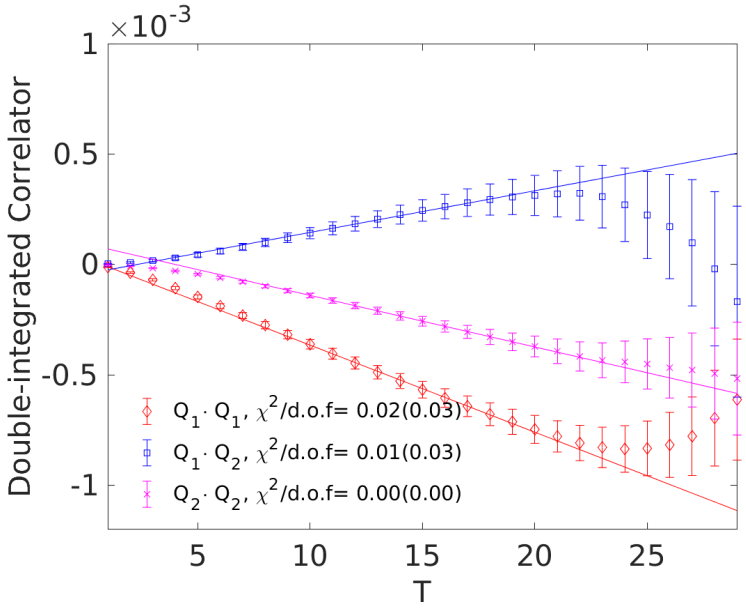

(a)

Figure 6.10: Double-integrated correlators $\mathcal{A}_{ij}(T)$. Please note in the plot, the raw data from the lattice calculation is plotted and the y axis does not have meaningful units.

Analysis method	Δm_K	Δm_K(type1&2)	Δm_K(type3&4)
Double-integration	6.31(0.98)	6.71(0.48)	-0.20(0.65)
Single-integration	6.34(0.57)	6.24(0.24)	0.33(0.50)

Table 6.9: Results for Δm_K in units of 10^{-12} MeV. Double-integration results are obtained from uncorrelated fits with fitting range 10:20.

In our Δm_K calculation, the type-1 and type-2 diagrams are connected and the type-3 and type-4 diagrams are disconnected. In order to check the validity of the OZI rule in our results, we also calculate the contributions to Δm_K from the connected diagrams and the disconnected diagrams separately. The separation is made as following: for the connected-only contribution, only type-1 and type-2 diagrams are included; all the rest contributions to Δm_K are included in the contributions from type-3 and type-4 diagrams. Please note the mixed diagrams due to our introduction of $\bar{s}d$ and $\bar{s}\gamma_5 d$ operators are combined with the type-3 and type-4 diagrams which have similar topologies.

Similar to the connected-only calculation in the scaling test of the four-point correlation functions discussed in Section 5.6.3, in our calculation of the contribution to Δm_K from the con-

nected type-1 and type-2 diagrams, we use the interpolating operator $O_{\pi^0} = i\overline{u}\gamma_5 u$ rather than $O_{\pi^0} = i(\overline{u}\gamma_5 u - \overline{d}\gamma_5 d)/\sqrt{2}$ and only include figure-8 diagrams to calculate the three-point matrix elements $\langle\pi|Q_i|K^0\rangle$ to remove the exponentially increasing terms from the single-integrated four-point correlators. In our calculation of the contribution to Δm_K from the disconnected type-3 and type-4 diagrams, when we subtract the light state terms, we subtract from the type-3 and type-4 unintegrated correlation functions the difference between the light-state terms in the full Δm_K calculation and the light-state terms in the connected-only calculation.

The unintegrated correlators from the two different types of diagrams are plotted in Figure 6.11 and corresponding contributions to Δm_K are shown in Table 6.9. The main contribution to Δm_K is from the type-1 and type-2 diagrams and the contribution from the type-3 and type-4 diagrams which are disconnected is zero within uncertainty. This may imply the validity of the OZI rule in the case of physical kinematics in contrast to the earlier calculation of Δm_K with unphysical kinematics[1], where contributions from type-3 and type-4 diagrams are almost half the size of the contributions from type-1 and type-2 diagrams but with the opposite sign.

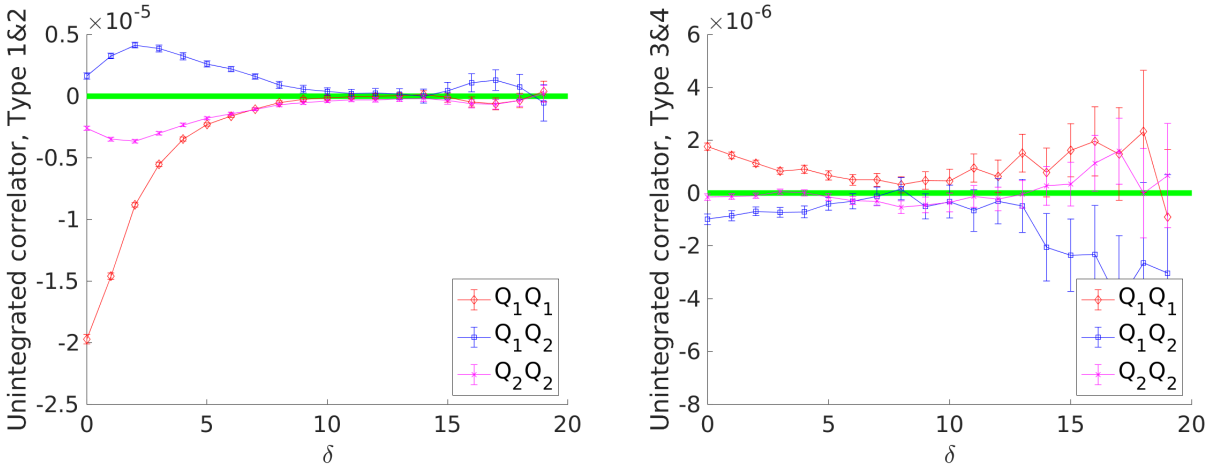

Figure 6.11: Unintegrated correlators from type-1 and type-2 diagrams (a) and type-3 and type-4 diagrams (b). Please note in each plot, the raw data from the lattice calculation is plotted and the y axis does not have meaningful units.

6.3.1 AMA correction

Our use of the sample AMA method reduced the computational cost of the calculation by a factor of 2.3, while the statistical error on the AMA correction will add to the total statistical error. Table 6.10 shows the size of the error coming from the correction which is added in quadrature to give our final error. We can conclude that the AMA method does not contribute much to the error in our final answer.

Analysis method	type 3&4 error from "sloppy"	type 3&4 error from correction	type 3&4 error in total
Double-integration	0.60	0.24	0.65
Single-integration	0.39	0.29	0.49

Table 6.10: Contributions to the statistical error for Δm_K from type-3 and type-4 diagrams (in units of 10^{-12} MeV). From left to right, type-3 and type-4 errors from the "sloppy", from the AMA correction and in total are shown. In our calculation, the type-3 and type-4 diagrams are AMA corrected while the type-1 and type-2 diagrams are calculated only as part of the exact measurements that are also used to determine the AMA corrections for the type-3 and type-4 diagrams.

6.4 Systematic errors

Two potentially important systematic errors come from finite-volume and finite lattice spacing effects. As discussed in Section 5.1, the potential large finite volume effects can be removed by performing a known correction. The finite-volume correction to Δm_K based on the discussion in Section 5.1 is estimated to be:

$$\delta(\Delta m_K)^{FV} = -0.54(18) \times 10^{-12}\text{MeV}. \tag{6.17}$$

As for the finite lattice spacing effects, the $O(a^2)$ error due to the heavy charm is estimated to be a significant source of systematic error. If we use the physical charm mass and our lattice spacing $a^{-1} = 2.36$ GeV for the estimate, this relative error should be $\sim (m_c a)^2 \sim 25\%$. Our the scaling tests at larger lattice spacings in Section 5.5 show that at $m_c a = 0.32$, the scaling

violation for the four-point single-integrated correlators with Q_+ operators is about 5% and the scaling violation with Q_- operators is about 13%. However, there is a scaling violation of size $\sim$ 40% being observed in the case with Q_- operators as $m_c a$ approaches zero and we therefore estimate the finite lattice spacing error of our Δm_K calculation to be $\sim$ 40%.

6.5 Conclusion

After including the finite volume correction, our result for Δm_K based on 152 configurations with physical quark masses is:

$$\Delta m_K = 5.8(0.6)_{\text{stat}}(2.3)_{\text{sys}} \times 10^{-12}\text{MeV}. \tag{6.18}$$

Here the first error is statistical and the second is an estimate of largest systematic error due to the finite lattice spacing effects.

Chapter 7: Conclusion and outlook

In this work, we have presented the first lattice QCD calculation of Δm_K , the mass difference between the long- and short-lived K mesons, with physical quark masses. The calculation was performed on an ensemble of 2+1 flavor gauge configurations with $a^{-1} = 2.36$GeV and a $64^3 \times 128$ lattice volume using 152 configurations. Our preliminary result for Δm_K is:

$$\Delta m_K = 5.8(0.6)_{\text{stat}}(2.3)_{\text{sys}} \times 10^{-12}\text{MeV}. \tag{7.1}$$

Here the first error is statistical and the second is an estimate of largest systematic error, the discretization error, based on the scaling tests performed on the 24I and 32I ensembles. Having a mature method to carry out the calculation with systematic errors under control, the next step is to increase the statistics and reduce the systematic errors. While the statistical error approaches a relatively small size of 10%, the systematic errors have more significant effects.

A comparison between our physical standard model Δm_K value and the experimental value $3.484(6) \times 10^{-12}$ MeV [4] suggests reasonable agreement given the large finite lattice spacing errors. Future calculations on the Summit supercomputer will extend our current scaling tests on the 24I and 32I ensembles to smaller lattice spacings, and will reveal a comprehensive picture about the finite lattice spacing errors. Calculations on a $96^3 \times 192$ lattice with $a^{-1} = 2.8$ GeV should improve the precision to $\sim 5\%$ level. The calculation on $96^3 \times 196$ lattice together with this completed calculation on the $64^3 \times 128$ ensemble with physical quark masses, will allow the continuum limit to be explored.

References

[1] Z. Bai, N. H. Christ, T. Izubuchi, C. T. Sachrajda, A. Soni, and J. Yu, "K_L–K_S mass difference from lattice qcd," Phys. Rev. Lett., vol. 113, p. 112 003, 11 2014.

[2] Bai, Ziyuan, Christ, Norman H., and Sachrajda, Christopher T., "The $K_L - K_S$ mass difference," EPJ Web Conf., vol. 175, p. 13 017, 2018.

[3] T. Inami and C. S. Lim, "Effects of Superheavy Quarks and Leptons in Low-Energy Weak Processes $K_L \to \mu\mu$, $K^+ \to \pi^+\nu\nu$ and $K^0 \leftrightarrow \overline{K^0}$," Progress of Theoretical Physics, vol. 65, no. 1, pp. 297–314, Jan. 1981. eprint: https://academic.oup.com/ptp/article-pdf/65/1/297/5252099/65-1-297.pdf.

[4] P. Zyla et al., "Review of Particle Physics," Prog. Theor. Exp. Phys., vol. 2020, no. 8, Aug. 2020, 083C01.

[5] J. Brod and M. Gorbahn, "Next-to-next-to-leading-order charm-quark contribution to the CP Violation Parameter ϵ_K and ΔM_K," Phys. Rev. Lett., vol. 108, p. 121 801, 12 2012.

[6] N. H. Christ, T. Izubuchi, C. T. Sachrajda, A. Soni, and J. Yu, "Long distance contribution to the $K_L - K_S$ mass difference," Phys. Rev. D, vol. 88, p. 014 508, 1 2013.

[7] B. Wang, "Results for the mass difference between the long- and short-lived K mesons for physical quark masses," PoS, vol. LATTICE2018, p. 286, 2019.

[8] N. H. Christ, X. Feng, G. Martinelli, and C. T. Sachrajda, "Effects of finite volume on the $K_L - K_S$ mass difference," Phys. Rev. D, vol. 91, p. 114 510, 11 2015.

[9] G. Buchalla, A. J. Buras, and M. E. Lautenbacher, "Weak decays beyond leading logarithms," Rev. Mod. Phys., vol. 68, pp. 1125–1244, 4 1996.

[10] J. Eeg and I. Picek, "K^0–$\overline{K^0}$ mixing at three loops short-distance double penguin-like diagrams," Nuclear Physics B, vol. 292, pp. 745–766, 1987.

[11] N. H. Christ, T. Izubuchi, C. Sachrajda, A. Soni, and J. Yu, "Calculating the $K_L - K_S$ mass difference and ϵ_K to sub-percent accuracy," PoS, vol. LATTICE 2013, p. 397, 2014.

[12] T. Blum, P. A. Boyle, N. H. Christ, J. Frison, N. Garron, R. J. Hudspith, T. Izubuchi, T. Janowski, C. Jung, A. Jüttner, C. Kelly, R. D. Kenway, C. Lehner, M. Marinkovic, R. D. Mawhinney, G. McGlynn, D. J. Murphy, S. Ohta, A. Portelli, C. T. Sachrajda, and A. Soni, "Domain wall qcd with physical quark masses," Phys. Rev. D, vol. 93, p. 074 505, 7 2016.

[13] T. Blum, T. Izubuchi, and E. Shintani, "New class of variance-reduction techniques using lattice symmetries," Phys. Rev. D, vol. 88, p. 094 503, 9 2013.

[14] C. Lehner and C. Sturm, "Matching factors for $\Delta S = 1$ four-quark operators in ri/smom schemes," Phys. Rev. D, vol. 84, p. 014 001, 1 2011.

[15] T. Blum, P. Chen, N. Christ, C. Cristian, C. Dawson, G. Fleming, R. Mawhinney, S. Ohta, G. Siegert, A. Soni, P. Vranas, M. Wingate, L. Wu, and Y. Zhestkov, "Kaon matrix elements and cp violation from quenched lattice qcd: The 3-flavor case," Phys. Rev. D, vol. 68, p. 114 506, 11 2003.

[16] Z. Bai, "$K_L - K_S$ mass difference from lattice QCD," Ph.D. thesis,

[17] J. D. Bratt, R. G. Edwards, M. Engelhardt, P. Hägler, H. W. Lin, M. F. Lin, H. B. Meyer, B. Musch, J. W. Negele, K. Orginos, A. V. Pochinsky, M. Procura, D. G. Richards, W. Schroers, and S. N. Syritsyn, "Nucleon structure from mixed action calculations using $2 + 1$ flavors of asqtad sea and domain wall valence fermions," Phys. Rev. D, vol. 82, p. 094 502, 9 2010.

[18] M. Lüscher, "Two-particle states on a torus and their relation to the scattering matrix," Nuclear Physics B, vol. 354, no. 2, pp. 531–578, 1991.

[19] T. Yamazaki, S. Aoki, M. Fukugita, K.-I. Ishikawa, N. Ishizuka, Y. Iwasaki, K. Kanaya, T. Kaneko, Y. Kuramashi, M. Okawa, A. Ukawa, and T. Yoshié, "I=2$\pi\pi$ scattering phase shift with two flavors of O (a) improved dynamical quarks," Phys. Rev. D, vol. 70, p. 074 513, 7 2004.

[20] L. M. Lellouch L., "Weak transition matrix elements from finite-volume correlation functions," Commun. Math. Phys., vol. 219, 31–44 2001.

[21] L. Jin, "Private communication,"

[22] T. Blum, P. A. Boyle, N. H. Christ, N. Garron, E. Goode, T. Izubuchi, C. Lehner, Q. Liu, R. D. Mawhinney, C. T. Sachrajda, A. Soni, C. Sturm, H. Yin, and R. Zhou, "k to $\pi\pi$ decay amplitudes from lattice qcd," Phys. Rev. D, vol. 84, p. 114 503, 11 2011.

[23] R. Arthur, T. Blum, P. A. Boyle, N. H. Christ, N. Garron, R. J. Hudspith, T. Izubuchi, C. Jung, C. Kelly, A. T. Lytle, R. D. Mawhinney, D. Murphy, S. Ohta, C. T. Sachrajda, A. Soni, J. Yu, and J. M. Zanotti, "Domain wall qcd with near-physical pions," Phys. Rev. D, vol. 87, p. 094 514, 9 2013.

[24] T. Blum, P. A. Boyle, N. H. Christ, J. Frison, N. Garron, T. Janowski, C. Jung, C. Kelly, C. Lehner, A. Lytle, R. D. Mawhinney, C. T. Sachrajda, A. Soni, H. Yin, and D. Zhang, "K$\rightarrow\pi\pi$ ΔI= $3/2$ decay amplitude in the continuum limit," Phys. Rev. D, vol. 91, p. 074 502, 7 2015.

[25] Clark, M. A., Jung, Chulwoo, and Lehner, Christoph, "Multi-grid lanczos," EPJ Web Conf., vol. 175, p. 14 023, 2018.

[26] J. Yu, "$K_L - K_S$ mass difference from lattice QCD," Ph.D. thesis,

[27] Izubuchi, T., "Note for four-dimensional free DWF propagators in momentum space," N/A,

[28] M. Tomii, "Private communication,"

Appendix A: Normalization conventions and dimensions of the matrix elements

In our lattice calculation, we need to multiply the lattice results by appropriate powers of the lattice spacing a to match the dimension of the physical quantities being calculated. Thus, we need to specify the dimensions of the physical quantities we calculate and evaluate them in physical units.

A.1 Normalization convention of meson states

The normalization convention used for the quantum states in the continuum infinite volume matrix elements we are computing, using the K meson as an example, is given by:

$$\langle K^0(\vec{p}_1)|K^0(\vec{p}_2)\rangle = (2\pi)^3\delta^3(\vec{p}_1 - \vec{p}_2). \tag{A.1}$$

and the dimension of the meson states in units of mass is $-\frac{3}{2}$. Under such convention, a single particle plane wave state in infinite volume with momentum $\vec{p}$ has the wave function:

$$\psi^{\infty}_{\vec{p}}(\vec{r}) \equiv {}_{\infty}\langle\vec{r}|\vec{p}\rangle_{\infty} = e^{i\vec{p}\cdot\vec{r}}. \tag{A.2}$$

Please note this is different from the relativistic convention:

$$\langle K^0(\vec{p}_1)|K^0(\vec{p}_2)\rangle = 2E(2\pi)^3\delta^3(\vec{p}_1 - \vec{p}_2), \tag{A.3}$$

where the dimension of the meson states in units of mass is -1.

In our finite volume lattice calculation, a single particle momentum eigenstate in finite volume

with momentum $\vec{p}_n$ will have the wave function:

$$\psi^V_{\vec{p}_n}(\vec{r}) \equiv {}_V\langle \vec{r}|\vec{p}_n\rangle_V = \frac{1}{\sqrt{L^3}} e^{i\vec{p}_n\cdot\vec{r}}, \tag{A.4}$$

where L^3 denotes the spacial volume and the corresponding normalization condition for the finite-volume states is given by:

$${}_V\langle \vec{p}_n|\vec{p_{n'}}\rangle_V = \delta_{n,n'}. \tag{A.5}$$

The dimension of the finite-volume meson states in units of mass is 0.

The relationship between the one particle state in infinite volume $|\vec{p}\rangle_\infty$ and the one particle state in finite volume $|\vec{p}\rangle_V$ with momentum $\vec{p}$ is given by:

$$|\vec{p}\rangle_\infty = \lim_{V\to\infty} \sqrt{L^3}|\vec{p}\rangle_V, \tag{A.6}$$

In each of the following sections, we will first present the dimension of a matrix element in the infinite volume so that we can obtain the appropriate powers of the lattice spacing a to multiply the results from the lattice calculation and then derive the corresponding finite-volume expression based on Equation A.6 which will be calculated on the lattice.

A.2 Dimension of three-point matrix elements

A.2.1 Dimension of three-point matrix elements with four-quark operators

In infinite volume, the dimension of the matrix element related to four-quark operators in units of mass, using ${}_\infty\langle\pi|Q_\pm(\vec{0},t)|K^0\rangle_\infty$ as an example, is given by:

$$\begin{aligned}\dim[{}_\infty\langle\pi|Q_\pm(\vec{0},t)|K^0\rangle_\infty] &= \dim[\text{quark field}]\times 4 + \dim[|K\rangle_\infty] + \dim[|\pi\rangle_\infty] \\ &= \frac{3}{2}\times 4 - \frac{3}{2} - \frac{3}{2} = 3,\end{aligned} \tag{A.7}$$

In our lattice calculation in a finite volume, we calculate ${}_V\langle\pi|\overline{Q}_\pm(t)|K^0\rangle_V$ with $\overline{Q}_\pm(t) = \int d^3x Q_\pm(\vec{x},t)$,

the dimension of the matrix element related to four-quark operators in mass unit, is given by:

$$\begin{aligned}\dim[{}_V\langle\pi|\overline{Q}_\pm(t)|K^0\rangle_V] &= \dim[\text{quark field}]\times 4 + \dim[\text{3D integral}] + \dim[|K\rangle_V] + \dim[|\pi\rangle_V] \\ &= \frac{3}{2}\times 4 - 3 + 0 + 0 = 3,\end{aligned} \tag{A.8}$$

where the "3D integral" refers to the integral we perform over the spacial volume for the operator at a specific time t. Using translation invariance, we can write:

$$\mathcal{Q}_\pm(\vec{0},t) \to \frac{1}{L^3}\int d^3x \mathcal{Q}_\pm(\vec{x},t) = \frac{1}{L^3}\overline{Q}_\pm(t). \tag{A.9}$$

Therefore using Equation A.6 and Equation A.9, the relationship between ${}_V\langle\pi|\overline{Q}_\pm(t)|K^0\rangle_V$ and ${}_\infty\langle\pi|\mathcal{Q}_\pm(\vec{0},t)|K^0\rangle_\infty$ is given by:

$${}_\infty\langle\pi|\mathcal{Q}_\pm(\vec{0},t)|K^0\rangle_\infty = (\sqrt{L^3})^2{}_V\langle\pi|\frac{1}{L^3}\overline{Q}_\pm(t)|K^0\rangle_V = {}_V\langle\pi|\overline{Q}_\pm(t)|K^0\rangle_V, \tag{A.10}$$

if the finite-volume corrections are negligible and neglected.

Thus, the physical matrix elements ${}_V\langle\pi|\overline{Q}_\pm|K^0\rangle_V$ on which we perform scaling tests are given by:

$${}_V\langle\pi|\overline{Q}_\pm|K^0\rangle_V = {}_V\langle\pi|\overline{Q}_\pm^{\text{lat}}|K^0\rangle_V \times (a^{-1})^3 \times Z_\pm, \tag{A.11}$$

where ${}_V\langle\pi|\overline{Q}_\pm^{\text{lat}}|K^0\rangle_V$ are values of matrix elements obtained from lattice calculations and $Z_\pm$ are the NPR factors calculated at the RI-SMOM scheme.

A.2.2 Dimension of three-point matrix elements with two-quark operators

We also introduced the two-quark operators $\bar{s}d$ and $\bar{s}\gamma_5 d$ with lower dimensions. In infinite volume, the dimension of three-point matrix element ${}_\infty\langle\pi|\bar{s}d(\vec{x}, t=0)|K^0\rangle_\infty$ is given by:

$$\begin{aligned}\dim[{}_\infty\langle\pi|\bar{s}d(\vec{x}, t=0)|K^0\rangle_\infty] &= \dim[|\pi\rangle_\infty] + \dim[\text{quark field}] \times 2 + \dim[|K\rangle_\infty] \\ &= -\frac{3}{2} + \frac{3}{2} \times 2 - \frac{3}{2} = 0.\end{aligned} \tag{A.12}$$

In our lattice calculation in a finite volume, the dimension of the matrix element of these two-quark operators in units of mass, using ${}_V\langle\pi|\int d^3x\bar{s}d(\vec{x}, t=0)|K^0\rangle_V$ as an example, is given by:

$$\begin{aligned}\dim[{}_V\langle\pi|\int d^3x\bar{s}d(\vec{x}, t=0)|K^0\rangle_V] &= \dim[|\pi\rangle_V] + \dim[|K\rangle_V] \\ &\quad + \left(\dim[\text{quark field}] \times 2 + \dim[\text{3D integral}]\right) \\ &= 0 + 0 + \frac{3}{2} \times 2 - 3 = 0.\end{aligned} \tag{A.13}$$

The relationship between ${}_V\langle\pi|\int d^3x\bar{s}d(\vec{x}, t=0)|K^0\rangle_V$ and ${}_\infty\langle\pi|\bar{s}d(\vec{x}, t=0)|K^0\rangle_\infty$ is given by:

$${}_\infty\langle\pi|\bar{s}d(\vec{x}, t=0)|K^0\rangle_\infty = (\sqrt{L^3})^2 {}_V\langle\pi|\frac{1}{L^3}\bar{s}d(t)|K^0\rangle_V = {}_V\langle\pi|\bar{s}d(t)|K^0\rangle_V, \tag{A.14}$$

if the finite-volume corrections are negligible and neglected.

Thus, the physical matrix element ${}_V\langle\pi|\int d^3x\bar{s}d(\vec{x}, t=0)|K^0\rangle_V$ on which we perform scaling tests are given by:

$${}_V\langle\pi|\int d^3x\bar{s}d(\vec{x}, t=0)|K^0\rangle_V = {}_V\langle\pi|\int d^3x\bar{s}d^{\text{lat}}(\vec{x}, t=0)|K^0\rangle_V \times (a^{-1})^0 \times Z_m, \tag{A.15}$$

where ${}_V\langle\pi|\int d^3x\bar{s}d^{\text{lat}}(\vec{x}, t=0)|K^0\rangle_V$ is the value of the matrix element obtained from lattice calculations and Z_m is the mass renormalization factor.

A.3 Dimension of four-point correlation functions

According to Equation 4.14 and the dimension analysis for the finite-volume three-point matrix elements as shown in Equation A.11, we obtain the dimension of the finite-volume single-integrated correlation functions $\mathcal{A}_{ij}^{S}(T)$ which is given by:

$$\begin{aligned}\dim[\mathcal{A}_{ij}^{S}(T)] &= \dim\left[\sum_{n} \frac{{}_V\langle\overline{K^0}|\overline{Q}_i^{'}|n\rangle_{VV}\langle n|\overline{Q}_j^{'}|K^0\rangle_V}{m_K - E_n}\right] \\ &= \dim[{}_V\langle n|\overline{Q}_j^{'}|K^0\rangle_V] \times 2 - \dim[m_K - E_n] = 3 \times 2 - 1 = 5,\end{aligned} \tag{A.16}$$

where $\overline{Q}_i^{'} = \int d^3Q_i'(\vec{x}, t = 0)$. We obtain the physical Δm_K by multiplying the contants k_{ij} obtained from the value of single-integrated correlation functions on the lattice $\mathcal{A}_{ij}^{S,\text{lat}}(T)$, as shown in Equation 4.25 by $(a^{-1})^5$:

$$\Delta m_K^{\text{phys}} = \frac{G_F^2}{2}\lambda_u^2\left[\sum_{i,j=1,2}(-2) \times C_i^{\text{lat}} C_j^{\text{lat}} k_{ij}\right] \times (a^{-1})^5. \tag{A.17}$$

and $\dim[\Delta m_K^{\text{phys}}] = \dim[\frac{G_F^2}{2}\lambda_u^2] + \dim[\mathcal{A}_{ij}^{S}(T)] = -4 + 5 = 1$ as expected.

Similarly, for the unintegrated correlation functions like for $\widetilde{G}_{ij}^{\text{sub}}(t)$ defined in Equation 4.22 , we have:

$$\begin{aligned}\dim[\widetilde{G}_{ij}^{\text{sub}}(t)] &= \dim\left[\sum_{n\neq n_l} {}_V\langle\overline{K^0}|\overline{Q}_i^{'}|n\rangle_{VV}\langle n|\overline{Q}_j^{'}|K^0\rangle_V e^{(m_K - E_n)t}\right] \\ &= \dim[{}_V\langle n|Q_j'|K^0\rangle_V] \times 2 = 3 \times 2 = 6.\end{aligned} \tag{A.18}$$

Thus the unintegrated correlation functions we plot in physical units, can be obtain from multiplying the values of the unintegrated correlation functions on the lattice $\widetilde{G}_{ij}^{\text{sub,lat}}(t)$ by $(a^{-1})^6$:

$$\widetilde{G}_{ij}^{\text{sub}}(t) = \widetilde{G}_{ij}^{\text{sub,lat}}(t) \times (a^{-1})^6 \times Z_{ij}, \tag{A.19}$$

where Z_{ij} are the NPR factors calculated at the RI-SMOM scheme.

Appendix B: Input parameters used in Δm_K calculation

G_F	$1.16637 \times 10^{-5}\text{GeV}^{-2}$
m_t	172.2 GeV
m_W	80.4 GeV
m_Z	91.1876 GeV
λ_u	0.2196
λ	0.2253(7)

Table B.1: Input parameters used in Δm_K calculation.

λ_u is calculated using the Wolfenstein parametrization. To order $O(\lambda^5)$, we have:

$$\lambda_u = \lambda - \frac{\lambda^3}{2} - \frac{\lambda^5}{8}, \tag{B.1}$$

For the value of λ_u listed in Table B.1, following our earlier calculations, we calculate it up to $O(\lambda^3)$:

$$\lambda_u = \lambda - \frac{\lambda^3}{2}. \tag{B.2}$$

Appendix C: Diagrams

In this appendix, we show each diagram that is computed and give its type and assign an additional numeric label that will be used in Appendix D to identify it.

C.1 Four-point diagrams

Following the earlier calculation of Δm_K[16][26], we obtain the four-point diagrams listed in this section using the $\Delta S = 1$ weak operators Q_1 and Q_2:

$$Q_1^{qq'} = (\bar{s}_i \gamma^\mu (1-\gamma_5) d_i)(\bar{q}_j \gamma^\mu (1-\gamma_5) q'_j), \tag{C.1}$$

$$Q_2^{qq'} = (\bar{s}_i \gamma^\mu (1-\gamma_5) q'_i)(\bar{q}_j \gamma^\mu (1-\gamma_5) d_j), \tag{C.2}$$

where we have written the operator Q_2 in a color-diagonal form by taking advantage of the Fierz identity. In this way, the pair of lines joined to a single dot in the diagrams shown below corresponds to those quark propagators whose color and spin indices are contracted.

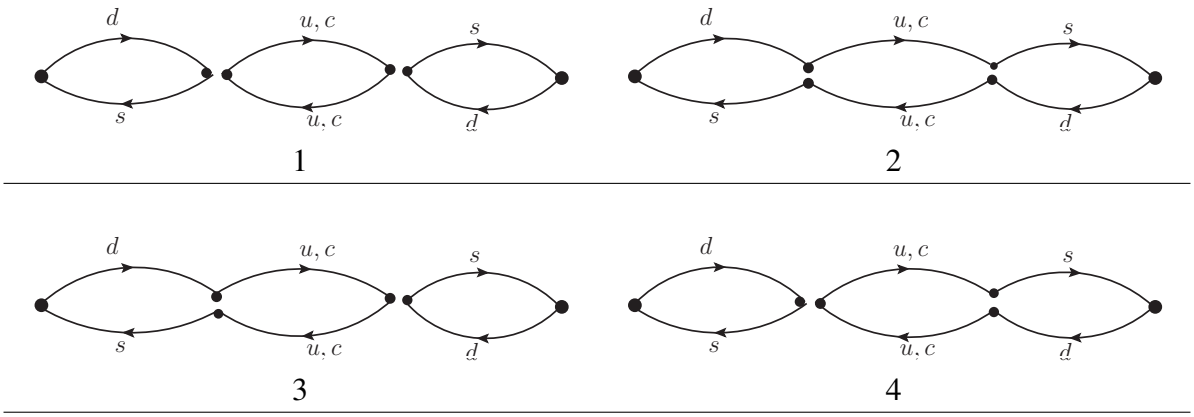

Figure C.1: Diagrams for type-1 contractions[26]. The single dots correspond to the K^0 and $\overline{K^0}$ operators including a γ_5 matrix. The paired dots correspond to the weak four-quark operators. The pair of lines joined to a single dot corresponds to those quark propagators whose color and spin indices are contracted with, in the case of spin indices, only factors of γ_μ or $\gamma_\mu\gamma_5$ in between.

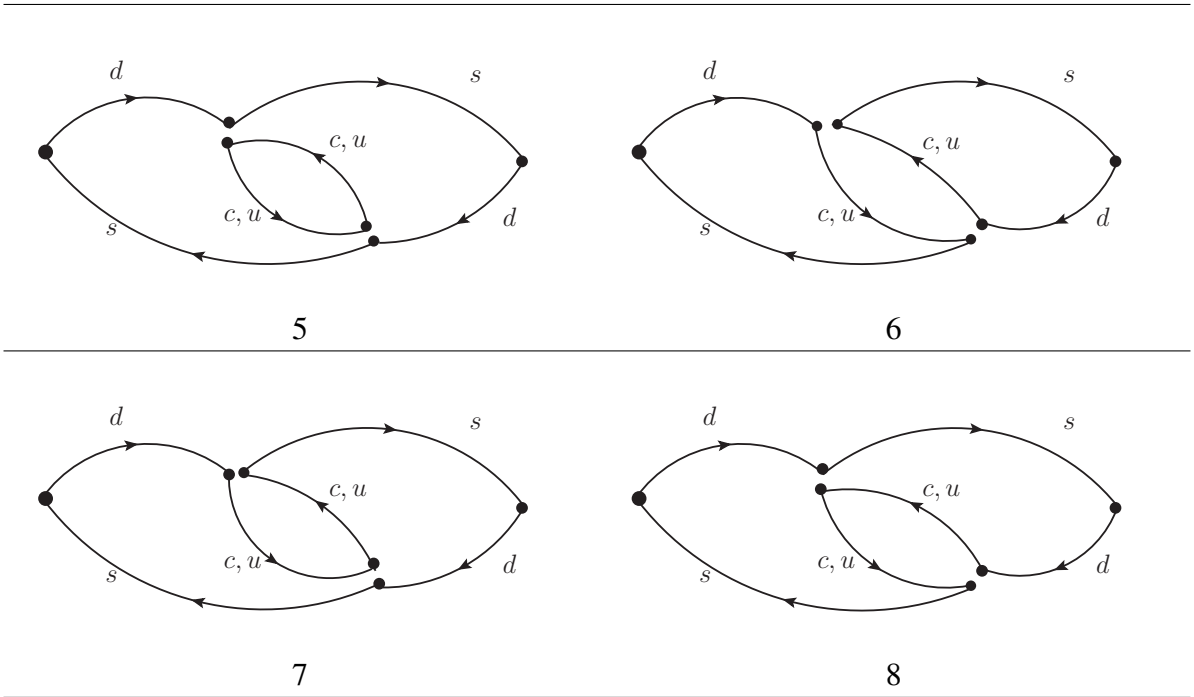

Figure C.2: Diagrams for type-2 contractions[26]. The single dots correspond to the K^0 and $\overline{K^0}$ operators while the paired dots correspond to the weak four-quark operators. The conventions used here are the same as those explained in the caption of Figure C.1.

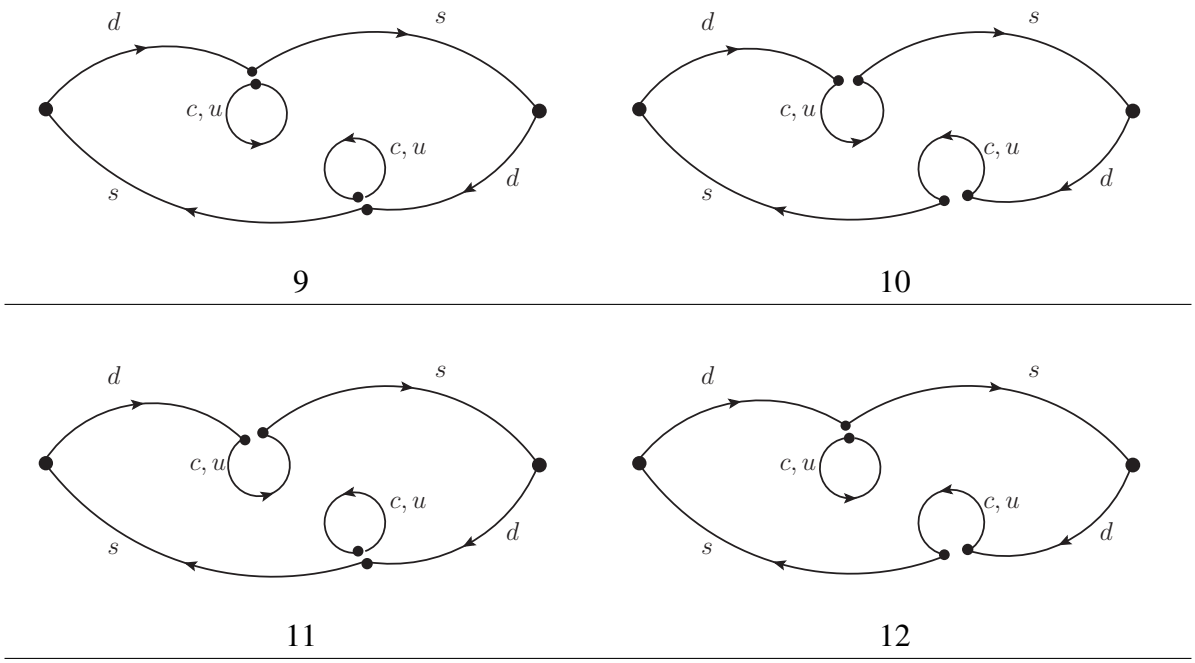

Figure C.3: Diagrams for type-3 contractions[26]. The single dots correspond to the K^0 and $\overline{K^0}$ operators while the paired dots correspond to the weak four-quark operators.The conventions used here are the same as those explained in the caption of Figure C.1.

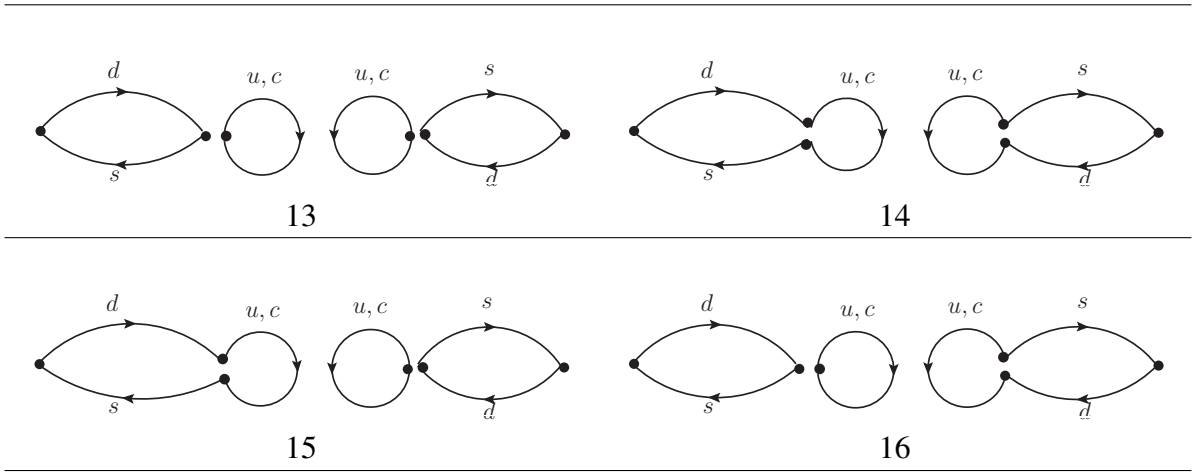

Figure C.4: Diagrams for type-4 contractions[26]. The single dots correspond to the K^0 and $\overline{K^0}$ operators while the paired dots correspond to the weak four-quark operators. The conventions used here are the same as those explained in the caption of Figure C.1.

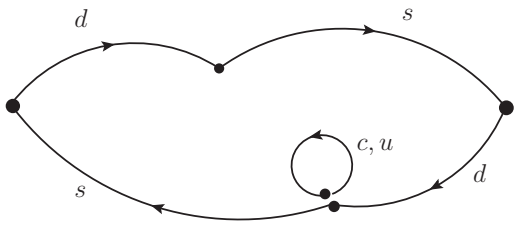

17

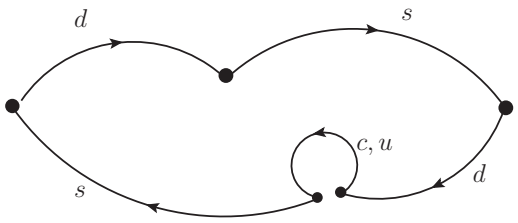

18

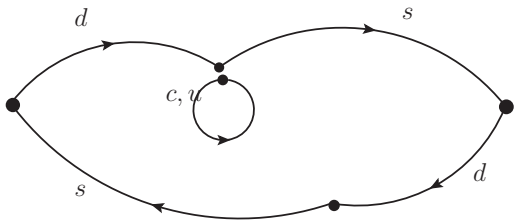

19

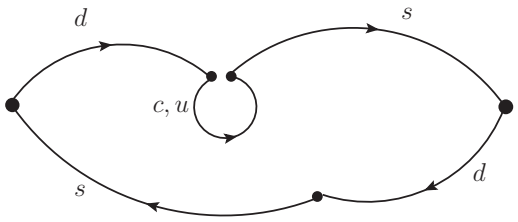

20

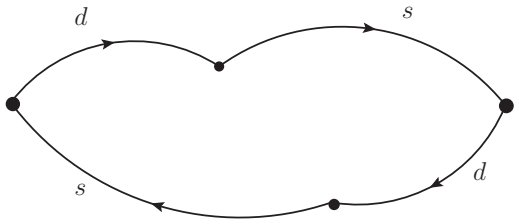

21

Figure C.5: Diagrams for type-3-like mixed contractions[26]. The single dots at the left and right ends correspond to the K^0 and $\overline{K^0}$ operators while the paired dots correspond to the weak four-quark operators. The single dots in the middle correspond to the $\overline{s}d$ or $\overline{s}\gamma_5 d$ operator. The conventions used here are the same as those explained in the caption of Figure C.1.

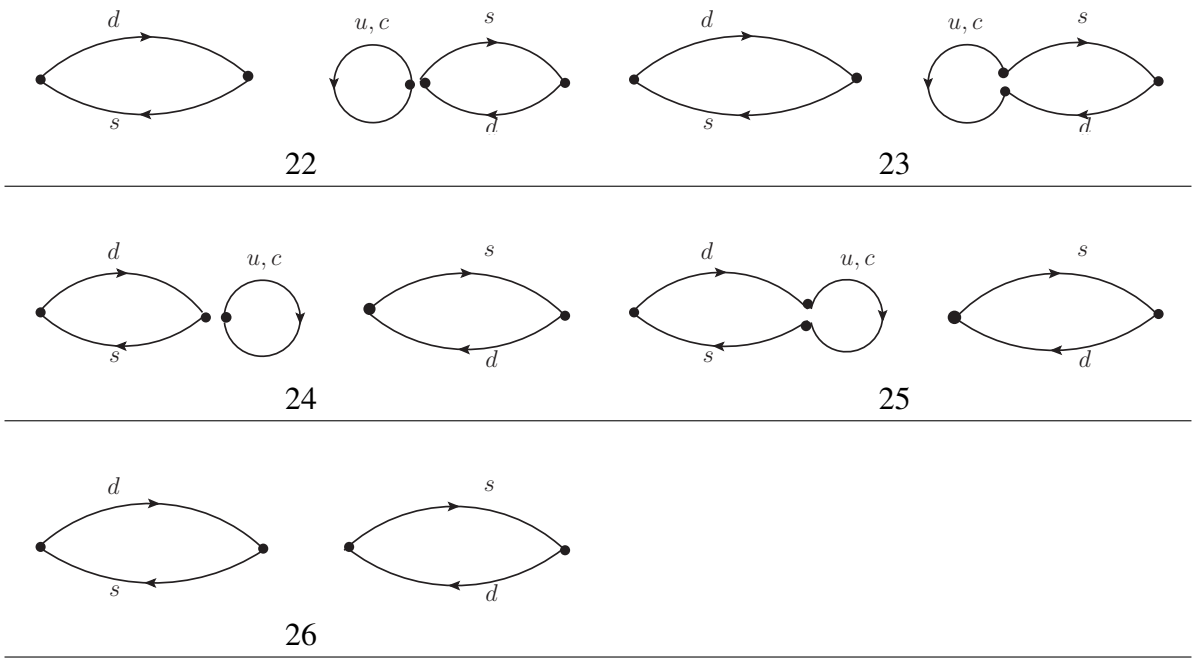

Figure C.6: Diagrams for type-4-like mixed contractions[26]. The single dots at the left and right ends correspond to the K^0 and $\overline{K^0}$ operators while the paired dots correspond to the weak four-quark operators. The single dots in the middle correspond to the $\bar{s}d$ or $\bar{s}\gamma_5 d$ operator. The conventions used here are the same as those explained in the caption of Figure C.1.

C.2 Three-point diagrams

In this section, we will show the diagrams which contribute to the three-point correlators from which we need to extract light state matrix elements. For the kaon to pion, kaon to eta and kaon to vacuum diagrams, we used the the operator Q_2 written in a color-diagonal form by taking advantage of the Fierz identity and therefore, in the diagrams shown in this section the pair of lines joined to a single dot correspond to those quark propagators whose color and spin indices are contracted. Because kaon to two-pion diagrams are calculated without writing the operator Q_2 in a color-diagonal form in our earlier Δm_K calculation [16], we will present kaon to two-pion diagrams separately in Section C.3.

In Figure C.7, we show all the diagrams contribute to the kaon to pion three-point correlators. The kaon to eta three-point point correlators have more diagrams in addition to the diagrams which contribute to the kaon to pion three-point correlators. Therefore in Figure C.8, we show the diagrams which contribute to the kaon to eta three-point correlators in addition to the ones shown in Figure C.7.

In Figure C.9, we show all the diagrams which contribute to the kaon to vacuum three-point correlators. The diagram labeled by index 17 is a two-point diagram but we put it with other kaon to vacuum three-point diagrams because it will be subtracted in the calculations of the kaon to vacuum three-point correlators. In Figure C.10, we show all the diagrams which contribute to the three-point B_K correlators which we also calculate along with other three-point diagrams.

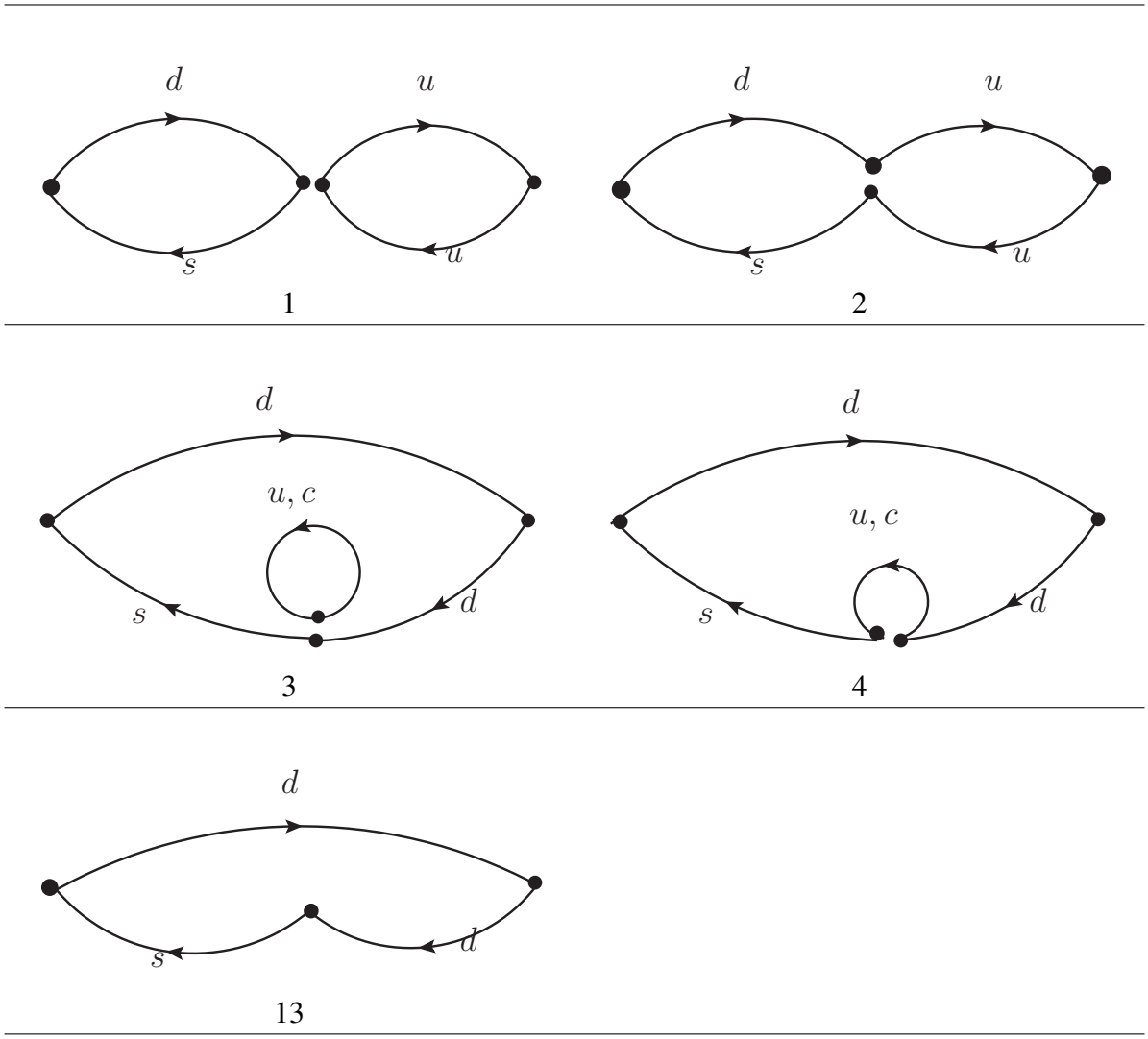

Figure C.7: Diagrams for three-point K $\rightarrow \pi$ correlators. The single dots at the left and right ends correspond to the K^0 and π operators while the paired dots correspond to the weak four-quark operators. The single dot in the middle of the diagram 13 corresponds to the $\overline{s}d$ operator.

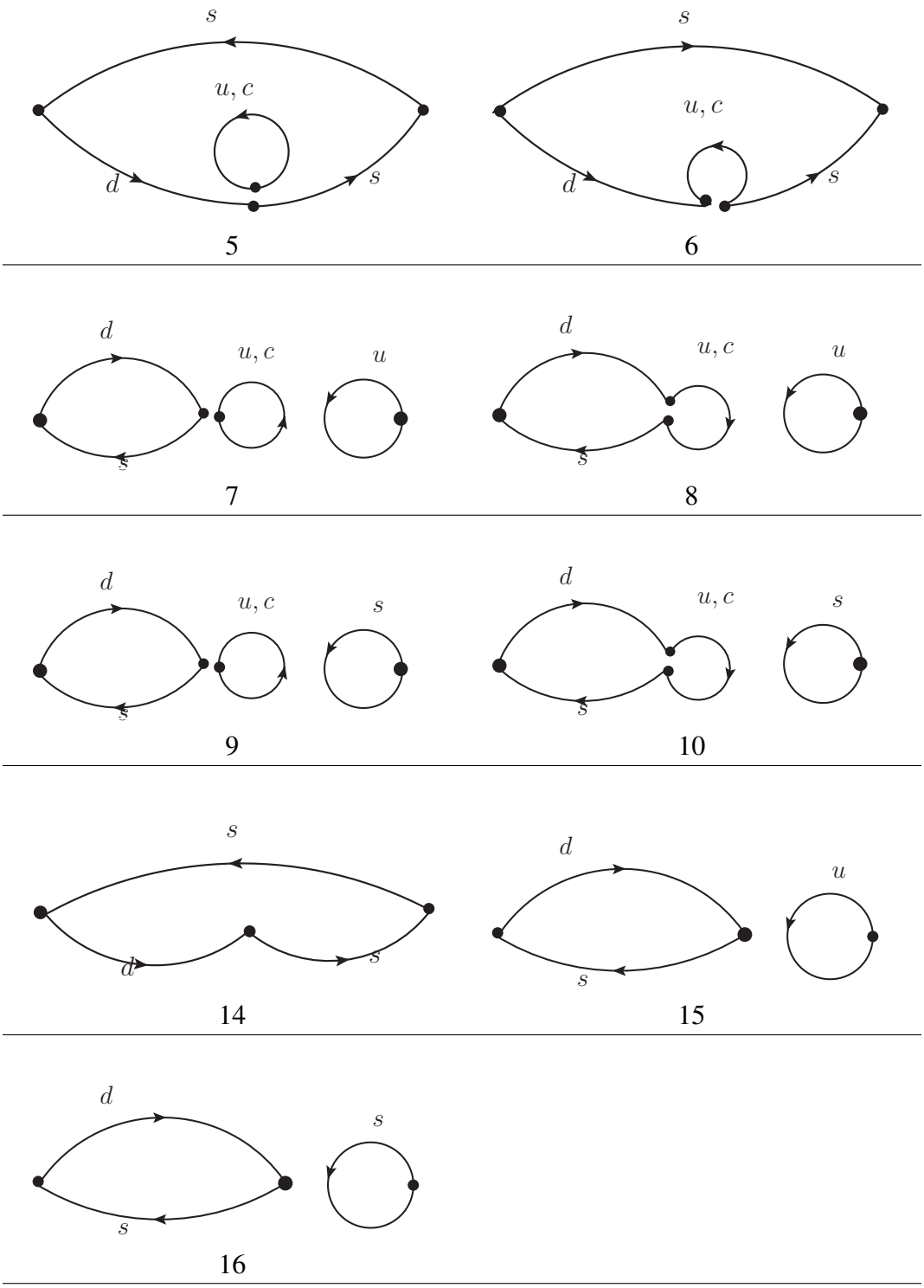

Figure C.8: Diagrams for three-point K $\to \eta$ correlators in addition to the ones shown in Figure C.7. The single dots at the left and right ends correspond to the K^0 and η operators while the paired dots correspond to the weak four-quark operators. Diagram 13 has been included in Figure C.7. The single dot in the middle of the diagrams 14-16 corresponds to the $\overline{s}d$ operator.

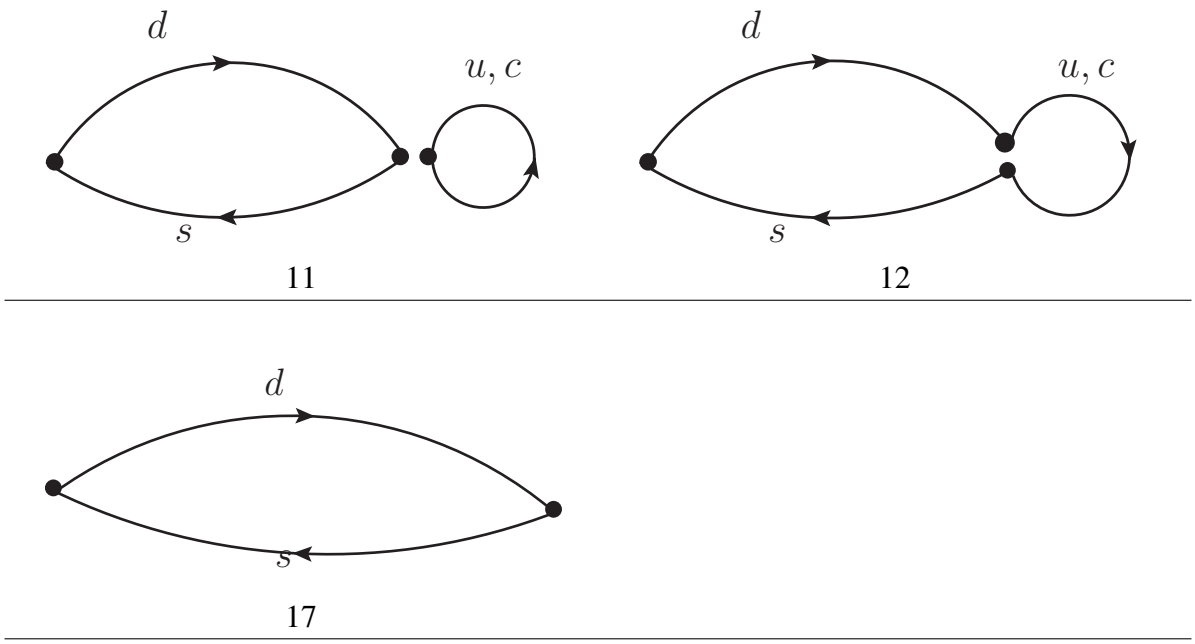

Figure C.9: Diagrams for three-point K to vacuum correlators. The single dots at the left end correspond to the K^0 operator while the paired dots correspond to the weak four-quark operators. The single dot on the right in the diagram 17 corresponds to the $\bar{s}\gamma_5 d$ operator. Please note the diagram 17 is a two-point diagram but we put it here along with other kaon to vacuum three-point diagrams because it will be subtracted in the calculation of the kaon to vacuum three-point correlators.

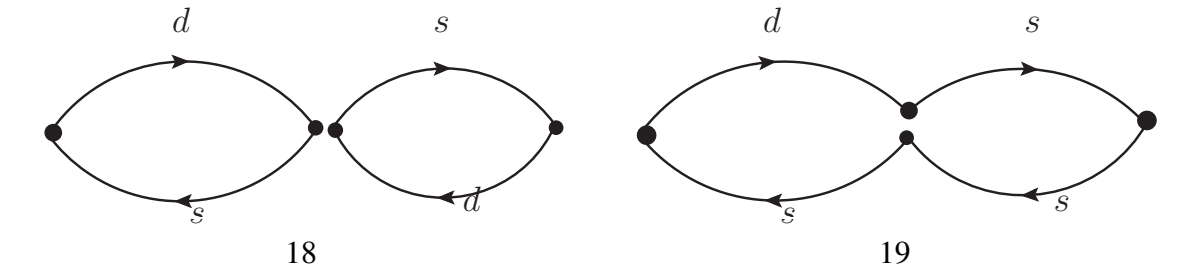

Figure C.10: Diagrams for three-point B_K correlators. The single dots at the left and right ends correspond to the K^0 and $\overline{K^0}$ operators while the paired dots in the middle correspond to the weak four-quark operators.

C.3 Three-point diagrams: kaon to two-pion diagrams

The kaon to two-pion diagrams are calculated without writing the operator Q_2 in a color-diagonal form in our earlier Δm_K calculation [16], and we follow the same convention for our kaon to two-pion diagrams. In Figure C.11, we list the kaon to two-pion diagrams in a different style as in the previous sections: the pairs of vertices with a cross correspond to the weak four-quark operators; for a diagram having only solid lines, the pair of solid lines joined to the vertices correspond to those quark propagators whose color and spin indices are contracted and for a diagram having dashed lines, the pair of solid lines joined to the vertices correspond to those quark propagators whose spin indices are contracted and the color contractions are denoted by the dashed lines.

Because we have introduced $\overline{s}\gamma_5 d$ operators, there are mix diagrams as well for kaon to two-pion correlators and we list them in Figure C.12.

If we write the operator Q_2 in a color-diagonal form, we will find in Figure C.11, Diagram 2 multiplied by -1 is equivalent to Diagram 3 and Diagram 4 multiplied by -1 is equivalent to Diagram 1. The -1 comes from the difference of number of loops between the equivalent diagrams. In Figure C.13, we also list the diagrams equivalent to to Diagrams 6, 8 and 10 in Figure C.11 under the Fierz transformation. In the future calculations, we can equivalently calculate the kaon to two-pion correlators with the operator Q_2 in a color-diagonal form as well.

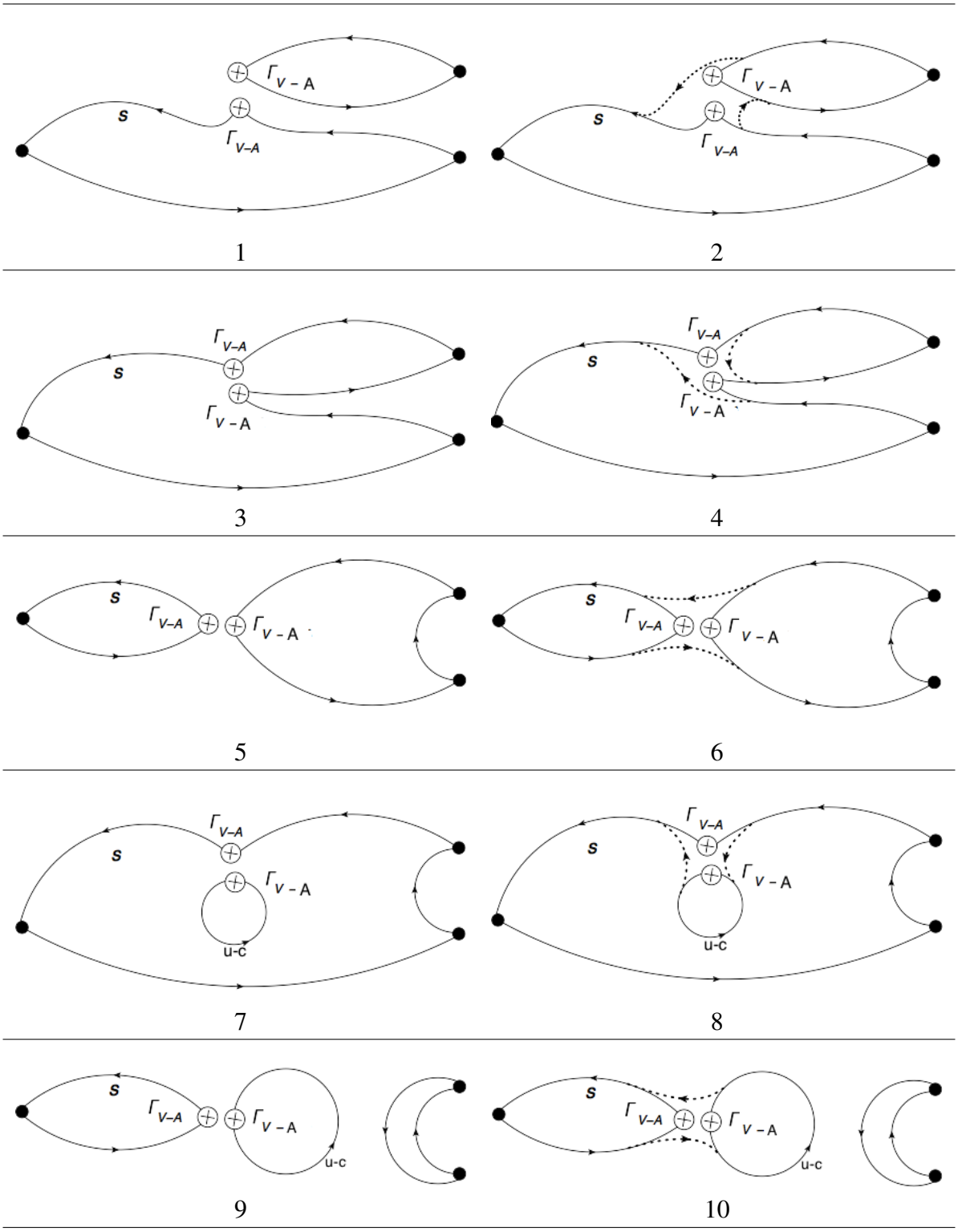

Figure C.11: Diagrams for three-point K to $\pi\pi$ correlators. The single dots at the left end correspond to the K^0 and the double dots at the right end correspond to the $\pi\pi$ operators. The pairs of vertices with a cross correspond to the weak four-quark operators. The dashed lines denote the color contractions.

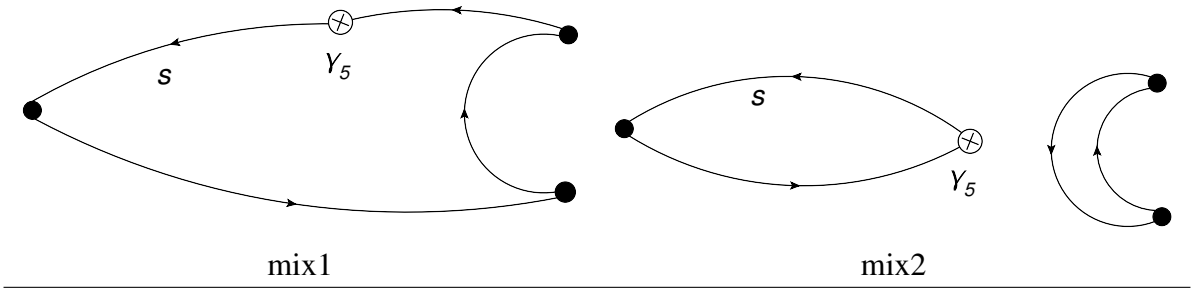

mix1 mix2

Figure C.12: The mixed diagrams for three-point K to $\pi\pi$ correlators. The single dots at the left end correspond to the K^0 and the double dots at the right end correspond to the $\pi\pi$ operators. The vertex with a cross and labeled by γ_5 correspond to the $\bar{s}\gamma_5 d$ operator.

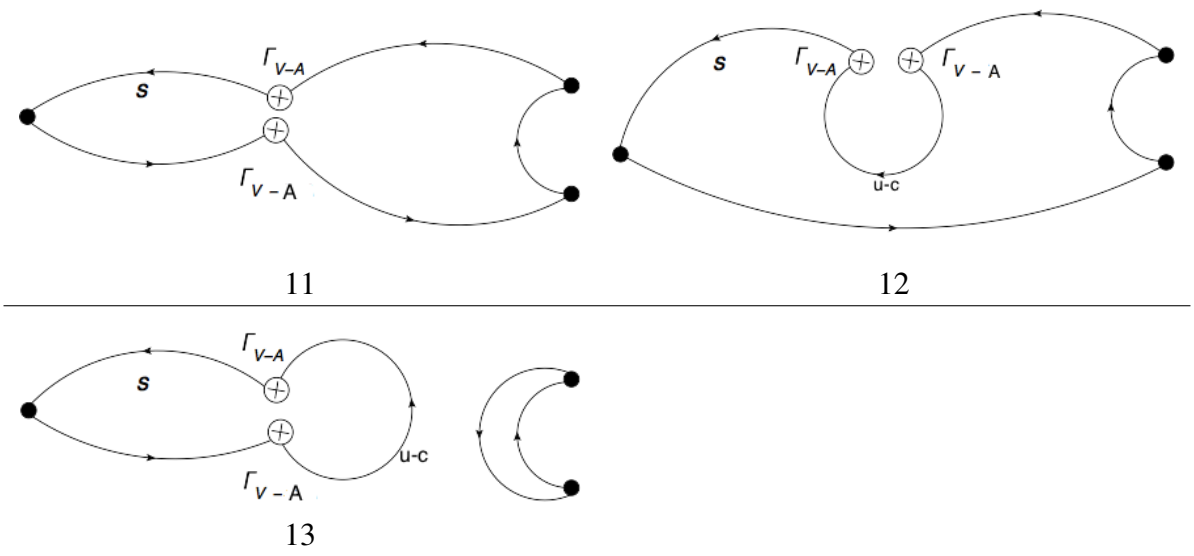

11 12 13

Figure C.13: Extra diagrams which can be used for three-point K to $\pi\pi$ correlators. The single dots at the left end correspond to the K^0 and the double dots at the right end correspond to the $\pi\pi$ operators. Diagrams 11, 12, and 13 are equivalent to Diagrams 6, 8 and 10 in Figure C.11 under the Fierz transformation and can be used in the future calculations. The pairs of vertices with a cross correspond to the weak four-quark operators. The dashed lines denotes the color contractions.

C.4 Two-point diagrams

In Figure C.14, we list the two-point diagrams related to the two-point pion, kaon, and eta meson correlators.

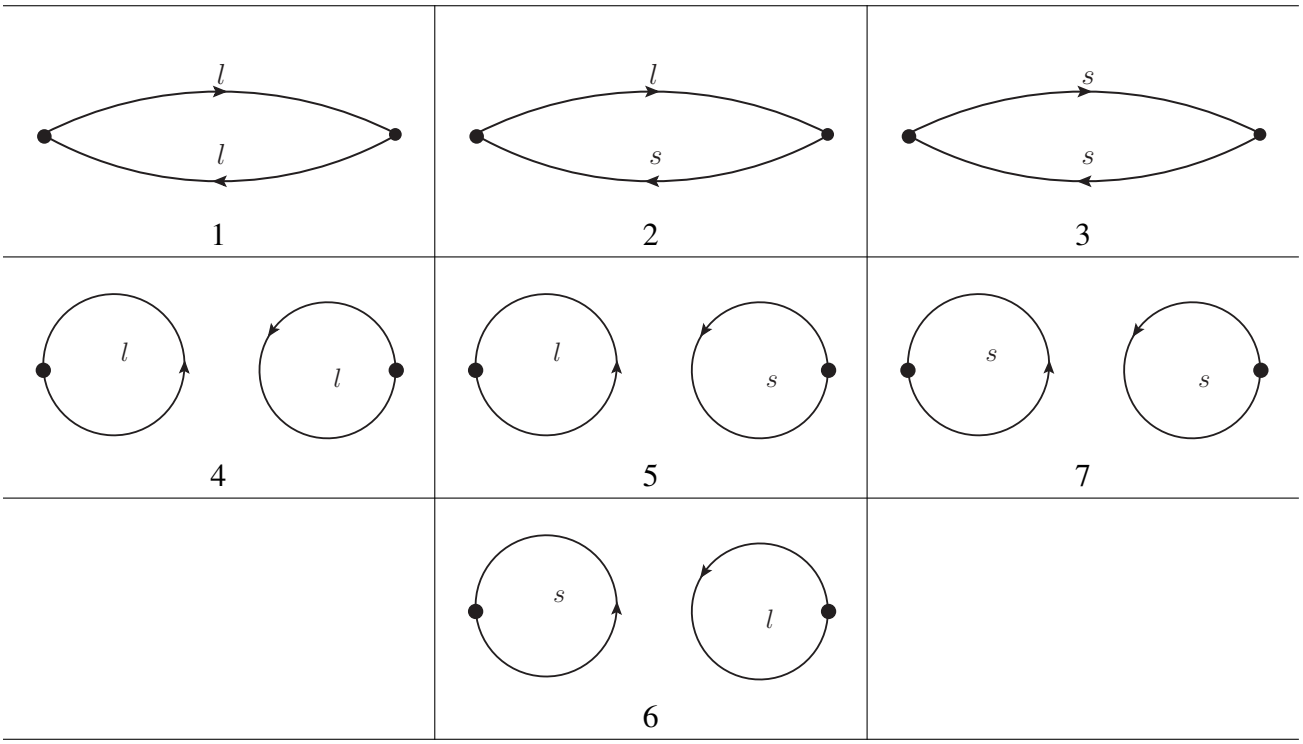

Figure C.14: Diagrams for two-point correlators. The single dots at the left and right ends correspond to the meson interpolating operators. $\pi - \pi$ two-point diagrams are shown in Figure C.15.

In Figure C.15, we list the two-point diagrams related to the two-pion meson correlators. We also need to remove the $\langle 0|\pi\pi\rangle$ contribution from the two-pion meson correlators. The diagram related to the two-pion to vacuum is shown in Figure C.16.

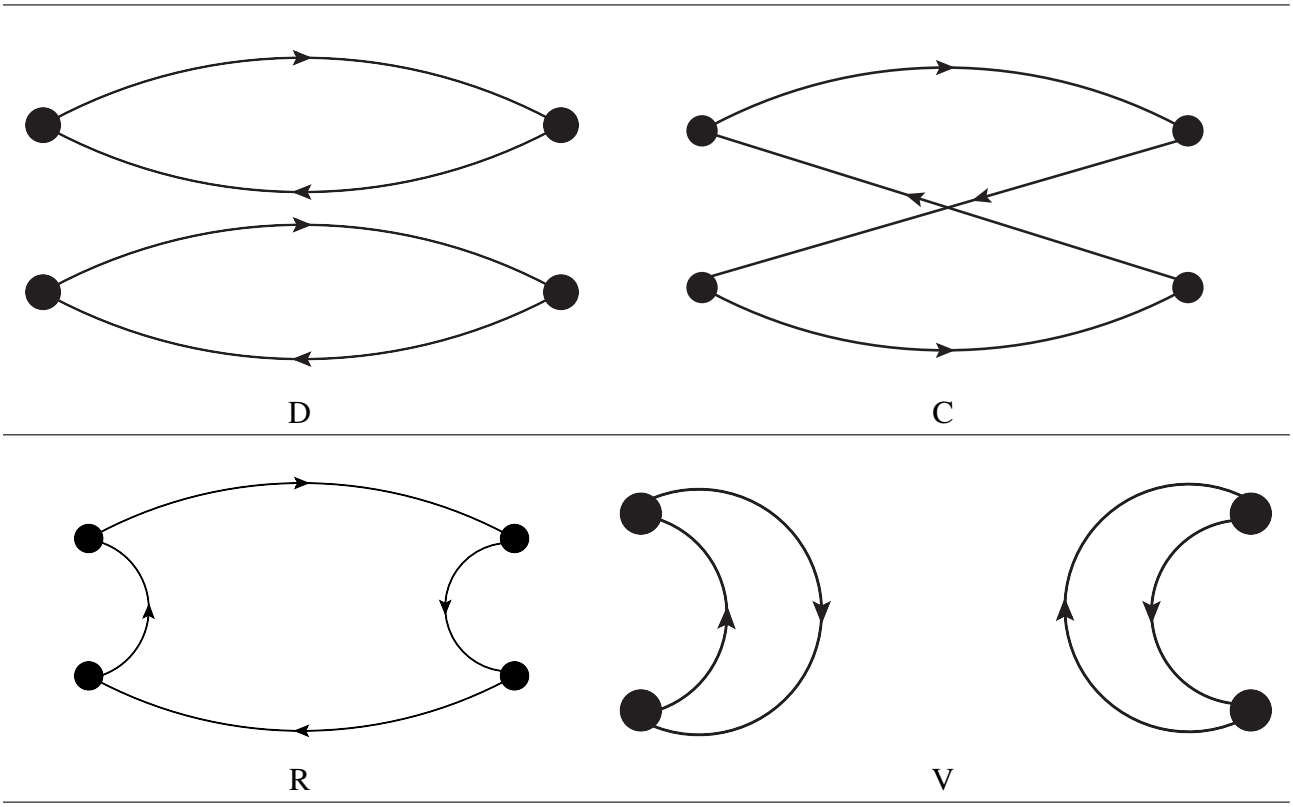

Figure C.15: Diagrams for two-point $\pi - \pi$ correlators. The double dots at the left and right ends correspond to the two pion interpolating operators separated by 6 lattice units in time.

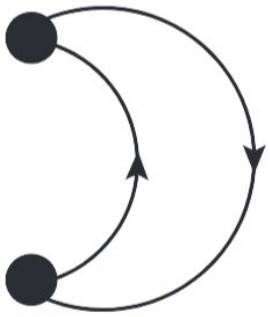

Figure C.16: $|\pi\pi\rangle \rightarrow |0\rangle$ diagram to be subtracted from the two-point $\pi - \pi$ diagram V. The double dots correspond to the two pion interpolating operators separated by 6 lattice units in time.

Appendix D: Contractions

In this chapter, we will list all the contractions we use in our Δm_K calculations. All the indices and labels of the diagrams can be found in the figures shown in Appendix C. The expressions for the time dependence of two-point, three-point and four-point correlators are described in Chapter 4.

D.1 Two-point contractions

The two-point diagrams and their indices can be found in Section C.4 and the contractions for two-point correlation functions are listed below:

$$C_{\pi}^{2\mathrm{pt}}(t) = \textcircled{1} \tag{D.1}$$

$$C_{K}^{2\mathrm{pt}}(t) = \textcircled{2} \tag{D.2}$$

$$C_{\eta_8}^{2\mathrm{pt}}(t) = \frac{1}{6}\left(2\times\textcircled{1}+4\times\textcircled{3}-4\times\textcircled{4}-4\times\textcircled{5}+4\times\textcircled{6}+4\times\textcircled{7}\right) \tag{D.3}$$

$$C_{\eta_1}^{2\mathrm{pt}}(t) = \frac{1}{3}\left(2\times\textcircled{1}+\textcircled{3}-4\times\textcircled{4}-\textcircled{5}-2\times\textcircled{6}-2\times\textcircled{7}\right) \tag{D.4}$$

$$C_{\pi\pi_{I=2}}^{2\mathrm{pt}}(t) = 2\times\left(\textcircled{D}-\textcircled{C}\right) \tag{D.5}$$

$$C_{\pi\pi_{I=0}}^{2\mathrm{pt}}(t) = 2\times\textcircled{D}+\textcircled{C}-6\times\textcircled{R}+3\times\textcircled{V'}, \tag{D.6}$$

where we subtract $\langle 0|\pi\pi\rangle$ contribution shown in Figure C.16 from the diagram (V) to obtain (V'):

$$\textcircled{V'} = \textcircled{V} - \textcircled{p2v}\times\textcircled{p2v}. \tag{D.7}$$

D.2 Three-point contractions

For three-point diagrams, we follow the convention of our earlier Δm_K calculations and assign "-1" explicitly to the diagrams with the even number of loops and put them within a pair of parenthesis. The diagrams labeled by circled indices themselves do not have the signs included. Please note this convention looks different from the common convention used where the diagrams with the odd number of loops are assigned with an extra factor of "-1" due to the anti-commutation of the fermions but is actually consistent with the common convention. This difference is caused by the fact that our definition of interpolating operators and the way we perform contractions. For example, we have the kaon interpolating operator $O_{K^0} = i(\overline{d}\gamma_5 s)$ and the pion interpolating operator $O_{\pi^0} = i(\overline{u}\gamma_5 u - \overline{d}\gamma_5 d)/\sqrt{2}$ in our kaon to pion three-point correlator calculations. With such a source and a sink, there will be an extra minus sign, $i^2 = -1$, because we do not include the minus sign in the contractions.

The three-point diagrams and their indices can be found in Section C.2 and the contractions for three-point correlation functions are listed below:

$$C^{Q_1}_{K\to\pi}(\Delta,t) = \frac{1}{\sqrt{2}}[(-\textcircled{1}) - (-\textcircled{3})] \tag{D.8}$$

$$C^{Q_2}_{K\to\pi}(\Delta,t) = \frac{1}{\sqrt{2}}[\textcircled{2} - \textcircled{4}] \tag{D.9}$$

$$C^{\bar{s}d}_{K\to\pi}(\Delta,t)\rangle = \textcircled{13} \tag{D.10}$$

$$C^{Q_1}_{K\to\eta}(\Delta,t) = \frac{1}{\sqrt{6}}[(-\textcircled{1}) + (-\textcircled{3}) - 2\times(-\textcircled{5}) + 2\times\textcircled{7} - 2\times\textcircled{9}] \tag{D.11}$$

$$C^{Q_2}_{K\to\eta}(\Delta,t) = \frac{1}{\sqrt{6}}[\textcircled{2} + \textcircled{4} - 2\times\textcircled{6} + 2\times(-\textcircled{8}) - 2\times(-\textcircled{10})] \tag{D.12}$$

$$C^{\bar{s}d}_{K\to\eta}(\Delta,t) = \frac{1}{\sqrt{6}}[\textcircled{13} - 2\times\textcircled{14} - 2\times\textcircled{15} + 2\times\textcircled{16}] \tag{D.13}$$

$$C^{Q_1}_{K\to 0}(\Delta,t) = i\textcircled{11} \tag{D.14}$$

$$C^{Q_2}_{K\to 0}(\Delta,t) = -i\textcircled{12} \tag{D.15}$$

$$C^{\bar{s}\gamma_5 d}_{K\to 0}(\Delta,t) = -i\textcircled{17} \tag{D.16}$$

For the K $\to \pi\pi_{I=0}$ three-point correlation functions, we have separate diagrams and indices shown in Figures C.11. Because we have introduced $\bar{s}\gamma_5 d$ operator, we have mixed diagrams in K $\to \pi\pi_{I=0}$ contractions shown in Figure C.12. We include the mixed diagrams and first combine them with a few diagrams with the similar topologies:

$$(-\text{7'}) = (-\text{7}) - c_{\text{p1}}\,\text{mix1} \tag{D.17}$$

$$(-\text{8'}) = (-\text{8}) - c_{\text{p2}}\,\text{mix1} \tag{D.18}$$

$$\text{9'} = \text{9} - c_{\text{p1}}(-\text{mix2}) \tag{D.19}$$

$$\text{10'} = \text{10} - c_{\text{p2}}(-\text{mix2}) \tag{D.20}$$

Then we have contractions:

$$C^{Q_1'}_{K\to\pi\pi_{I=0}}(\Delta,\delta) = \frac{i}{\sqrt{3}}[(-\text{1}) - 2\times\text{3} - 3\times(-\text{5}) - 3\times(-\text{7'}) - 3\times\text{9'}] \tag{D.21}$$

$$C^{Q_2'}_{K\to\pi\pi_{I=0}}(\Delta,\delta) = \frac{i}{\sqrt{3}}[(-\text{2}) - 2\times\text{4} - 3\times(-\text{6}) - 3\times(-\text{8'}) - 3\times\text{10'}]. \tag{D.22}$$

For the K $\to \pi\pi_{I=2}$ three-point correlation functions, there is no mixed diagram involved and the contractions are:

$$C^{Q_1}_{K\to\pi\pi_{I=2}}(\Delta,\delta) = -i\sqrt{\frac{2}{3}}[(-\text{1}) + \text{3}] \tag{D.23}$$

$$C^{Q_2}_{K\to\pi\pi_{I=2}}(\Delta,\delta) = -i\sqrt{\frac{2}{3}}[(-\text{2}) + \text{4}]. \tag{D.24}$$

Using the Fierz transformation, we can find:

$$\text{(3)} = -\text{(2)} \tag{D.25}$$

$$\text{(4)} = -\text{(1)} \tag{D.26}$$

$$\text{(11)} = -\text{(6)} \tag{D.27}$$

$$\text{(12)} = -\text{(8)} \tag{D.28}$$

$$\text{(13)} = -\text{(10)} \tag{D.29}$$

and therefore expect:

$$C^{Q_1}_{K\to\pi\pi_{I=2}}(\Delta,\delta) = -i\sqrt{\frac{2}{3}}[(-\text{(1)}) + \text{(3)}] = C^{Q_2}_{K\to\pi\pi_{I=2}}(\Delta,\delta) = -i\sqrt{\frac{2}{3}}[(-\text{(2)}) + \text{(4)}], \tag{D.30}$$

$$C^{Q'_2}_{K\to\pi\pi_{I=0}}(\Delta,\delta) = \frac{i}{\sqrt{3}}[(-\text{(2)}) - 2\times\text{(4)} - 3\times\text{(11)} - 3\times\text{(12')} + 3\times\text{(13')}]. \tag{D.31}$$

where (12') and (13') are given by:

$$\text{(12')} = \text{(12)} - c_{\text{p2}}\text{(mix1)}, \tag{D.32}$$

$$\text{(13')} = \text{(13)} - c_{\text{p2}}(-\text{(mix2)}). \tag{D.33}$$

D.3 Four-point contractions

For four-point diagrams, we follow the convention of our earlier Δm_K calculations and assign "-1" explicitly to the diagrams with the even number of loops and put them within a pair of parenthesis. The diagrams labeled by circled indices themselves do not have the signs included. Please note this convention looks different from the common convention used where the diagrams with the odd number of loops are assigned with an extra factor of "-1" due to the anti-commutation of

the fermions but is actually consistent with the common convention. This difference is caused by the fact that our definition of interpolating operators and the way we perform contractions. For example, we have the kaon interpolating operator $O_{K^0} = i(\overline{d}\gamma_5 s)$ in our four-point correlator calculations. With such a kaon source and a kaon sink, there will be an extra minus sign, $i^2 = -1$, because we do not include the minus sign in the contractions.

For the mixed diagrams, we use the subscripts "$\overline{s}\gamma_5 d$" and "$\overline{s}d$" to denote lower-dimensional operators appeared in the diagrams. We use $\widetilde{G}_{ij}(\delta)$ to denote the four-point correlation functions with weak operators Q'_i and Q'_j with $i, j = 1, 2$ and the time difference between the two weak operators is δ. The contractions shown below have been compared and found agreed with earlier theses[16][26].

$$
\begin{aligned}
\widetilde{G}_{11}(\delta) = {} & [\textcircled{1} + (-\textcircled{5}) + \textcircled{9} + (-\textcircled{13})] \\
& - c_{\mathrm{p1}}[(-\textcircled{17}) + (-\textcircled{19}) + \textcircled{22} + \textcircled{24}]_{\overline{s}\gamma_5 d} + c_{\mathrm{p1}}^2[\textcircled{21} + (-\textcircled{26})]_{\overline{s}\gamma_5 d} \\
& - c_{\mathrm{s1}}[(-\textcircled{17}) + (-\textcircled{19}) + \textcircled{22} + \textcircled{24}]_{\overline{s}d} + c_{\mathrm{s1}}^2[\textcircled{21} + (-\textcircled{26})]_{\overline{s}d},
\end{aligned}
\tag{D.34}
$$

$$
\begin{aligned}
\widetilde{G}_{22}(\delta) = {} & [\textcircled{2} + (-\textcircled{6}) + \textcircled{10} + (-\textcircled{14})] \\
& - c_{\mathrm{p2}}[\textcircled{18} + \textcircled{20} + (-\textcircled{23}) + (-\textcircled{25})]_{\overline{s}\gamma_5 d} + c_{\mathrm{p2}}^2[\textcircled{21} + (-\textcircled{26})]_{\overline{s}\gamma_5 d} \\
& - c_{\mathrm{s2}}[\textcircled{18} + \textcircled{20} + (-\textcircled{23}) + (-\textcircled{25})]_{\overline{s}d} + c_{\mathrm{s2}}^2[\textcircled{21} + (-\textcircled{26})]_{\overline{s}d},
\end{aligned}
\tag{D.35}
$$

$$
\begin{aligned}
\widetilde{G}_{12}(\delta) = {} & [(-\textcircled{3}) + \textcircled{7} + (-\textcircled{11}) + \textcircled{15}] \\
& + [(-\textcircled{4}) + \textcircled{8} + (-\textcircled{12}) + \textcircled{16}] \\
& - c_{\mathrm{p2}}[(-\textcircled{17}) + (-\textcircled{19}) + \textcircled{22} + \textcircled{24}]_{\overline{s}\gamma_5 d} - c_{\mathrm{p1}}[\textcircled{18} + \textcircled{20} + (-\textcircled{23}) + (-\textcircled{25})]_{\overline{s}\gamma_5 d} \\
& + 2c_{\mathrm{p1}}c_{\mathrm{p2}}[\textcircled{21} + (-\textcircled{26})]_{\overline{s}\gamma_5 d} \\
& - c_{\mathrm{s2}}[(-\textcircled{17}) + (-\textcircled{19}) + \textcircled{22} + \textcircled{24}]_{\overline{s}d} - c_{\mathrm{s1}}[\textcircled{18} + \textcircled{20} + (-\textcircled{23}) + (-\textcircled{25})]_{\overline{s}d} \\
& + 2c_{\mathrm{s1}}c_{\mathrm{s2}}[\textcircled{21} + (-\textcircled{26})]_{\overline{s}d}.
\end{aligned}
\tag{D.36}
$$

Appendix E: Analytic free-field calculation with free domain wall fermion propagators

E.1 Analytic free DWF propagators in coordinate space

On a lattice of size $L_x \times L_y \times L_z \times L_t$ with lattice spacing a, the analytic expression for a four-dimensional free DWF propagator in momentum space with the size in fifth dimension $L_s \to \infty$ is given by [27]:

$$S_q(p) = \frac{-i\gamma_\mu \overline{p}_\mu - m_f(1 - We^{-\alpha})}{(We^{\alpha} - 1) + m_f^2(1 - We^{-\alpha})}, \tag{E.1}$$

where $\overline{p}_\mu = \eta \sin(p_\mu a), W = (1 - M) + r\eta \sum_\mu (1 - \cos(p_\mu a)), \eta = \frac{a_5}{a}$. And α is given by:

$$2\cosh\alpha = \frac{1 + W^2 + x}{W}, \tag{E.2}$$

where $x = \eta \sum_\mu \sin^2(p_\mu a)$. When the momentum p is close to the boundary of the Brillouin zone, e.g. $p_\mu a \to 0$, we obtain the asymptotic expression we expect:

$$S_q(p) \to \frac{M(2 - M)}{i\gamma_\mu p_\mu a_5 - M(2 - M)m_f}, \tag{E.3}$$

We can see the effect that M has on the quark mass and the normalization factor Z_q of the propagators:

$$m_q = (2 - M)Mm_f \tag{E.4}$$

$$Z_q = (2 - M)M. \tag{E.5}$$

In our free-field calculation discussed in Section 5.3, we need analytic free DWF propagators in coordinate space for various sources. To go to the coordinate space, we need to Fourier transform

these propagators. To save computational cost, the Fourier transformations are performed on the coefficients of the $\mathbf{1}$ and γ_μ matrices[28].

If we write Equation E.1 as:

$$S_q(p) = f(p)(c_\mu(p)\gamma_\mu + c_\mathbf{1}(p)\mathbf{1}), \tag{E.6}$$

where $f(p) = \frac{1}{(We^{\alpha}-1)+m_f^2(1-We^{-\alpha})}$, $c_\mu(p) = -i\overline{p}_\mu$, and $c_\mathbf{1}(p) = -m_f(1 - We^{-\alpha})$. Please note, for $p = (0, 0, 0, 0)$, we must use the asymptotic expression Equation E.3 and write the momentum-space propagator as:

$$S_q(0) = -\frac{1}{m_f}\mathbf{1}. \tag{E.7}$$

Then for position space propagators $S(x)$, we have:

$$S_q(x) = \frac{S_q(0)}{L_xL_yL_zL_t}\mathbf{1} + \sum_{p\neq 0}\frac{f(p)}{L_xL_yL_zL_t}(c_\mu(p)\gamma_\mu + c_\mathbf{1}(p)\mathbf{1}))e^{ipx} \tag{E.8}$$

or

$$S_q(x) = (C_\mu(x)\gamma_\mu + C_\mathbf{1}(x)\mathbf{1}). \tag{E.9}$$

Using Equation E.8, we can easily verify that γ_5-hermiticity is satisfied:

$$S(-x) = \gamma_5 S^\dagger(x)\gamma_5. \tag{E.10}$$

To show this, we should notice that $c_\mu(p)$ are pure imaginary while $f(p)$ and $c_\mathbf{1}$ are pure real and the last two of the gamma matrices' properties in Euclidean space listed below are satisfied:

- $Tr(\gamma_\mu\gamma_\nu) = 4\delta_{\mu,\nu}$
- $\gamma_5\gamma_\mu = -\gamma_\mu\gamma_5$
- $\gamma_\mu^\dagger = \gamma_\mu$

E.1.1 Wall source propagators

For wall source propagators, the spacial momentum $\vec{p} = 0$ and thus we need a non-trivial Fourier transformation only in time. Using the conventions above, each propagator is represented by a 5-element vector $[c_\mu(p), c_{\mathbf{1}}(p)]$ and the wall source propagator $S_q^W(t)$ obtained from the Fourier transformation is given by:

$$S_q^W(t) = \frac{S_q(p=0)}{L_t}\mathbf{1} + \sum_{p_t \neq 0} \frac{f(\vec{0}, p_t)}{L_t}[c_\mu(\vec{0}, p_t)\gamma_\mu + c_{\mathbf{1}}(\vec{0}, p_t)\mathbf{1})]e^{ip_t t} \tag{E.11}$$

or written more compactly as

$$S_q^W(t) = C_\mu(t)\gamma_\mu + C_{\mathbf{1}}(t)\mathbf{1}, \tag{E.12}$$

with $p_t = \frac{2\pi}{L_t} n_t$, where n_t is an integer obeying $-\frac{L_t}{2} < n_t \leqslant +\frac{L_t}{2}$, and L_t is the lattice size in time direction. Because of the spacial translational invariance, the difference between wall-source-point-sink and wall-source-wall-sink propagators is factor of the spacial volume size $V_{3D} = L_x L_y L_z$ and we should be aware of this V_{3D} factor in the contractions.

In our free-field calculation, we adopt the following treatment for the normalization factors:

- Any factor resulting from volume summations are omitted.
- The propagators are not divided by the Z_q factor mentioned in Equation (E.5) for each M value.
- The input mass m_f is modified so that for each M value, the same "physical" fermion mass is used.

Thus, the omitted factors of spatial volume or Z_q mentioned above are restored while doing the contractions. Thus, we will make sure each correlator has the correct normalization, although the propagators are conventionally normalized.

E.1.2 Point-source-point-sink propagators

In principle, we should perform a Fourier transformation as in Equation E.8. The Fourier transformation requires $O(V_{4D})$ operations and further summing up the contracted diagrams is of $O(V_{3D})$, thus the total calculation is estimated to be $O(V_{3D}^2 L_t)$. Here we are assuming an FFT is performed and ignoring a $ln(V)$ factor. This is quite difficult for large lattice like $64^3 \times 128$. However, we can simplify the problem by looking at only a specific contribution to Δm_K from the four-point diagram shown in Figure 5.3c and comparing it with the corresponding three-point diagram shown in Figure 5.3e.

For the four-point diagram shown in Figure 5.3c the spacial dependence of the inner loop could be factored out as follows (if we neglect the spin matrices):

$$C^{\text{4pt}}(t_i, t_f, t_x, t_y) \propto \sum_{\vec{x}} Tr\{S_d^W(t_x - t_i) S_s^{W\dagger}(t_x - t_i) \times S(\vec{x}, t_y - t_x) \times S_d^{W\dagger}(t_y - t_f) S_d^W(t_y - t_f) \times S(-\vec{x}, t_x - t_y)\} \tag{E.13}$$

and we could simplify the loop in the middle as below:

$$C^{\text{4pt}}(t_i, t_f, t_x, t_y) \propto \sum_{\vec{x}} Tr\{...S(\vec{x}, t)...S(-\vec{x}, -t)...\} \tag{E.14}$$

Since the order of summing over $\vec{x}$ and taking the trace is interchangeable, we could sum over $\vec{x}$ first. So if we pick out the tensor element related to the loop:

$$T_{ab}^{\text{4pt,umc}} = \sum_{\vec{x}} (\sum_{p} \frac{S(p)_a e^{ipx}}{L_x L_y L_z L_t}) \otimes (\sum_{p'} \frac{S(p')_b e^{-ip'x}}{L_x L_y L_z L_t}), \tag{E.15}$$

where a, b are each an index specifying a component of the propagator when expressed as a vector of five coefficients. We will omit the tensor indices below but one should assume the indices are implicitly included. Please note that S(0) has a special form but this will not change the equation shown above. If we change the order of the summation and combine the tensor products, we

obtain:

$$
\begin{aligned}
T_{ab}^{\text{4pt,umc}} &= (\sum_{p}\sum_{p'}\frac{S(p)\otimes S(p')e^{i(p_0-p_0')t}}{V^2L_t^2})(\sum_{\vec{x}} e^{i(\vec{p}-\vec{p'})\cdot\vec{x}}) \\
&= \sum_{p}\sum_{p'}\frac{S(\vec{p},p_0)\otimes S(\vec{p'},p_0')e^{i(p_0-p_0')t}}{V^2L_t^2}t(\vec{p}-\vec{p'}) \\
&= \sum_{\vec{p}}\sum_{p_0}\sum_{p_0'}\frac{S(\vec{p},p_0)\otimes S(\vec{p},p_0')e^{i(p_0-p_0')t}}{V^2L_t^2} \\
&= \sum_{\vec{p}}\frac{S(\vec{p},t)\otimes S(\vec{p},-t)}{V^2}.
\end{aligned}
\tag{E.16}
$$

We can then perform the sum over $\vec{p}$ first and obtain:

$$
T_{ab}^{\text{4pt,umc}} = \sum_{p_0}\sum_{p_0'}\frac{(\sum_{\vec{p}} S(\vec{p},p_0)\otimes S(\vec{p},p_0'))e^{i(p_0-p_0')t}}{V^2L_t^2} = \sum_{p_0}\sum_{p_0'}\frac{M(p_0,p_0')e^{i(p_0-p_0')t}}{V^2L_t^2} \tag{E.17}
$$

This is better considering that Matlab can efficiently perform a summation in a parallel manner for the large number of allowed $\vec{p}$.

E.2 Contractions

The contractions in our calculation have traces calculated for products of gamma matrices and this process is independent of the coefficients C_μ and $C_{\mathbf{1}}$. Thus, for a specific contraction, we can perform the trace and obtain a tensor of traces and then combine it with the related components of the propagators.

E.2.1 Two-point contractions

A general two-point contraction with wall sources is given by:

$$
C^{\text{2pt}}(t_i,t_f) = Tr\{\gamma_5 S_1^W(t_f-t_i)\gamma_5 S_2^W(t_i-t_f)\} \tag{E.18}
$$

and we can rewrite in a tensor form as:

$$C^{2\text{pt}}(t_i, t_f) = C^W_{1,i}(t_f - t_i) C^W_{2,j}(t_i - t_f) T^{2pt}_{i,j}, \tag{E.19}$$

where C^W_i are the five components of the propagators and $T^{2pt}_{i,j}$ is generic for all two-point diagrams with pseudo-scalar meson source and sink:

$$T^{2\text{pt}}_{ij} = Tr\{\gamma_5 \Gamma_i \gamma_5 \Gamma_j\},\ \Gamma \in \{\gamma_\mu, \mathbf{1}\}. \tag{E.20}$$

Below are a few comments:

- The components of the reverse propagator can be obtained using γ_5 hermiticity.
- The trace in the code is only for spin, thus one need to multiply the results by number of colors N_c to include the trivial color trace.
- Since there are two quark lines, there is an $Z_q^2 = M^2(2-M)^2$ factor by which the correlation function is needed to be divided to reproduce the usual free-field conventions.

E.2.2 Three-point contractions

The three-point contractions for the three-point diagram shown in Figure 5.3e is given by:

$$C^{3\text{pt}}(t) = Tr[\gamma_5(\gamma_5 S_d^\dagger(t;\Delta)\gamma_5)\gamma_\mu(1-\gamma_5)S_s(t;0)\gamma_5(\gamma_5 S_d^\dagger(t;0)\gamma_5)\gamma^\mu(1-\gamma_5)S_s(t;\Delta)], \tag{E.21}$$

where t is the time difference between the local operator and the source and Δ the time distance between the source and the sink.

In our case we write $C^{3\text{pt}}(t)$ in tensor form:

$$C^{3\text{pt}}(t) = \sum_{\mu=1}^{4} C^W_{d,j}(-(t-\Delta)) C^W_{s,k}(t) C^W_{d,l}(-t) C^W_{s,m}(t-\Delta) T^{3\text{pt,ud}}_{\mu,j,k,l,m}, \tag{E.22}$$

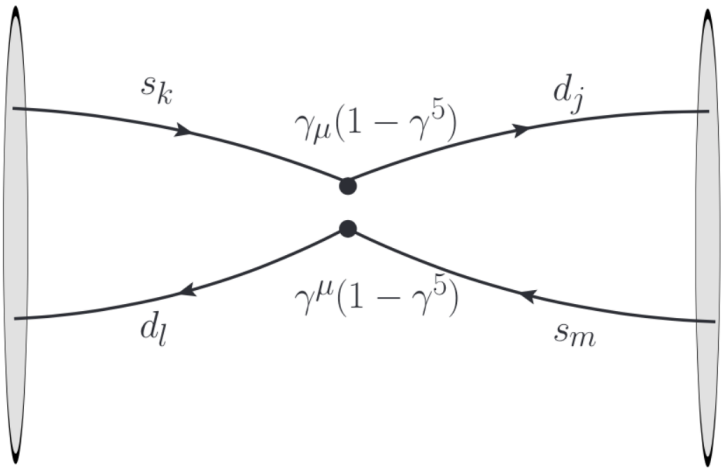

Figure E.1: The three point diagram with tensor index labeled.

where C_i^W are the components of coefficient vector of the propagators, $C_{d,l}^W(-t) = \gamma_5 C_{d,l}^{W\dagger}(t)\gamma_5$ and $C_{d,j}^W(-(t-\Delta)) = \gamma_5 C_{d,j}^{W\dagger}(t-\Delta)\gamma_5$ represent the transposed propagator using γ_5 hermiticity and $T_{\mu,j,k,l,m}^{\text{3pt,ud}}$ includes both the upper half and lower halves of the diagram shown in Figure E.1:

$$T_{\mu,j,k,l,m}^{\text{3pt,ud}} = Tr\{\gamma_5\Gamma_j\gamma_\mu(1-\gamma_5)\Gamma_k\gamma_5\Gamma_l\gamma_\mu(1-\gamma_5)\Gamma_m\},\ \Gamma \in \{\gamma_\mu, \mathbf{1}\}, \tag{E.23}$$

where the repeated index μ is not summed as implemented in my analysis code. **Note:**

- The components of the hermitian conjugate propagator like $C_{d,l}^W(-t)$ could be obtained using γ_5 hermiticity.
- The trace in the code is only for spin. Thus one need to multiply the results by number of colors N_c to include the trivial color trace.
- Since there are four quark lines, there is a $Z_q^4 = M^4(2-M)^4$ factor by which the correlation function needs to be divided.

E.2.3 Four-point contractions

If we omit the gamma matrices, the four-point contraction shown in Figure E.2 is given by:

$$C^{\text{4pt}}(t_i, t_f, t_x, t_y) \propto \sum_{\vec{x}} Tr\{S_d^W(t_x - t_i) S_s^{W\dagger}(t_x - t_i) \times S(\vec{x}, t_y - t_x) \times S_d^W(t_y - t_f) S_s^{W\dagger}(t_y - t_f) \times S(-\vec{x}, t_x - t_y)\}. \tag{E.24}$$

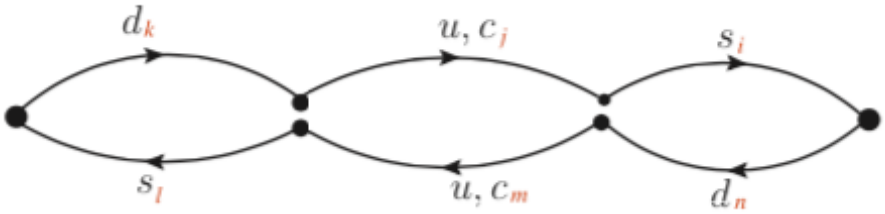

Figure E.2: The four-point diagram with tensor index labeled.

In our case we write it in the tensor form:

$$\begin{aligned} C^{\text{4pt}}(t_i, t_f, t_x, t_y) = \sum_{\mu=1}^{4} \sum_{\nu=1}^{4} & C_{s,i}^W[-(t_y - t_f)] C_{d,k}^W(t_x - t_i) C_{s,l}^W[-(t_x - t_i)] C_{d,n}^W(t_y - t_f) \\ & \times T_{jm}^{4pt,umc}(t_y - t_x) T_{\mu,\nu,i,j,k,l,m,n}^{\text{4pt,ud}}, \end{aligned} \tag{E.25}$$

where C_i^W are the components of the propagators, $C_{s,i}^W[-(t_y - t_f)] = \gamma_5 C_{s,i}^{W\dagger}(t_y - t_f)\gamma_5$ and $C_{s,l}^W[-(t_x - t_i)] = \gamma_5 C_{s,l}^{W\dagger}(t_x - t_i)\gamma_5$ represent the transposed propagators using γ_5 hermiticity and $T_{\mu,\nu,i,j,k,l,m,n}^{\text{4pt,ud}}$ includes both the upper half and lower half of the diagram shown in Figure E.2:

$$T_{\mu,\nu,i,j,k,l,m,n}^{\text{4pt,ud}} = Tr\{\gamma_5 \Gamma_i \gamma_\mu (1-\gamma_5) \Gamma_j \gamma_\nu (1-\gamma_5) \Gamma_k \gamma_5 \Gamma_l \gamma_\nu (1-\gamma_5) \Gamma_m \gamma_\mu (1-\gamma_5) \Gamma_n,\ \Gamma \in \{\gamma_\mu, \mathbf{1}\}, \tag{E.26}$$

where the repeated indices μ, ν are not summed.

Note:

- The components of the reverse propagator could be obtained using γ_5 hermiticity.
- The trace in the code is only for spin, thus one need to multiply the results by number of colors N_c to include the trivial color trace.

- Since there are six quark lines, there is a $Z_q^6 = M^6(2-M)^6$ factor by which the correlation function needs to be divided.

E.3 Time dependence of the free-field correlation functions with around-the-world effects

Because of we calculate the free propagators on a lattice with periodic boundary condition in the time direction, the lattice propagators do not simply equal to those for infinite time extent, but instead are equivalent to a sum of these infinite-time propagators. For the free-field case, due to the absence of confinement from the QCD, the quark propagators connecting the meson interpolating operators can propagate independently on various paths. As a result, the correlation functions we calculated on the lattice after performing contractions may have significantly different time-dependence than for the infinite-time case.

In the large time extent limit, the difference is negligible but in most cases, if we use light quarks and the lattice size in time is limited, the effects may be significant and one needs to examine the around-the-world effects before fitting. In order to extract physical quantities from the correlation functions, we also have to include the around-the-world effects. In this section, we will derive the time dependence for the correlation functions including the around-the-world effects and show how we can extract physical quantities from them.

Basically, a quark propagator $S(t;0) \equiv S(t)$ in a volume of infinite time extent from source at time 0 to sink at time t, is given by:

$$S(t) = S_1 e^{-m_q t}\Theta(t) + S_2 e^{+m_q t}\Theta(-t), \tag{E.27}$$

where S_1 and S_2 are the Wilson matrices corresponding to forward and backward propagation and Θ is the step function.

In the non-relativistic case where $\vec{p} = 0$, $S_1 \propto (\gamma_0 + 1)$ and $S_2 \propto (-\gamma_0 + 1)$. As a result, $S_1 S_1^\dagger \propto (\gamma_0 + 1)$, $S_2 S_2^\dagger \propto (-\gamma_0 + 1)$ and $S_1 S_2^\dagger = 0$. However, the propagator shown in Equation E.27 is not what we have in our lattice calculations. On the lattice we use periodic boundary condition

in time, with a source set at a certain time index on lattice t_{src}, and solve the propagators from the source to each sink point. Different from the single-source result shown above, within the box with periodic boundary conditions in time, for a certain sink, there are infinitely many sources coming from each period. Thus the propagator $S^{\text{lat}}(t)$ calculated on the lattice is given by[21]:

$$S^{\text{lat}}(t) = \sum_{i=0}^{\infty} S(t + iT) + \sum_{j=0}^{\infty} S(-(T - t) - jT), \tag{E.28}$$

where T is the period in the time direction of our lattice. The terms in the sum with index i are propagators with sources on the left (earlier time) side and those with index j are propagators with sources on the right (later time) side. If we plug Equation E.27 into the equation above, we obtain:

$$S^{\text{lat}}(t) = S_1 e^{-m_q t} \sum_{i=0}^{\infty} e^{-i m_q T} + S_2 e^{-m_q (T-t)} \sum_{j=0}^{\infty} e^{-j m_q T}. \tag{E.29}$$

And using $\sum_{i=0}^{\infty} x^i = \frac{1}{1-x}$, we simplify it to:

$$S^{\text{lat}}(t) = \frac{1}{1 - e^{-m_q T}} (S_1 e^{-m_q t} + S_2 e^{-m_q (T-t)}). \tag{E.30}$$

E.3.1 Pseudo-scalar meson: two-point correlation functions

For our lattice calculation, the meson two-point correlators are given by:

$$C(t) = Tr[S_q(t;0)\gamma_5 S_{q'}(0;t)\gamma_5], \tag{E.31}$$

where the γ_5 comes from the pseudo-scalar meson interpolating operator. Using γ_5 Hermiticity $S(y;x) = \gamma_5 S^{\dagger}(x;y)\gamma_5$ and $\gamma_5^2 = 1$, we have:

$$C(t) = Tr[S_q(t;0) S^{\dagger}_{q'}(t;0)] \equiv Tr[S_q(t) S^{\dagger}_{q'}(t)] \tag{E.32}$$

If we use the expression for the free lattice propagators shown in Equation E.30 in, we obtain the time dependence for the conventional two-point correlation function shown in Equation E.31:

$$C(t) = N^2(\frac{1}{1-e^{-m_q T}})(\frac{1}{1-e^{-m_{q'} T}})[e^{-(m_q+m_{q'})t} + e^{-(m_q+m_{q'})(T-t)}], \tag{E.33}$$

where N is defined as $N^2 \equiv Tr(S_1 S_1^\dagger) = Tr(S_2 S_2^\dagger)$ and we have used $S_1 S_2^\dagger = 0$ which is valid for the zero momentum case.

Thus, we can perform the analysis discussed in Section 4.1.1 to extract the normalization factors and the effective masses and we will expect the effective mass obtained $m_{\text{eff}} = m_q + m_{q'}$. Thus, for our free-field case the structure of our "meson" propagator look remarkably like what is found in a confining theory!

Using the input masses listed in Tab. E.1, we fit the curve shown in Figure E.3 to Equation E.33, we can find that $m_{ll} = 2m_l$ and $m_{ls} = m_l + m_s$ as listed in Tab. E.1.

m_l	m_s	m_{ll}	m_{ls}
0.02	0.03	0.039997	0.049994

Table E.1: Masses obtained from fitting of two-point correlation functions using input masses listed in the first and second columns. ll denotes that two light quarks propagators are used in the two-point contractions. and ls denotes one light and one strange quark propagators are used in the two-point contractions.

E.3.2 Pseudo-scalar meson: three-point correlation functions

Following the discussion in Section 4.1.2, for the free-field case, when the around-the-world effects are negligible, and we expect the three-point correlation function, using the B_K diagram as an example, can be written as:

$$C_{3\text{pt}}(\Delta, t) = N_K^2 \langle \overline{K^0} | O_{LL} | K^0 \rangle e^{-m_K(\Delta - t)} e^{-m_K t}, \tag{E.34}$$

where t denotes the time difference between the O_{LL} operator and the kaon source and Δ is the source-sink separation.

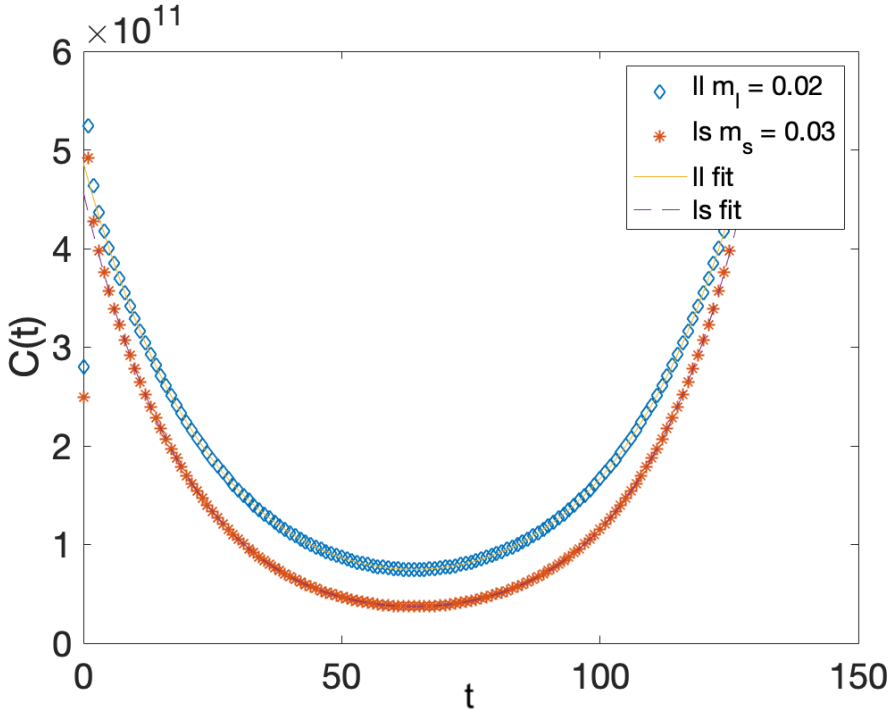

Figure E.3: Free two-point correlation functions and fitting curves.

Here, we will derive the expression for three-point contractions with the around-the-world effects taken into account.

To calculate the three-point B_K matrix element, we have to calculated the two contractions shown in Figure E.4b which we label it to be "1" and Figure E.4c which we label it to be "2":

$$C_1(\Delta, t) = Tr[\gamma^\mu(1-\gamma_5)S_u(t;0)S_s^\dagger(t;0)\gamma_5] \times Tr[\gamma_\mu(1-\gamma_5)S_u(t;\Delta)S_s^\dagger(t;\Delta)\gamma_5], \tag{E.35}$$

$$C_2(\Delta, t) = Tr[\gamma^\mu(1-\gamma_5)S_u(t;0)S_s^\dagger(t;0)\gamma_5) \times \gamma_\mu(1-\gamma_5)S_u(t;\Delta)S_s^\dagger(t;\Delta)\gamma_5], \tag{E.36}$$

where the γ_5 comes from the pseudo-scalar interpolating operator and we have used γ_5 Hermiticity $S(y;x) = \gamma_5 S^\dagger(x;y)\gamma_5$ and $\gamma_5^2 = 1$. $S_q(t;\Delta)$ denotes a propagator with the source at time Δ and the sink at time t and quark flavor q. Δ is the source-sink separation and is larger than t.

The quark propagator $S_q(t;\Delta)$ calculated on the lattice with the periodic boundary conditions in the time direction can be expressed in terms of propagators $S(t) \equiv S(t;0)$ in the infinite volume

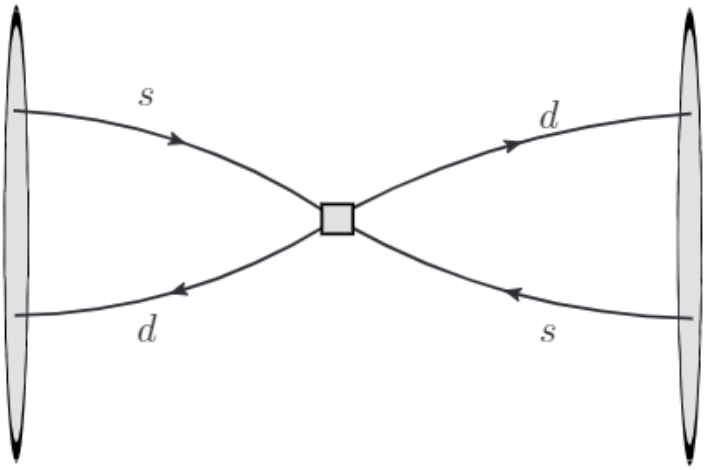

(a)

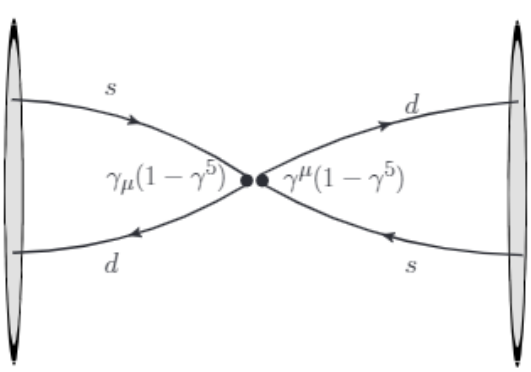

(b)

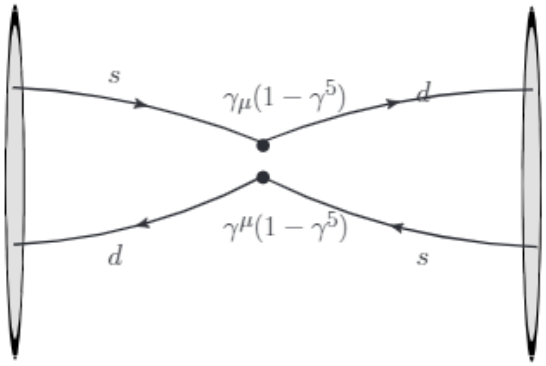

(c)

Figure E.4: Three-point B_K diagram with the square block representing the operator O_{LL}(a). Two possible contractions are shown in (b) and (c).

as:

$$S^{\text{lat}}(t;\Delta) = \sum_{i=0}^{\infty} S(T-(\Delta-t)+iT) + \sum_{j=0}^{\infty} S(-(\Delta-t)-jT) \tag{E.37}$$

$$S^{\text{lat}}(t;\Delta) = \frac{1}{1-e^{-m_q T}}(S_1 e^{-m_q(T-(\Delta-t))} + S_2 e^{-m_q(\Delta-t)}). \tag{E.38}$$

Thus, in the zero momentum case where $S_i S_j^\dagger = N^2\delta_{ij}$ and $i, j = 1, 2$, we can calculate some useful quantities like:

$$Tr[\gamma^\mu(1-\gamma_5)S_1 S_1^\dagger \gamma_5] = -NTr[\gamma^\mu\gamma_5\gamma_0\gamma_5] = -Tr[\gamma^\mu(1-\gamma_5)S_2 S_2^\dagger\gamma_5] \equiv \alpha^\mu, \tag{E.39}$$

$$Tr[\gamma^\mu(1-\gamma_5)S_1 S_2^\dagger\gamma_5] = 0. \tag{E.40}$$

Then if we substitute the propagators in Equation E.35 with the expressions in E.30 and Equation E.38, using the results calculated in Equation E.39 and Equation E.40 , we obtain:

$$\begin{aligned} C_1(\Delta,t) &= (\alpha^\mu e^{-m_K t} - \alpha^\mu e^{-m_K(T-t)}) \times (\alpha_\mu e^{-m_K(T-(\Delta-t))} - \alpha_\mu e^{-m_K(\Delta-t)}) \\ &= -\alpha^2(e^{-m_K t} - e^{-m_K(T-t)}) \times (e^{-m_K(\Delta-t)} - e^{-m_K(T-(\Delta-t))}) \\ &= -\alpha^2(e^{-m_K\Delta} - e^{-m_K(T-t)}e^{-m_K(\Delta-t)} - e^{-m_K(T-(\Delta-t))}e^{-m_K t} + e^{-m_K(2T-\Delta)}) \\ &= -\alpha^2[e^{-m_K\Delta} - e^{-m_K(T-\Delta)}(e^{-2m_K(\Delta-t)} - e^{-2m_K t}) + e^{-m_K(2T-\Delta)}], \end{aligned} \tag{E.41}$$

where m_K denotes the sum $m_l + m_s$. Thus we expect $C_1(\Delta, t)$ to be a t-dependent function of the form:

$$C_1(\Delta,t) = A_1[-2e^{-m_K T}\cosh(m_K(\Delta-2t)) + A_1'], \tag{E.42}$$

where A_1 and $A_1' = e^{-m_K\Delta} + e^{-m_K(2T-\Delta)}$ are constants and for $t = 0$, we have $C_1(\Delta, t = 0) = 0$.

Similarly, for $C_2(\Delta, t)$, we first calculate the trace part:

$$Tr[\gamma^\mu(1-\gamma_5)S_i S_i^\dagger\gamma_5\gamma_\mu(1-\gamma_5)S_j S_j^\dagger\gamma_5] \propto Tr[\gamma^\mu(1-\gamma_5)(\pm\gamma_0+1)\gamma_\mu(1-\gamma_5)(\pm\gamma_0+1)\gamma_5]\times f^{\pm\pm}(T,\Delta,t), \tag{E.43}$$

where $f^{\pm\pm}(T, \Delta, t)$ is the time factor depending on the 4 ± combinations:

$$f^{\pm\pm}(T, \Delta, t) = \begin{cases} e^{-m_K(T-(\Delta-t))}e^{-m_K t}, ++ \\ e^{-m_K \Delta}, +- \\ e^{-m_K(2T-\Delta)}, -+ \\ e^{-m_K(T-t)}e^{-m_K(\Delta-t)}, -- \end{cases} \tag{E.44}$$

Using the following relations:

$$Tr[\gamma^\mu(1-\gamma_5)(1)\gamma_\mu(1-\gamma_5)(1)\gamma_5] = 0, \tag{E.45}$$

$$Tr[\gamma^\mu(1-\gamma_5)(\pm\gamma_0)\gamma_\mu(1-\gamma_5)(1)\gamma_5] = Tr[\gamma^\mu(1-\gamma_5)(1)\gamma_\mu(1-\gamma_5)(\pm\gamma_0)\gamma_5] = 0, \tag{E.46}$$

$$Tr[\gamma^\mu(1-\gamma_5)(\pm\gamma_0)\gamma_\mu(1-\gamma_5)(\pm\gamma_0)\gamma_5] = \pm\pm 2Tr[\gamma^\mu\gamma_0\gamma_\mu\gamma_0] \equiv \pm\pm\alpha'^2, \tag{E.47}$$

we obtain:

$$C_2(t) = -\alpha'^2[e^{-m_K\Delta} - e^{-m_K(T-\Delta)}(e^{-2m_K(\Delta-t)} - e^{-2m_K t}) + e^{-m_K(2T-\Delta)}] \tag{E.48}$$

Thus we expect $C_2(\Delta, t)$ to be a t-dependent function of the form:

$$C_2(\Delta, t) = A_2[-2e^{-m_K T}\cosh(m_K(\Delta - 2t)) + A_2'], \tag{E.49}$$

where A_2 and $A_2' = e^{-m_K\Delta} + e^{-m_K(2T-\Delta)}$ are constants and for $t = 0$, we have $C_2(\Delta, t = 0) = 0$.

Lastly, by adding Equation E.42 and Equation E.49 together, we obtain an expression prediction of the three-point correlator related to B_K:

$$\mathcal{F}_{B_K}(t) = N_K^2(\frac{1}{1-e^{-m_l T}})^2(\frac{1}{1-e^{-m_s T}})^2\langle\overline{K^0}|O_{LL}|K^0\rangle[-2e^{-m_K T}\cosh(m_K(\Delta-2t)) + A_2'], \tag{E.50}$$

where $A_2' = A_1' = e^{-m_K\Delta} + e^{-m_K(2T-\Delta)}$ and N_K denotes the normalization factor N defined in

Equation E.33 for the specific pair of light and strange quarks. We can also find in the limit where T is large, Equation E.34 is reproduced while for $t = 0$, we have $\mathcal{F}(t = 0) = 0$.

In Figure E.5, we show that the three-point B_K correlation functions we have obtained and the fitting curve of the form shown in Equation E.50 are very consistent.

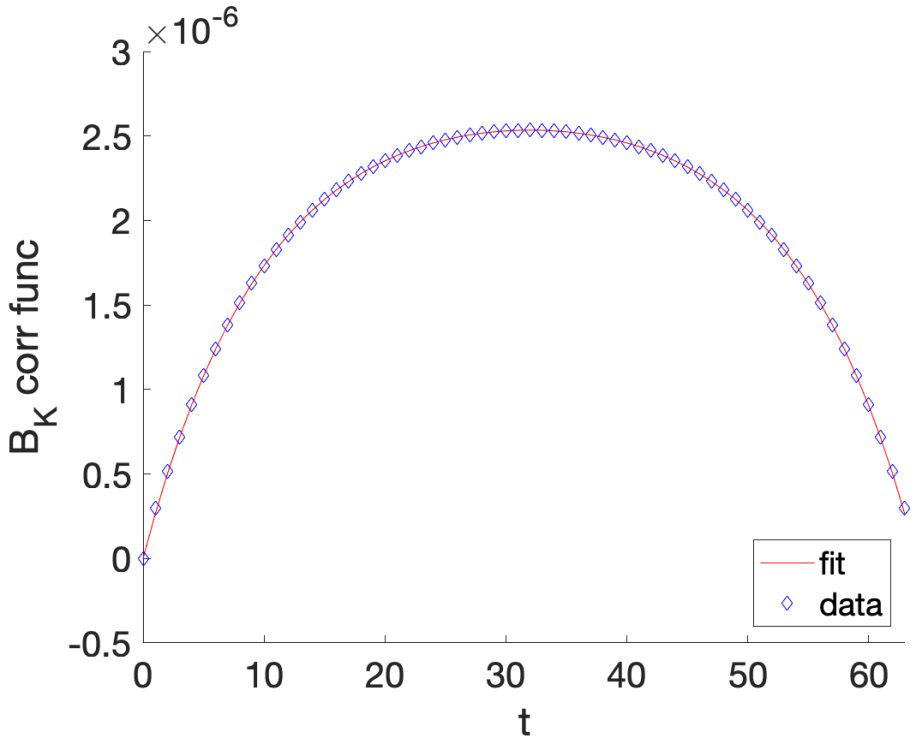

Figure E.5: Free three-point B_K correlation function $\mathcal{F}_{B_K}(t)$ as defined in Equation E.50 and fitting curves, calculated using the input masses listed in Tab. E.1.

We can therefore use the formulas derived above to evaluate the around-the-world effects in our free-field calculations and extract normalization factors of the interpolating operators and three-point matrix elements from two-point and three-point correlation functions in our free-field calculation even when the around-the-world effects are not negligible.